ELECTRONIC FABRY-PEROT INTERFEROMETRY OF QUANTUM HALL EDGE STATES

A Dissertation

Submitted to the Faculty

of

Purdue University

by

James R. Nakamura

In Partial Fulfillment of the

Requirements for the Degree

of

Doctor of Philosophy

August 2020

Purdue University

West Lafayette, Indiana

THE PURDUE UNIVERSITY GRADUATE SCHOOL
STATEMENT OF DISSERTATION APPROVAL

Dr. Michael Manfra, Chair

Department of Physics and Astronomy

Dr. Gabor Csathy

Department of Physics and Astronomy

Dr. Matthew Jones

Department of Physics and Astronomy

Dr. Rudro Biswas

Department of Physics and Astronomy

Approved by:

Dr. John P. Finley

Department of Physics and Astronomy

I dedicate this work to my family and our loving dog Roxie.

ACKNOWLEDGMENTS

The person who I owe the most to in my career as a graduate student is my advisor, Professor Michael Manfra. I first walked in the door never having heard of the quantum Hall effect, a lock-in amplifier, or a dilution refrigerator, and now due to his extensive mentoring and support I'm writing a thesis about measuring quantum Hall physics with lock-in amplifiers in a dilution refrigerator. I've been very fortunate to work for someone with expertise and resources in so many areas - MBE growth, device fabrication, and cryogenic measurements - and Professor Manfra's support in each of these areas has been crucial to all of my PhD work.

Additionally, I am grateful to the other members of my committee - Professors Gabor Csathy, Rudro Biswas, and Matthew Jones - for their time and support. I would never be able to graduate without them! Also, I'm writing this during the Covid-19 outbreak and lockdown, so I especially appreciate their flexibility in working with me during these challenging times.

I want to give special thanks to the MBE growth team who provided the ultra high quality GaAs/AlGaAs wafers I've used for my experiments, and this team includes Geoff Gardner, Saeed Fallahi (recently graduated), Shuang Liang, and Alex Webster. Direct access to amazing quality material has been critical to all the experimental work I've done, particularly the screening well interferometer studies. Saeed deserves additional credit for his mentoring in device fabrication and measurement; I learned a significant amount of basic experimental technique from Saeed.

In addition to the MBE growth team, there are several colleagues I've worked with who have been important to my development as a researcher. In the earlier years of my PhD I worked extensively with Qi Qian on multiple papers in quantum Hall physics, and I learned a lot in my discussions and work with her. Although I did not work with him as much directly, I also benefited significantly from Anthony

Hatke, particularly in learning how to navigate the world of physics research. For my work in the cleanroom, Ray Kallaher has been both an excellent intellectual resource as well as provided extremely valuable work in terms of maintaining critical pieces of equipment that I've used. Also, although I didn't overlap with him much directly, the spirit of the former graduate student John Watson (communicating to me through his excellent thesis, which I refer to constantly) has provided invaluable guidance. Furthermore, I want to thank all the other members of the Manfra group who I've worked with over the years.

Outside of the Manfra group, I also worked signficantly with Harshad Sahasrabudhe. Harshad's numerical simulations were very helpful in understanding interferometer behavior and resulted in nice publications, and I thank Harshad for his work.

Of course, there's a tremendous amount of support I've received from the Purdue University staff. Sandy Formica has worked tirelessly to keep me (and all the other graduate students!) on track, and I greatly appreciate her help over the years. None of the measurements I've done would have been possible without liquid helium, so I'm indebted to Keith Schmitter for keeping us up and running with a reliable supply. Other staff in the Physics building have been critical to my ability to conduct research, and I appreciate all their hard work. Likewise, the engineers and other staff in the Birck nanotechnology center have done fantastic work maintaining equipment and enabling high-quality research, and I want to thank all of them.

Finally, the most important support I've received in life has been from my parents. I would never have gotten through high school, through college, or through my PhD work without their love and support.

TABLE OF CONTENTS

Page

Page

LIST OF TABLES

LIST OF FIGURES

Figure Page

Figure Page

Figure Page

Figure Page

Figure Page

Figure Page

Figure Page

Figure Page

Figure Page

SYMBOLS

ν	electron filling factor
n	electron density
B	Magnetic field
e	electron charge
e^*	quasiparticle effective charge
v_{edge}	edge state velocity
θ	phase
Φ_0	magnetic flux quantum

ABBREVIATIONS

GaAs	Gallium Arsenide
AlGaAs	Aluminum Gallium Arsenide
AlAs	Aluminum Arsenide
2DES	two-dimensional electron system
2DEG	two-dimensional electron gas
QW	quantum well
SW	screening well
AB	Aharonov-Bohm
CD	Coulomb-dominated

ABSTRACT

Nakamura, James R. Ph.D., Purdue University, August 2020. Electronic Fabry-Perot Interferometry of Quantum Hall Edge States. Major Professor: Michael J. Manfra.

Two-dimensional electron systems in GaAs/AlGaAs heterostructures have provided a platform for investigating numerous phenomena in condensed matter physics. The quantum Hall effect is a particularly remarkable phenomenon due to its topological properties, including chiral edge states with quantized conductance. This report describes progress made in interference measurements of these edge states in electronic Fabry-Perot interferometers. Previous interference experiments in the quantum Hall regime have been stymied by Coulomb charging effects and poor quantum coherence. These Coulomb charging effects have been dramatically suppressed by the implementation of a novel GaAs/AlGaAs heterostructure which utilizes auxiliary screening wells in addition to the primary GaAs quantum well. Using this heterostructure, Aharonov-Bohm interference is measured in very small devices which have greatly improved coherence. Robust Aharonov-Bohm interference is reported at fractional quantum Hall states $\nu = 1/3$ and $\nu = 2/3$. Discrete jumps in phase at $\nu = 1/3$ consistent with anyonic braiding statistics are observed. The report concludes with proposed future experiments, including extending these results to possible non-Abelian quantum Hall states.

1. INTRODUCTION

1.1 Two-dimensional Electron Systems

To a layman, a "Two-Dimensional Electron System" (2DES) may sound like a hopelessly exotic and esoteric thing to study which could not possibly have any relevance for everyday life. Nothing could be further from the truth given the huge impact that semiconductor technology and in particular CMOS have had on technology and our lives. In my area of research we study two-dimensional electron systems in semiconductors (which are not too different from some of the transistors you find in your computer or phone) and subject them to exotic conditions: very low temperature and very high magnetic field. Under these conditions the 2DES may form a variety of fascinating phases determined by the electrons' quantum mechanical behavior and by the Coulomb interaction between the electrons.

1.2 Gallium Arsenide Heterostructures

The material system I have been studying is the GaAs/AlGaAs heterostructure [1] grown by Molecular Beam Epitaxy (MBE). The beauty of this III-V semiconductor system is that GaAs is nearly exactly lattice matched to AlAs (as well as to intermediate AlGaAs alloys), which makes it possible to grow complicated structures layer by layer without producing strain induced defects. This enables growth of extremely high quality GaAs 2DESs [1–3]. Such high quality, low disorder samples are necessary for observation of fragile correlated electron quantum states, such as the fractional quantum Hall states, which are easily destroyed by disorder.

The layer stack for a simple GaAs/AlGaAs heterostructure is shown in Fig. 1.1a, and a simulation of the band structure and electron density for this heterostructure

produced using the nextnano software package [4] is shown in Fig. 1.1b. The energy of the conduction band is higher in the AlGaAs than in the GaAs, so there is effectively a potential minimum in the GaAs at the interface which confines electrons; the Gamma-band energy plotted in red in Fig. 1.1b can be though of as this confining potential. This confining potential is in the z-direction (along which the structure is grown); in the x and y directions which form the plane of the 2DES, the electrons are unconfined except by the edges of the sample, or in some devices by the potentials applied by metal gates. It is important to note that undoped GaAs is an insulator, with the Fermi level pinned in the middle of the band gap at the surface. Therefore, in order to supply electrons to the 2DES, the structure is doped with silicon, which acts as a donor of electrons.

An important considerations is the fact that, once ionized, the Si donors form a random electrostatic potential that causes scattering of electrons in the 2DES, and it is necessary to minimize this source of disorder in order to observe the fragile fractional quantum Hall states. Therefore, the heterostructures are designed using the technique of modulation doping [5], in which the Si donors are separated from the 2DES by an undoped AlGaAs spacer. Because the conduction band minimum of GaAs is well below that of $AlGa_{0.36}As_{0.64}$, electrons will transfer to the GaAs region rather than remaining in the doped region. In general a larger setback of the 2DES from the donors will result in lower disorder and a cleaner 2DES, but lower electron density.

MBE growth of high-quality material is both a science and an art form. High-mobility GaAs capable of supporting fragile quantum states requires ultra-high vacuum ($\sim 10^{-12}$ mbar), extremely high purity source material, and atomically precise control of the growth process [1–3,6]. Over the last several decades, improvements in MBE growth technology have resulted in dramatically higher electron mobilities and enabled the study of numerous fragile electronic phases of matter [2,5,7–10]. I cannot take credit for any part of the growth process myself, so I consider myself extremely fortunate to be part of a group with the best MBE growth capabilities in the world.

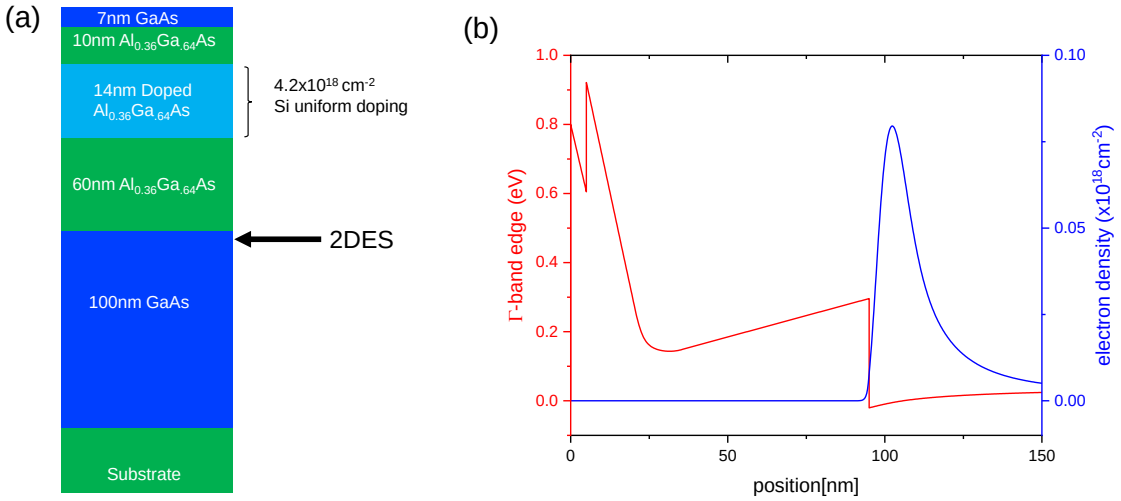

Fig. 1.1. **GaAs/AlGaAs heterostructures.** (a) Layer stack showing the sequence of GaAs and AlGaAs along the MBE growth direction, starting from the GaAs substrate. The structure depicted is a simple single interface design, in which charge transfers from the doped AlGaAs region to the GaAs, resulting in a 2DES in the GaAs at the interface. (b) Numerical simulation of the band structure showing the energy of the conduction band minimum and the electron density along the growth direction. The gamma-band energy (red) acts as the effective confining potential, with a potential minimum at the GaAs/AlGaAs interface which confines electrons. The structure is designed so that only the first subband is occupied, making the structure effectively two-dimensional despite the finite extent of the wave function (blue). The simulation was performed using the self-consistent Schrodinger-Poisson method using nextnano [4]

1.3 Quantum Hall Effect

A clean 2DES (such as the one depicted in Fig. 1.1) cooled to low temperatures and subjected to a perpendicular magnetic field B exhibits a remarkable phenomenon: the quantum Hall effect. The quantum Hall effect was discovered by von Klitzing in 1980 [11, 12], and has been the subject of intense study in the decades since. The quantum Hall effect is characterized by zero longitudinal resistance R_{xx} (measured

parallel to the flow of current) and *quantized* Hall resistance R_{xy} (measured perpendicular to the flow of current). The measurement setup for observing the quantum Hall effect is illustrated in Fig. 1.2.

Understanding the quantum Hall effect requires solving the problem of an electron in a uniform magnetic field. The Hamiltonian (neglecting spin for now) is written in Eqn. 1.1:

$$H = \frac{1}{2m^*}(\vec{p} + e\vec{A})^2 \tag{1.1}$$

Where m^* is the electron's effective mass, $\vec{p}$ is the momentum, and $\vec{A}$ is the magnetic vector potential. Common choices of the gauge potential to use are the Landau gauge and the symmetric gauge, but regardless of the choice of gauge the energy spectrum is the same: the eigenstates have energy $E_N = (N + 1/2)\hbar\omega_c$, where $N = 0, 1, 2...$ is the Landau level index and $\omega_c \equiv \frac{eB}{m^*}$ is the cyclotron frequency.

Landau quantization results in a flat band structure with an energy gap of $\hbar\omega_c$ between Landau levels. When the Fermi energy lies between Landau levels (in other words, when an integer number of Landau levels is fully filled), there will be zero density of states (DOS) available for conduction in the bulk, making the bulk an insulator. Each Landau level has a fixed degeneracy per unit area equal to $\frac{eB}{h}$. A parameter called the filling factor, ν, is used to keep track of the number of filled Landau levels, and is defined as $\nu \equiv \frac{nh}{eB}$, where n is the electron sheet density in the 2DES. At the edges of the sample, on the other hand, the confining potential causes the Landau level energies to bend upward, and the Fermi energy will cross each occupied Landau level. This results in edge states that carry current with chirality set by the direction of the magnetic field.

In real samples the Landau level DOS will be broadened by finite disorder, so the bulk will never truly have zero DOS. However, charge tends to be localized in the hills and valleys of the disorder potential, which leads to an insulating bulk despite finite DOS over a finite range of filling factor [13]. At low temperatures and high magnetic fields the conduction of localized states in the bulk drops exponentially, leading to

the observed quantized Hall conductance (due to the edge states) and vanishing bulk conductance. This is usually probed by measuring a four-terminal resistance (rather than conductance) to avoid the effect of contact and electrical lead resistance. In a typical quantum Hall experiment a fixed AC current I is driven through the sample and the longitudinal voltage V_{xx} and perpendicular voltage V_{xy} are measured with lock-in amplifiers. The longitudinal resistance $R_{xx} \equiv V_{xx}/I$ and the Hall resistance $R_{xy} \equiv V_{xy}/I$ are then calculated. This typical measurement circuit is shown in Fig. 1.2a.

Since electron density is usually fixed (unless deliberately changed via a gate), there will be only one point in magnetic field where the filling factor $\nu \equiv \frac{nh}{eB}$ is an integer, and an exact amount of Landau levels is fully filled and the rest fully empty. This makes it surprising that the quantum Hall plateaus persist over a finite (and fairly wide) range of magnetic field. This phenomenon is actually explained by the inevitable presence of disorder: when a Landau level is only slightly filled, the few electrons in it (or few holes, if it is instead only slightly emptied) become localized in the hills and valleys of the disorder potential [13, 14]. Because these excess electrons are localized and thus don't contribute to conduction, R_{xy} remains quantized and R_{xx} remains zero because the system behaves as if an exact integer number of Landau levels were fully filled.

The quantum Hall effect is an amazingly robust phenomenon - the measured longitudinal and Hall resistances are independent of sample size or shape and even against moderate amounts of disorder. One testament to the robustness of the quantum Hall effect is the crude samples we frequently use to probe it - to measure bulk quantum Hall we typically cleave so-called Van der Pauw squares measured by eye to be roughly 4mm, and for contacts we make scratches at the edges and attach wires with blobs of indium. Despite the messy and inexact nature of these samples, the Hall conductance is exactly quantized to $R_{xy} = \frac{1}{i}\frac{h}{e^2}$ [12], with i being an integer which corresponds to the number of fully filled Landau levels. For some applications we fabricate Hall bars

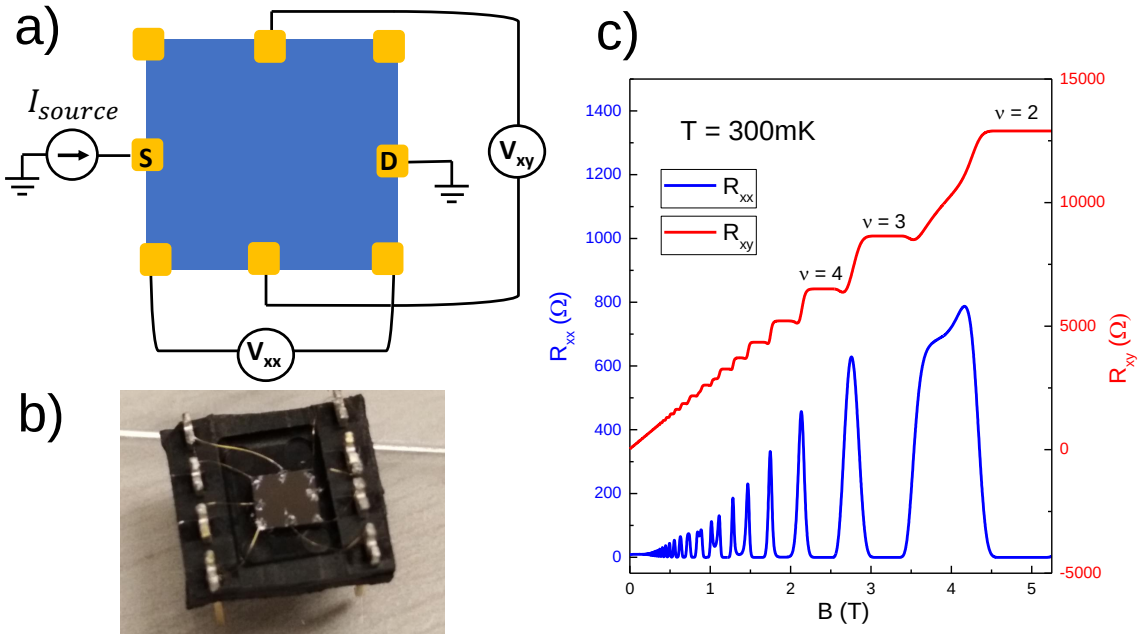

Fig. 1.2. **Quantum hall effect.** (a) Typical measurement circuit for the quantum Hall effect in a bulk semiconductor sample. A current is sourced from source contact S to drain contact D. The longitudinal voltage V_{xx} and Hall voltage V_{xy} are measured and used to calculate R_{xx} and R_{xy}. (b) A typical GaAs sample used for bulk quantum Hall measurements. Despite the haphazard shape and arrangement of indium contacts, such samples typically exhibit exact quantization of R_{xy} as well as zeros in R_{xx} at numerous integer and some fractional filling factors. (c) Typical integer quantum Hall data, showing pronounced plateaus in R_{xy} with $R_{xy} = \frac{1}{i}\frac{h}{e^2}$ and corresponding zeros in R_{xx} for integer i fully filled Landau levels.

with tightly controlled dimensions, but in the quantum Hall regime these give exactly the same result as the haphazard Van der Pauw squares.

1.4 Topology

The observation of quantized conductance under a variety of sample parameters strongly suggests that the quantum Hall effect has a connection to topology, the

branch of mathematics which studies properties of systems which do not change when system parameters are changed continuously. Laughlin gave an explanation for the quantization through arguments of gauge invariance [15]. A more complete explanation was provided by Thouless and coworkeres, who elegantly demonstrated the application of topology to the quantum Hall effect, and found that the Hall conductance is a topological invariant [16, 17]. This explains the robust quantization of the Hall conductance for different systems with different geometries and levels of disorder. While disorder and other sample details modify the energies and wave functions of electron states, as long as the disorder is not great enough to close the energy gap Thouless's arguments hold and the Hall conductance remains quantized.

1.5 Fractional Quantum Hall Effect

Quantum Hall states occurring at integer filling factors are readily understood in terms of the non-interacting picture described previously. However, in 1982 a surprising phenomenon was observed: a plateau in R_{xy} and minimum in R_{xx} at a *fractional* filling factor, $\nu = 1/3$, with the plateau in R_{xy} also corresponding to fractionally quantized conductance, $R_{xy} = 3\frac{h}{e^2}$ [18–20]. Explanation of this *fractional* quantum Hall state required a theory which takes into account the Coulomb interaction between electrons. A first theory was provided by Laughlin [21], who provided a wave function for a gapped state at filling factor $\nu = 1/3$ (which generalizes to other fractional fillings of the form $\nu = \frac{1}{2p+1}$, with p an integer). However, as the quality of GaAs heterostructures improved over time, numerous other fractional quantum Hall states were observed [22–26] which did not fit into the Laughlin sequence.

A more general theory of the fractional quantum Hall effect was provided by Jain's composite fermion theory [27–29]. Composite fermion theory starts with a core premise: an even integer number of flux quanta (taken from the overall applied magnetic field) attach to each electron, thus forming the composite fermion quasiparticles; a cartoon of this process is shown in Fig 1.3. Then, the leftover magnetic flux

causes the composite fermions to exhibit the *integer* quantum Hall effect at effective integer filling factors ν^*. The real filling factor for these composite fermion quantum Hall states is $\nu = \frac{\nu^*}{2p\nu^* \pm 1}$, with p and ν^* both integers. Remarkably, the fractional quantum Hall states observed in the lowest ($N = 0$) Landau level exactly follow this sequence, making Jain's theory highly successful at explaining experiments.

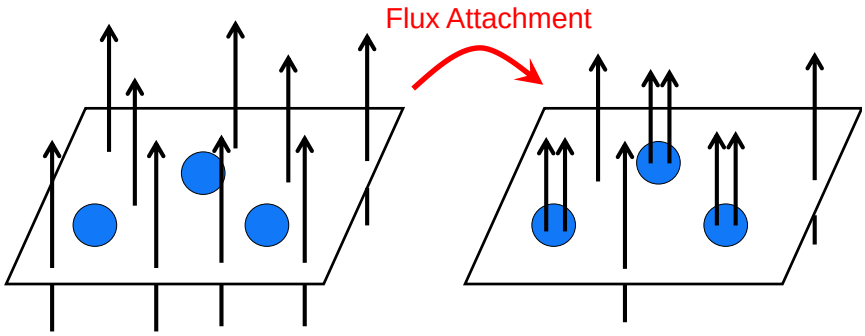

Fig. 1.3. **Composite fermion states.** Cartoon showing the flux attachment process by which electrons are transformed into composite fermions. In the cartoon there are three flux quanta per electron, two of which attach and form the composite fermion; this situation corresponds to the $\nu = 1/3$ fractional quantum Hall state.

The composite fermion wave function is shown in Eqn. 1.2. The factor $\prod_{j<k}(z_j - z_k)^{2p}$ achieves flux attachment (making each electron see $2p$ flux quantua on each other electron) and transforming them into composite fermions; here $z_i \equiv x_i + iy_i$ is the complex coordinate of electron i in the 2DES. The term Φ_{ν^*} places the composite fermions in Landau levels filled up to ν^*, and $\mathcal{P}_{LLL}$ projects the resulting wave function into the lowest Landau level. The case of $\nu^* = 1$ yields the Laughlin wavefunction (for which the lowest Landau level projection is not needed).

It is the flux attachment term which makes the composite fermion wave function effective at minimizing the energy of the system. The $\prod_{j<k}(z_j - z_k)^{2p}$ term keeps the electrons far apart from one another by making the amplitude of the wave function small when they draw too close, thus reducing the electrostatic energy of the system.

$$\Psi_{\nu=\frac{\nu^*}{2p\nu^*+1}} = \mathcal{P}_{LLL}\Phi_{\nu^*}\prod_{j<k}(z_j - z_k)^{2p} \tag{1.2}$$

It is important to emphasize that neither the Laughlin nor the composite fermion wave functions are exact solutions to the Schrodinger equation. Furthermore, flux attachment does not literally occur; the real magnetic field is uniform. However, the theory qualitatively matches experimental observation of gapped quantum Hall states at exactly the predicted filling factors, and exact diagonalization studies have found good overlap between the composite fermion wave functions and the exact ground states [29]. Thus, despite not being an exact analytical solution, composite fermion theory is a very good approximation for reality and has proved very useful for understanding behavior in the fractional quantum Hall regime. That said, it is worth mentioning that a few even-denominator fractional quantum Hall states, such as the famous $\nu = 5/2$ state, have been observed, and drawn considerable interest [25,30,31]. The $\nu = 5/2$ state does not easily fit into the composite fermion picture, but may be a paired state of composite fermions [29, 32, 33].

1.6 Fractional Quasiparticles

Despite their close relationship to the integer quantum Hall effect of non-interacting particles, fractional quantum Hall states are predicted to have interesting properties which differ from their integer counterparts. Fractional quantum Hall states are predicted to host quasiparticle excitations which carry a rational fraction of the electron's charge [21, 29, 34]. For a state $\nu = \frac{\nu^*}{2p\nu^*\pm1}$ fitting into the composite fermion picture the predicted quasiparticle charge is $e^* = \frac{e}{2p\nu^*\pm1}$ [29, 35, 36].

Even more remarkably, these quasiparticles are predicted to abey *anyonic braiding statistics*. When the positions of two fermions are exchanged, the system acquires a phase of π, while when two bosons are exchanged the phase is 2π; however, these quasiparticles are neither fermions nor bosons, but *anyons* for which a phase equal to a fraction of π is obtained when positions are exchanged [34, 37]. A braiding oper-

ation, in which one quasiparticle encircles another, is equivalent to two quasiparticle exchanges. For a Laughlin state the anyonic phase accumulated in a braiding operation is predicted to be $\theta_{anyon} = 2\pi \times \frac{1}{2p+1}$ for a state $\nu = \frac{1}{2p+1}$ [34]. For composite fermion states with $\nu = \frac{\nu^*}{2p\nu^*+1}$, this generalizes to $\theta_{anyon} = 2\pi\frac{p}{2\nu^*p+1}$ [29, 36]. In the case of $\nu^* = 1$, this result is consistent with the value for the value derived for a Laughlin state modulo 2π. Quasiparticle braiding can be seen as another manifestation of topology in the quantum Hall effect because the anyonic phase is independent of the details of the path taken, as depicted in Fig. 1.4.

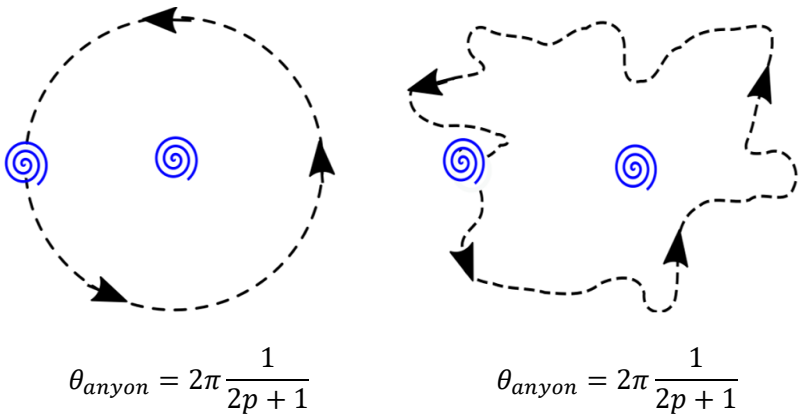

Fig. 1.4. **Cartoon showing two paths for one quasiparticle around another.** Because anyon braiding in the fractional quantum Hall regime is topological phenomenon, the two paths result in the same phase θ_{anyon}

1.7 Interferometry

While bulk semiconductor samples such as the one shown in Fig. 1.2b can be used to observe quantization of the Hall resistance, much smaller, mesoscopic devices are required to detect the exotic properties of quasiparticles. Electronic Aharonov-Bohm interferometry has been proposed as a method to probe quantum Hall edge states [36,38–40]. Three distinct geometries have been proposed: antidot interferome-

ters (shown in Fig. 1.5a), Mach-Zehnder interferometers (Fig. 1.5b), and Fabry-Perot interferometers (Fig. 1.5c). All three varieties of interferometers share similar features. Interferometers take advantage of the fact that in the quantum Hall regime, current is carried by chiral edge states, making it straightforward to define an interference path. They all utilize two quantum point contacts (QPCs) to partially backscatter incident edge states (analogous to beamsplitters used in optical interferometers). In typical devices, the QPCs and interference path are defined using metal gates patterned on the semiconductor surface; when the gates are negatively biased the electrons underneath the gate are depleted, causing the edge states to be directed in the desired path. For electrons the phase difference between the two paths is given by the Aharonov-Bohm phase, which is proportional to the encircled magnetic flux: $\theta = 2\pi \frac{A_I B}{\Phi_0}$. Here, A_I is the area of the interference path, B is the magnetic field, and $\Phi_0 \equiv \frac{h}{e}$ is the magnetic flux quantum.

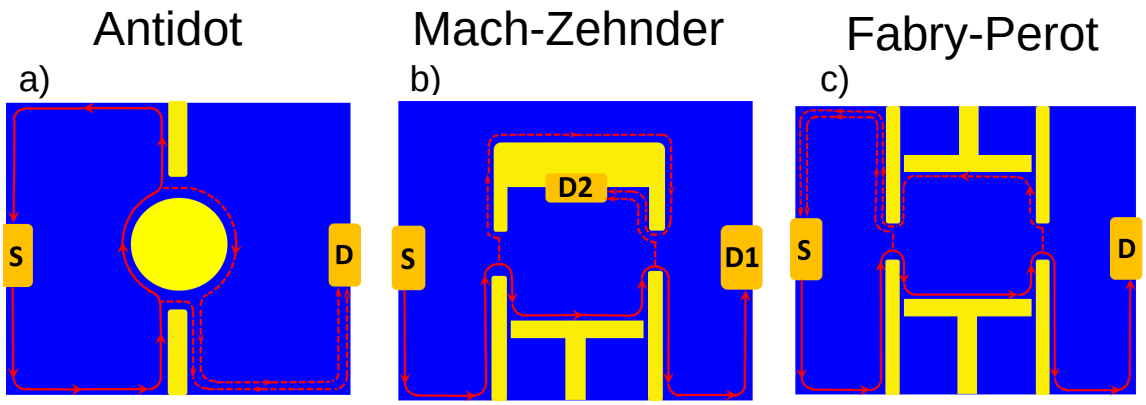

Fig. 1.5. **Different types of quantum Hall interferometers.** (a) Schematic of an antidot interferometer. The source contact S and drain D are labeled; metal gates to define the interference path are shown in yellow. The chiral edge states are shown with red lines; the dashed red lines represent the backscattered paths from the two QPCs. (b) Schematic of a Mach-Zehnder interferometer. (c) Schematic of a Fabry-Perot interferometer.

While antidot devices have been investigated in a few previous experiments [41,42], Mach-Zehnder and Fabry-Perot devices have drawn more theoretical and experimental interest due to their potential to measure the fractional charge and anyonic braiding statistics of quasiparticles in fractional quantum Hall states. Mach-Zehnder devices are more difficult to fabricate and in previous experiments [43, 44], they have failed to yield any interference at fractional quantum Hall states. For these reasons, I have decided to work with Fabry-Perot type interferometers.

For Fabry-Perot interference of a fractional state with quasiparticles bearing charge e^* and statistical phase θ_{anyon}, the interference phase θ is modified [36]:

$$\theta = 2\pi \frac{e^*}{e} \frac{A_I B}{\Phi_0} + N_L \theta_{anyon} \tag{1.3}$$

In Eqn. 1.3 N_L is the number of quasiparticles localized inside the interference path. From this equation, it is clear that both the fractional charge and fractional braiding statistics can be accessed (at least in principle) from Fabry-Perot interference.

1.8 Operation of Fabry-Perot Interferometers

When the gates of a Fabry-Perot electronic interferometer are negatively biased and edge states are partially reflected by the two quantum point contacts, as shown schematically in Fig. 1.5c, quantum interference will occur between the two backscattered paths. The interference will modulate the current through the device, and thus can be probed by measuring the conductance or resistance across the device. For integer quantum Hall states the phase is simply the electronic Aharonov-Bohm phase, $\theta = 2\pi \frac{A_I B}{\Phi_0}$. There are two ways of operating such a device; the area A_I can be changed by changing the voltage V_{gate} on the side gates (more negative voltage will reduce the area and thus reduce the magnetic flux), or the magnetic field B can be changed by controlling the current through a superconducting magnet.

Since the phase is proportional to both A_I and to B, if one does the experiment of measuring conductance as a function of both magnetic field and gate voltage the naively expected behavior is that the lines of constant phase should have *negative* slope as a function of V_{gate} and B. Furthermore, since the area A_I is not expected to depend significantly on B, it is expected magnetic field oscillation period ΔB should be constant and equal to $\frac{\Phi_0}{A_I}$; on the other hand, the change of phase when changing A_I is proportional to B, so the gate voltage period ΔV_{gate} should be *inversely proportional* to B (it will also depend on the lever arm $\frac{\partial A_I}{\partial V_{gate}}$ that relates a change in gate voltage to a change in area, and is assumed to be nearly independent of magnetic field).

Early experiments with Fabry-Perot devices, however, showed exactly the opposite of the expected behavior. When sweeping the magnetic field and gate voltage, lines of constant phase/constant conductance were found to have *positive* slope rather than the expected negative slope [45–47]. The oscillation periods ΔB and ΔV_{gate} were also inconsistent with the expected behavior; rather than being a constant, the magnetic field period ΔB was found to be proportional to $\frac{1}{B}$, and the gate voltage period ΔV_{gate} was found to be nearly constant - once again, exactly the opposite of expected behavior!

Theoretical works explained this unexpected behavior as being due to Coulomb charging effects in the device [36, 40]. When the magnetic field is increased, the degeneracy of each Landau level also increases, leading to an increase in electron sheet density for each fully occupied Landau level, and thus an increase in the charge in the bulk of the device $\delta q_{bulk} = \frac{e\nu\overline{A}\delta B}{\Phi_0}$ (here $\overline{A}$ is the average area to which small changes δA_I are made and B is the starting magnetic field to which small changes δB are made). However, for a small device there is a large electrostatic energy cost for increasing charge in the device, so the area of the interfering Landau level decreases to compensate; this results in a change in charge at the edge $\delta q_{edge} = \frac{e\delta A_I B}{\Phi_0}$. Strong Coulomb charging effects will force the total charge to be zero so $\delta q_{bulk} + \delta q_{edge} = 0$. This gives a change in area of the interference path $\delta A_I = -\frac{\nu\overline{A}\delta B}{B}$.

The change in flux, $\delta\Phi$, will be a combination of the change in area and the change in magnetic field: $\delta\Phi = \overline{A}\delta B + B\delta A = \overline{A}\delta B - \nu\overline{A}\delta B = (1-\nu)\overline{A}\delta B$. Since for integer quantum Hall states $\nu \geq 1$, this implies that the flux through the interference path actually *decreases* if the magnetic field is increased (and vice versa)! This explains the positive slope of constant phase lines observed in experiments. Devices which exhibit this positive slope (or zero slope in the case of $\nu = 1$) due to Coulomb effects are referred to as "Coulomb-dominated."

These Coulomb charging effects extend to the fractional quantum Hall regime as well, but there is an additional problem: it has been shown that in the Coulomb dominated regime, the anyonic braiding phase is unobservable [36]. This is because the anyonic phase depends on braiding the edge quasiparticles around the fractional charge of the quasiparticles localized in the interference path; however, in a Coulomb dominated device the enclosed charge is fixed, so no discrete phase jumps can occur (what will happen is that the area of the device will vary in just such a way that the anyonic phase is cancelled by the Aharonov-Bohm phase, making the anyonic contribution unobservable). Due to this problem, it is necessary to reduce Coulomb charging effects to prevent Coulomb dominated behavior and enable devices to operate in the "Aharonov-Bohm (AB) regime", where conventional Aharonov-Bohm behavior may be observed.

It turns out that the Aharonov-Bohm regime is difficult to achieve; if one jumps into these types of experiments, it is very likely that devices will be Coulomb dominated (at least at first). This is exactly what happened to me. On the other hand, in previous experiments it was demonstrated that it is possible to recover Aharonov-Bohm behavior. This was achieved by making device dimensions very large, $\approx 20\mu\text{m}^2$ (which makes the Coulomb interaction between electrons in the bulk and electrons at the edge weaker), and by adding a metal gate over the middle of the device; this metal gate is kept at ground potential and acts to screen Coulomb effects in the device [45, 46]. The major problem with these types of devices is that due to their large size, coherence is very weak, making the interference signal small. Most impor-

tantly, interference was only able to measured at integer quantum hall states, and no interference was able to be measured at any fractional quantum Hall states. From these experiments, it was clear that more effective screening was needed to achieve Aharonov-Bohm behavior in much smaller devices.

Another technique for suppressing Coulomb charging was presented in [48], in which an annealed Ni/Au/Ge Ohmic contact was placed in the center of the interferometer. Since this contact provides a conduction path in the middle, the bulk of the device does not accumulate charge as magnetic field is varied, enabling it to operate in the Aharonov-Bohm regime despite a much smaller size ($\approx 2.6\mu m^2$). However, no interference at fractional quantum Hall states was reported in this type of device. A possible problem with this scheme is that annealed Ni/Au/Ge contacts are believed to work by spiking metal into the semiconductor to create contact; putting such a contact right in the middle of a device is likely to create a tremendous amount of disorder which would destroy the relatively fragile fractional states, making fractional interference impossible.

1.9 Screening Well Heterostructure

When I started working on quantum Hall interferometers, it was clear that interferometer coherence needed to be significantly improved for progress to be made in the field, since previous experiments showed poor coherence at integer quantum Hall states and no interferene at fractional states. Assuming that the system has a finite coherence time limited by thermal smearing or thermal noise, there are three ways one could envision improving the situation: 1)Reduce the electron temperature so that coherence time is longer 2)Increase the edge state velocity to reduce time spent in the interferometer relative to the coherence time 3)Reduce the interferometer size so that time spent traversing the interference path is shorter. Since we already operate a dilution refrigerator with a base temperature of around 10mK, option 1) seemed unlikely to yield large returns since refrigerators with significantly lower temperatures are not

readily available (although it is possible that in our samples the electron temperature may be higher than the fridge temperature, in which case there would be gains to be made by improving coupling of the electrons to the fridge). Option 2) seemed like a more promising avenue. Since edge currents are driven by the electric field at the edge of the sample, edge velocity can (in principle) be increased by increasing the sharpness of the confining potential in the device. I initially tried to make devices with a "helper" gate which would be positively biased in order to make the confining potential sharper, but this scheme utterly failed to improve interference. So, I had to come up with something else.

Because I have had the good fortune of working in a group with amazing capabilities in the field of GaAs MBE growth, I decided to approach the problem of quantum Hall interferometry from the perspective of heterostructure engineering. From this line of thinking I came up with the idea of the "screening well" heterostructure. The idea of this structure is that while a typical GaAs/AlGaAs heterostructure has a single 2DES located in a GaAs quantum well or at an interface, the screening well structure would utilize one or two extra quantum wells with their own 2DESs. These auxilliary wells would conduct and play the same role as the metal gates used to screen Coulomb effects in previous experiments, but the screening effect can be greatly improved because, due to being grown as a part of the structure, the screening wells can be located much closer to the 2DES than the metal gate could be, and if two screening wells are used, the screening can be done from both sides. One might ask "couldn't we simply grow a structure where the 2DES is located very close to the surface, and then get improved screening from a metal top gate?", but it turns out that if the 2DES is shallow, disorder from the surface will make it very low quality and it will not support fractional quantum Hall states.

However, there is a major problem with this screening well idea. The problem is that if there are electrons in the screening wells available to screen, they will also be an additional source of conduction parallel to the main quantum well. Parallel conduction is a huge problem for samples used for quantum Hall experiments because

the parallel conduction obscures the states in the primary quantum well that we want to observe in electronic transport measurements. Sometimes, when growing conventional GaAs heterostructures, a little bit of parallel conduction arises unintentionally, and this causes us to fret about what might have gone wrong in the growth, but here we are *intentionally* inducing a large amount of parallel conduction! This is not a problem that can easily be swept under the rug.

One way to deal with this issue is to keep the electron density low. If the density is very low, then the electrons in the screening well can have low enough conductivity that parallel conduction through them does not appear in transport measurements; sometimes there is parallel conduction at low field, but it freezes out at high field (possibly due to the very low filling factor causing Wigner crystallization of electrons in the screening wells). The hope was that the electrons would be conductive enough to cause screening (on the long time scale of the measurement) but not mobile enough to cause observable parallel conduction. So, we grew a double screening well structure with an estimated density of $\approx 4 \times 10^{10}\text{cm}^{-}2$ in each screening well. As we hoped, there was no parallel conduction. However, there was also no screening effect; interferometers made with this wafer all turned out to be Coulomb dominated. My conclusion is that parallel conduction is a necessary evil if we want screening to really work.

Things only began to work once we designed and grew a structure with much higher density in the screening wells such that there *was* significant parallel conduction. The layer stack for this structure is shown in Fig. 1.6a, and the simulated band structure is shown in 1.6b [4]. This structure has density in the screening wells comparable to that in the main quantum well, making parallel conduction unavoidable. But this did the trick: we were able to measure Aharonov-Bohm regime interference in a very small device with area $\approx 0.9\mu\text{m}^2$, an order of magnitude smaller than is possible with only screening by a metal top gate. Due to the small size of the device, the interference amplitude was very large and easy to measure. While this was a good proof of principle, the problem of parallel conduction remained; in fact, it was never

clear whether we were measuring interference of electrons in the main quantum well or of electrons in one of the screening wells. In order to get a convincing and publishable result, we had to eliminate parallel conduction through the screening wells while still maintaining their ability to screen; our scheme for doing this is detailed in the Chapter 2.

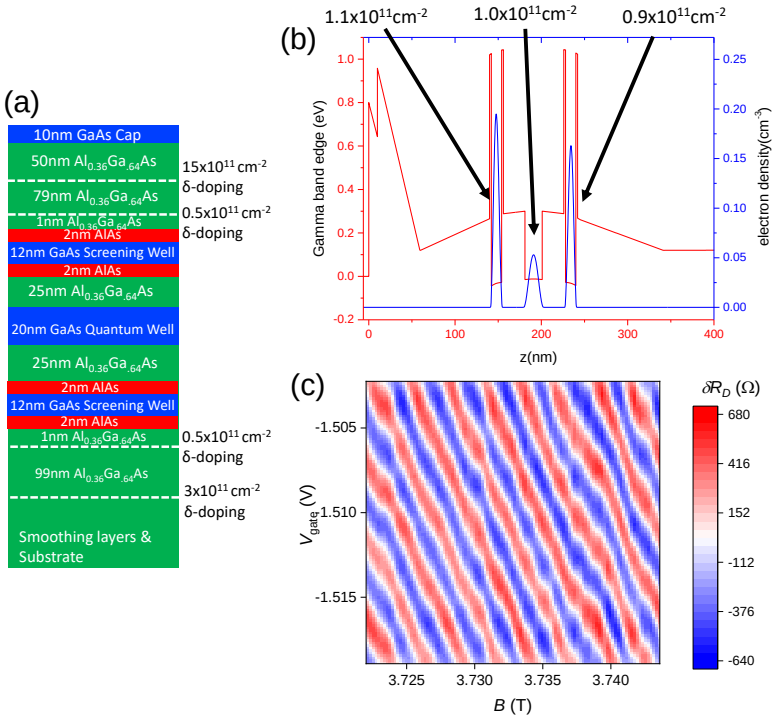

Fig. 1.6. **Screening well heterostructure.** (a) Layer stack showing the GaAs/AlGaAs heterostructure design using screening wells. In addition to the primary 20nm GaAs quantum wells, electrons also populate auxiliary 12nm screening wells which flank the quantum wells and serve to screen Coulomb effects in the interferometer. (b) Simulation of the conduction band minimum (shown in red) and electron density (shown in blue) along the growth direction for the structure in (a). (c) Pajama plot showing AB interference for a small interferometer with effective area $\approx 0.9\mu\text{m}^2$. The negative slope of the constant phase lines indicates that the screening wells have succeeded at suppressing Coulomb charging effects in the device.

2. AHARONOV-BOHM INTERFERENCE OF FRACTIONAL QUANTUM HALL EDGE STATES

A version of this chapter was previously published by *Nature Physics* [49].

2.1 Abstract

We demonstrate operation of a small Fabry-Perot interferometer in which highly coherent Aharonov-Bohm oscillations are observed in the integer and fractional quantum Hall regimes. Using a novel heterostructure design, Coulomb effects are drastically suppressed. Coherency of edge mode interference is characterized by the energy scale for thermal damping, $T_0 = 206mK$ at $\nu = 1$. Selective backscattering of edge modes originating in the $N = 0, 1, 2$ Landau levels allows for independent determination of inner and outer edge mode velocities. Clear Aharonov-Bohm oscillations are observed at fractional filling factors $\nu = 2/3$ and $\nu = 1/3$. Our device architecture provides a platform for measurement of anyonic braiding statistics.

2.2 Background

Integer and fractional quantum Hall states are archetypal topological phases of a two-dimensional electron system (2DES) subjected to a strong perpendicular magnetic field [29]. Electronic Fabry-Perot interferometry has been proposed as a means to probe the properties of integer and fractional quantum Hall edge states [38, 39, 50, 51]; most intriguingly, interferometry may be used to directly observe anyonic braiding statistics [37] of fractional quantum Hall quasiparticles. Interference visibility in real devices is limited by finite phase coherence, a particularly acute problem in the fractional quantum Hall regime. Visibility may be improved by decreasing the size

of the interferometer so that the path traveled by interfering excitations is shorter. However, attempts to measure interference in small devices have yielded results inconsistent with simple Aharonov-Bohm interference; specifically, the magnetic field oscillation period is found to change with filling factor, and constant phase lines in the gate voltage-magnetic field plane have positive slope rather than the expected negative slope [45, 46, 52, 53]. This behavior is attributed to Coulomb charging effects [40, 40], which cause the area of the interferometer to change as the magnetic field is varied. This "Coulomb-dominated" behavior masks the Aharonov-Bohm phase and makes braiding statistics unobservable [40]. The effects of intermediate Coulomb coupling have also been investigated theoretically [54]. The challenge for measuring robust interference and observing fractional braiding statistics is to create a device small enough to maintain phase coherence, while reducing Coulomb effects so that the device may operate in the Aharonov-Bohm regime. We report fabrication and operation of an interferometer that overcomes these challenges.

2.3 Screening Well Structure

The GaAs/AlGaAs heterostructure was grown by molecular beam epitaxy [1, 3] and is shown in Fig. 2.1a. While typical structures utilize a single GaAs quantum well in which the 2DES resides, our structure contains three GaAs wells: a primary quantum well 30nm wide and two additional 12nm wells located on either side of the primary well separated by 25nm $Al_{0.36}Ga_{0.64}As$ spacers. The 2DES under study is located inside the primary GaAs quantum well, while the ancillary wells screen Coulomb effects so that the interferometer may operate in the Aharonov-Bohm regime [36, 40]. The structure is modulation doped with silicon above the top screening well and below the bottom screening well. In Fig. 2.1b we show the position of the Γ-band edge (red) and electron density (blue) calculated by the self-consistent Schrodinger-Poisson method [55]; the confinement energy in each screening well is tuned to match the experimentally measured densities. This structure is designed to have significantly

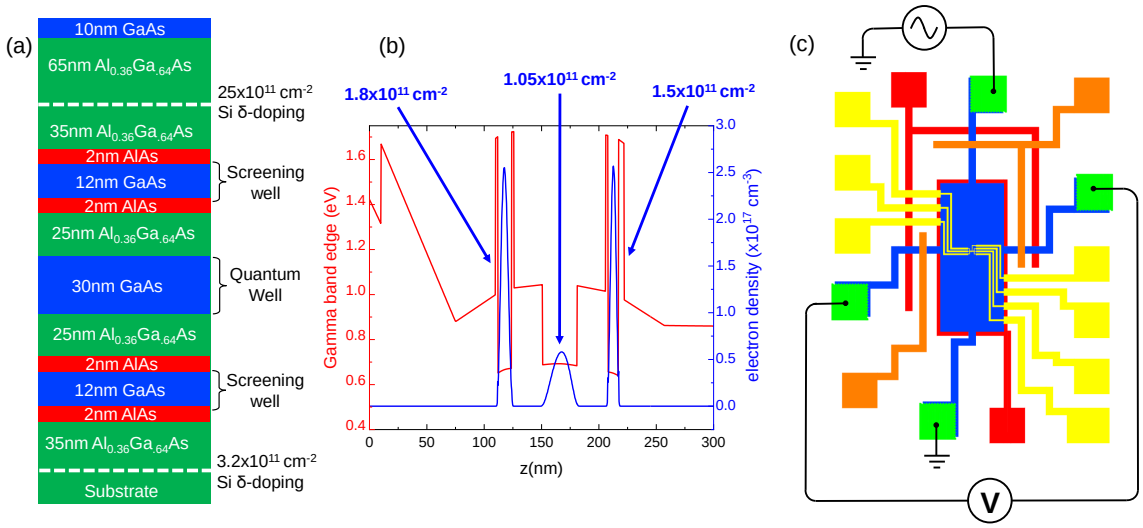

Fig. 2.1. **Heterostructure design and device layout.** (a) Layer stack of the GaAs/AlGaAs heterostructure along the growth direction, showing the positions of the GaAs quantum well and screening wells (blue), AlGaAs spacers (green), and AlAs barriers (red). (b) Conduction band edge (red) and electron density (blue) versus growth direction (z-axis) calculated using a self-consistent Schrodinger-Poisson method. The sheet density in each well is indicated. (c) Schematic showing the layout of the mesa (blue), Ohmic contacts (green), surface gates used to isolate the top screening well from the contacts (orange), and the backgate used to isolate the contacts from the bottom screening well (red). The surface gates used to define the interference path are shown in yellow. Additionally, there is a global backgate underneath the mesa (red). A four-terminal measurement circuit is indicated in which current is injected into the Hallbar and the perpendicular Hall voltage is measured; when the interferometer gates are biased to define the interference path, the measured resistance is referred to as the diagonal resistance, R_D.

higher density in the screening wells than in the primary well in order to facilitate strong screening.

In Fig. 2.2 we show a scanning electron microscopy (SEM) image of the interferometer gates. The device consists of two quantum point contacts (QPCs) that form narrow constrictions and a pair of side gates that define the interference path. The

gates shown in yellow are negatively biased to deplete electrons from the quantum well and define the interference path; the central top gate (green) is grounded and does not alter the 2DES density.

Interferometer operation requires transport measurements through the primary quantum well unobscured by parallel conduction through the screening wells. Our device includes narrow gates on the top surface and on the back side of the chip that partially overlay the arms connecting each Ohmic contact to the mesa; this is shown schematically in Fig. 2.1c. The surface gates over the Ohmics are negatively biased at -0.29V; this bias is sufficient to deplete the electrons from the top screening well without depleting either the primary quantum well or the bottom screening well. Similarly, the back side gate over the Ohmics is biased at -150V in order to deplete the bottom screening well, but not the primary quantum well. This eliminates electrical conduction through both screening wells so that only the primary quantum well is probed in measurements. Because these gates are well separated from the gates that define the mesoscopic interference path, the screening wells are still populated in the interferometer and thus available to screen. In Fig 2.3a we show the evolution of the Hall resistance R_{xy} with current allowed to flow through all three wells (black trace), with the top screening well disconnected from the contacts (blue trace), and with both screening wells disconnected such that current passes only through the primary quantum well (red trace); in the final case R_{xy} exhibits a much steeper slope and shows clear quantum Hall plateaus and concomitant zeroes in longitudinal resistance (not shown), demonstrating that parallel conduction through the screening wells has been eliminated. This selective depletion technique was pioneered to isolate transport in bulk bilayer systems [56]. Here we have demonstrated the technique has utility for mesoscale electronic devices as well.

The presence of the screening wells acts to reduce the Coulomb charging energy, characterized by measuring Coulomb blockade through the device at zero magnetic field [57]. Coulomb blockade diamonds (obtained by measuring the differential conductance $\frac{\partial I}{\partial V}$ versus side gate voltage V_{gate} and source drain voltage V_{SD}), shown in

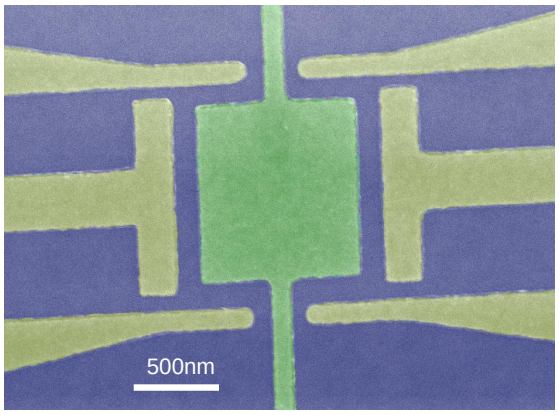

Fig. 2.2. **Scanning Electron Microscope image of interferometer**. False color SEM image of the interferometer, located in the center of the Hall bar shown schematically in Fig. 1c. The device consists of two quantum point contacts to backscatter current and a pair of side gates to define the interference path (yellow); when these gates are negatively biased, the 2DES underneath is depleted, which defines the interference path. In the measurements, the gate voltage V_{gate} applied to both side gates is varied in order to change the area of the interference path. An additional gate over the top of the area of the device (green) is grounded for these experiments.

Fig 2.3b, yield a charging energy $\frac{e^2}{2C} \approx 17\mu$eV. The Coulomb blockade charging energy characterizes the incremental increase of electrostatic energy when an electron is added in the presence all of the other electrons localized in the interior of the device; therefore, this energy may be loosely identified with the bulk-edge coupling constant K_{IL} in Ref. [36], which determines whether the device is in the Coulomb-dominated or Aharonov-Bohm regime. A similarly sized device *without* screening wells would have charging energy $\frac{e^2}{2C} \sim \frac{e^2}{\epsilon r} \approx 200\mu$eV (where r is the radius of the dot), indicating that the screening wells are very effective at reducing Coulomb effects in the interferometer (Coulomb blockade from a device without screening wells is shown in Fig. 2.4). It is important to note that although Coulomb effects are screened on the scale of the mesoscopic device, the presence of several fractional quantum Hall plateaus visible in Fig. 2.3a indicates that the Coulomb interaction on the microscopic length scales relevant for the fractional quantum Hall effect is not significantly reduced.

2.4 $\nu = 1$ interference

Next, we operate the device at filling factor $\nu = 1$ in the integer quantum Hall regime, where the bulk of the 2DES is insulating and current is carried by a chiral edge state. The interference path is shown schematically in Fig. 2.6a. Electrons incident from the source contact are backscattered by the two quantum point contacts to the opposite edge, and the two backscattered paths interfere; this is shown schematically in Fig. 2.6a. The quantum mechanical phase difference between the two interfering paths is given by the Aharonov-Bohm phase: $\theta = 2\pi\frac{A_I B}{\Phi_0}$, where A_I is the area of the interference path, B is the magnetic field, and $\Phi_0 \equiv \frac{h}{e}$ is the magnetic flux quantum. The device may be operated by changing the magnetic field B, or by changing the voltage on the side gates to change A_I. the nee At $\nu = 1$ the interferometer exhibits strong conductance oscillations, probed by measuring the diagonal resistance R_D across the device. R_D as a function of gate voltage and magnetic field is plotted in Fig. 2.6b; the lines of constant phase exhibit negative slope, consistent with the

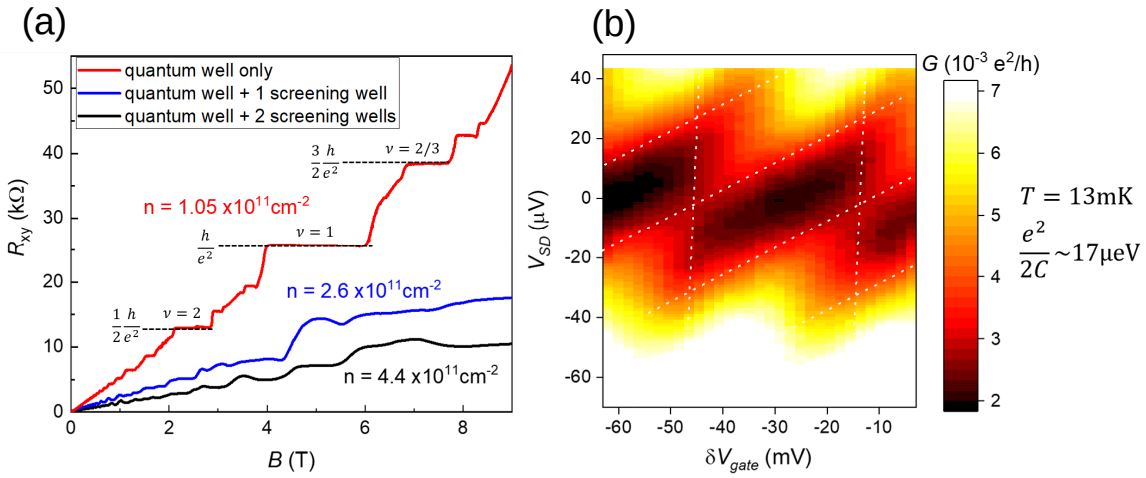

Fig. 2.3. **Bulk magnetotransport and Coulomb blockade.** (a) Bulk Hall conductance R_{xy} with the top and bottom gates around the contacts grounded (black trace), with -0.29V on the top gate to disconnect the top screening well from the contacts (blue), and with -0.29V on the top gate and -150V on the back gate around the contacts in order to disconnect both screening wells from the contacts so that transport is only measured through the primary quantum well (red). The red trace is taken at temperature $T = 13$mK, and the blue and black traces are taken at $T = 300$mK. (b) Coulomb blockade measurement at zero magnetic field measured in a dilution refrigerator at base temperature $T = 13$mK showing the differential conductance $\frac{\partial I}{\partial V}$ versus gate voltage and source-drain voltage V_{SD} for the device at zero field showing Coulomb blockade diamonds with charging energy $\frac{e^2}{2C} \sim 17\mu$eV. δV_{gate} is relative to -1.8V.

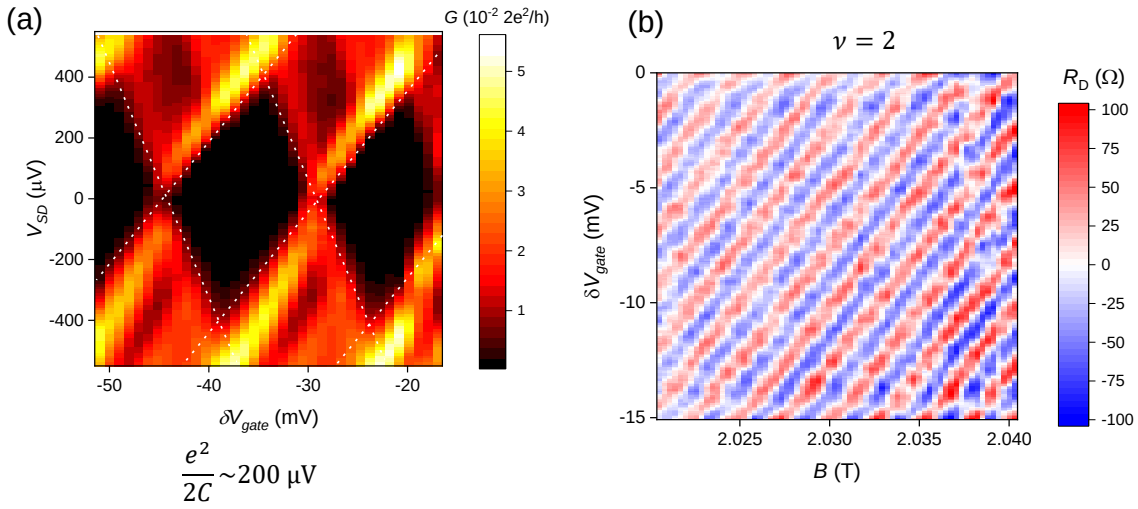

Fig. 2.4. **Coulomb-dominated measurements in devices without screening wells.** (a) Differential conductance measurements from a device without screening wells. The device has a radius of 800nm, making it comparable in size to the device presented in the main text, but it has a Coulomb charging energy (extracted with the height of the diamond pattern) $e^2/2C \sim 200\mu$V, an order of magnitude larger than the device with screening wells. (b) Resistance oscillations from another device made on a wafer without screening wells in the quantum Hall regime at filling factor $\nu_{bulk} = 2$. The positive slope of the constant-phase lines is a signature of Coulomb-dominated behavior which is pervasive in devices without screening wells.

device being in the Aharonov-Bohm regime despite its small size. The magnetic field oscillation period $\Delta B = 5.7$mT, which gives an area of the interference path $A_I = \frac{\Phi_0}{\Delta B} \approx 0.73\mu\text{m}^2$. This area is smaller than the lithographic area of the device, indicating that the 2DES is depleted in a region approximately 180nm wide around the gates; this agrees with simulations of the 2DES density at the edge of the gate (see Fig. 2.5). Additionally, we find that ΔB does not vary significantly with filling factor in the range $1 \leq \nu \leq 12$, consistent with Aharonov-Bohm behavior and in contrast to the Coulomb-dominated regime in which ΔB is proportional to $\frac{1}{\nu}$ [36,40,45,46]. Previous Fabry-Perot interferometry experiments utilizing conventional heterostructures have required a device area of $20\mu m^2$ in order for Coulomb effects to be small enough for the device to be in the Aharonov-Bohm regime [45, 46]; unambiguous observation of the Aharonov-Bohm regime in a much smaller device demonstrates the effectiveness of the device design employed here.

For weak backscattering by symmetrically tuned QPCs, conductance oscillations due to interference obey $G/G_0 = 1 - 2r^2[1 + \eta\cos(2\pi\frac{AB}{\Phi_0})]$, where $G = \frac{1}{R_D}$ is the conductance across the device, $G_0 \equiv \frac{e^2}{h}$ is the conductance quantum, r^2 is the reflection probability of the QPCs, and η is the coherence factor. We characterize coherence of the interference at $\nu = 1$ by measuring conductance oscillations at different cryostat temperatures, plotted in Fig. 2.6c; we normalize by dividing by the conductance oscillations δG by the reflection amplitude r^2, with each QPC tuned to approximately 97% transmission and 3% reflection. The coherence factor η (defined as the amplitude of $\frac{\delta G}{2G_0 r^2}$) decays with temperature following an approximately exponential trend, shown in Fig. 2.6d, with a characteristic temperature $T_0 = 206$mK. For comparison, in measurements of a Fabry-Perot interferometer in [58] T_0 was found to be < 20mK for magnetic fields exceeding 1.5T; in measurements of Mach-Zehnder interferometers the largest T_0 measured was 40mK [59], with larger devices exhibiting smaller T_0. The significantly larger T_0 observed in our experiment indicates that the smaller size achieved in our device is beneficial to achieving quantum coherence.

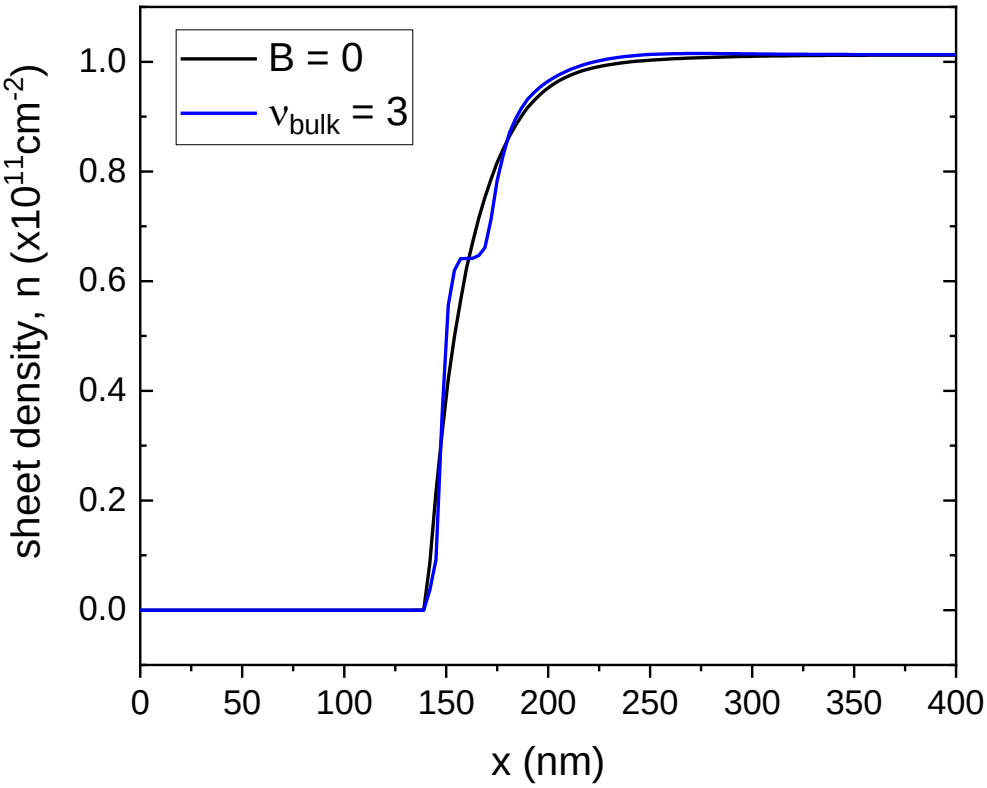

Fig. 2.5. **Simulation of the electron sheet density at the edge of the gate.** Electron sheet density is plotted versus lateral distance x from the gate at zero magnetic field (black line) and at $\nu_{bulk} = 3$ (blue line). The edge of the gate is located at $x = 0$. For the simulation the gate bias is set at -1.8V to match the experimental side gate bias. The simulation indicates that the 2DES is depleted in a region extending approximately 150nm from the edge of the gate, which is consistent with the experimental finding that the effective area extracted from Aharonov-Bohm oscillations is smaller than the lithographic area.

2.5 Edge mode velocity

When the device is operated at lower magnetic field (higher filling factor), multiple integer edge modes are present. In our device it is possible to selectively interfere a particular edge mode by tuning the QPC voltages to partially backscatter that

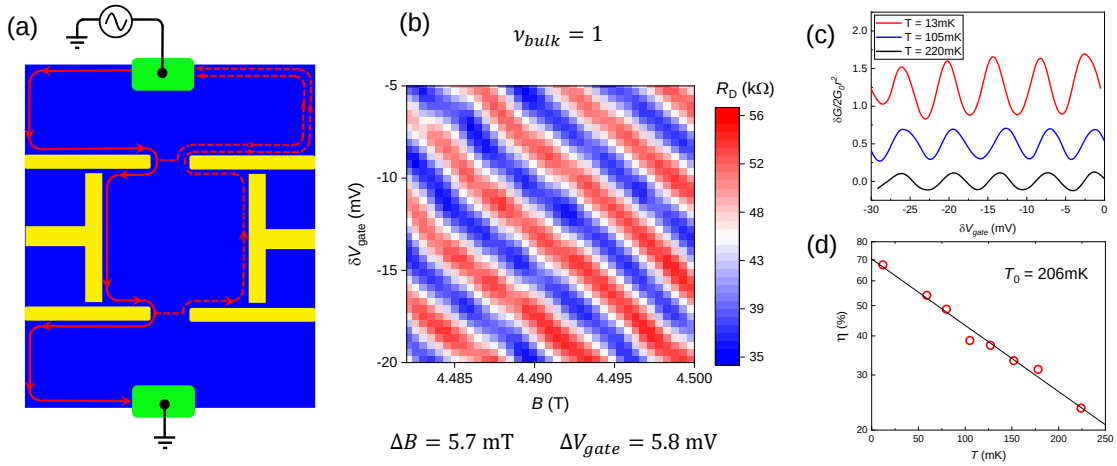

Fig. 2.6. **Interference measurements at $\nu = 1$.** (a) Schematic showing the interference path defined by the interferometer gates at $\nu = 1$. (b) Resistance oscillations as a function of magnetic field B and side gate voltage δV_{gate} (relative to -1.4V) showing clear Aharonov-Bohm interference. For this measurement the QPCs are biased to achieved approximately 25% reflection. (c) Oscillations in conductance through the device, δG, divided by the QPC backscattering amplitude, r^2, at 13mK (red), 105mK (blue), and 220mK (black). For these measurements each QPC is tuned to approximately 97% transmission and 3% reflection ($r^2 = 0.03$). The amplitude of the oscillations clearly decreases as cryostat temperature is increased. (d) Coherence factor η versus temperature; η shows an approximately exponential dependence on temperature with a characteristic decay scale of 206mK.

edge, while fully transmitting the outer edges so that only the partially backscattered edge interferes; this is shown schematically in Fig. 2.8a for the case of bulk filling factor $\nu_{bulk} = 3$, and a corresponding trace of the QPC conductance versus gate voltage is shown in Fig. 2.8b with the operating points corresponding to the selective interference of each edge mode indicated with colored circles.

The interference phase may be additionally modulated by changing the energy ϵ of injected electrons, which changes the wave-vector k. This introduces a phase shift $\delta\theta = \delta\epsilon \frac{\partial k}{\partial \epsilon} L = \frac{\delta \epsilon L}{\hbar v_{edge}}$, where L is the path length around the interference loop and

$v_{edge} \equiv \frac{1}{\hbar}\frac{\partial \epsilon}{\partial k}$ is the velocity of the edge mode [38]. ϵ may be modulated by applying a finite source-drain bias V_{SD} across the device; this results in oscillations in differential conductance as a function of both V_{SD} and flux: $\delta G \propto \cos(2\pi\frac{AB}{\Phi_0})\cos(\frac{eV_{SD}L}{2\hbar v_{edge}})$ [60]. This results in nodes in a "checkerboard" pattern when δG is measured in the V_{SD} - V_{gate} plane (plotted at $\nu_{bulk} = 1$ in Fig. 2.8c and for the inner N = 1 mode at $\nu_{bulk} = 3$ in Fig. 2.8d), with nodes in the interference pattern occurring at $V_{SD} = \pm\frac{\pi\hbar v_{edge}}{eL}$. The velocity may thus be extracted: $v_{edge} = \frac{eL\Delta V_{SD}}{2\pi\hbar}$ [44, 60], where ΔV_{SD} is the spacing between nodes, and we estimate L from the interference area, $L \approx 4\sqrt{A_I}$. The extracted velocity likely represents the average velocity of the edge mode in the interferometer since there may be local variations in the confining potential and thus velocity.

In Ref. [60] this method was used to measure edge velocity versus filling factor, but without controlling which edge mode was being interfered; in [44] edge velocity for only the $N = 0$ Landau Level (LL) was reported (where $N = 0, 1, 2...$ is the LL index). To our knowledge, measurement of edge velocity for different LLs as a function of filling factor has not been demonstrated previously. In Fig. 2.8e we plot the edge state velocity for the $N = 0$, $N = 1$, and $N = 2$ LL edge modes versus bulk filling factor ν_{bulk}. The inner, higher index Landau levels generally have lower velocity and correspondingly lower coherence. At magnetic fields below approximately 1.2T ($\nu_{bulk} = 4$), the QPCs show spin-degenerate conductance plateaus, even though the bulk transport exhibits spin-split quantum Hall states down to 0.2T. This suggests that although distinct edge states exist, below 1.2T they are too close to one another to be interfered independently; therefore at filling factors $v_{bulk} > 4$ we show a single velocity measurement for each Landau level, while at lower fillings we show both spins when resolved. We also mention that we observe the same period-halving phenomenon in our device that was reported in previous interferometry experiments [61–63]; see Fig. 2.7.

Much of the magnetic field dependence in Fig. 2.8e can be understood from the fact that edge currents in the quantum Hall regime are generated by Hall drift:

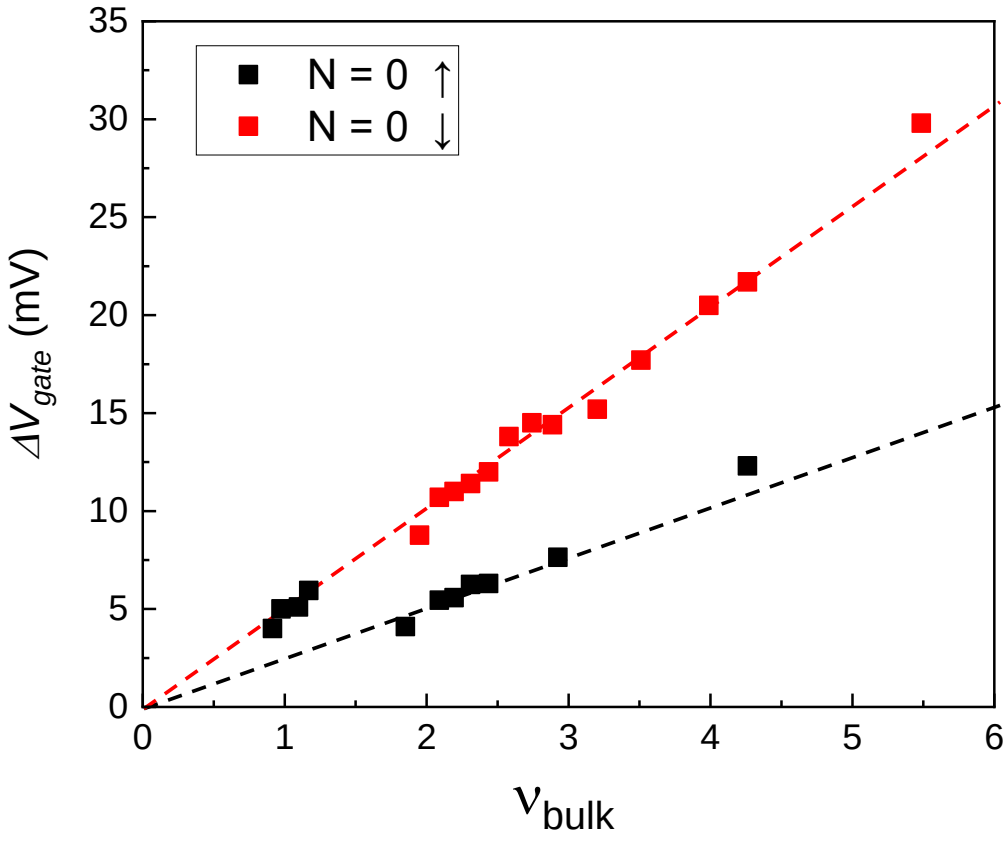

Fig. 2.7. **Period-halving phenomenon in in the Fabry-Perot interferometer.** Gate voltage period ΔV_{gate} versus bulk filling factor ν_{bulk} for the N = 0 Landau level spin-up (black squares) and spin-down (red squares) edge states. The red line indicates a linear fit through zero of spin-up data points for $\nu_{bulk} \leq 1.8$ as well as all the spin-down data points. The black dashed line indicates a linear fit through the spin-up data points for $\nu > 1.8$. The red dashed line has a slope of 5.12 mV, while the black dashed line has a slope of 2.57 mV, which is consistent with N = 0 spin-up LL edge state exhibiting a halved period Aharonov-Bohm behavior when the spin-down edge state is present, consistent with the behavior discussed in Refs. [61, 62].

$\vec{v}_{Hall} = \frac{\vec{E}\times\vec{B}}{B^2}$, where $\vec{E}$ is the in-plane electric field at the edge due to the confining potential and $\vec{B}$ is the perpendicular magnetic field. This implies that the edge velocity should increase with decreasing magnetic field (increasing filling factor), and

this is indeed the predominant trend observed at filling factors $9 < \nu_{bulk} < 2$. On the other hand, it must also be considered that the electric field experienced by each edge state also depends on both magnetic field and Landau level index. It can be seen from Fig. 2.8e that the outer, lower index Landau levels generally have higher edge velocity than the inner, higher index ones. This behavior can be understood from the works of Chklovskii et al. [64, 65], who found that the confining potential is steepest at the outer edge, resulting in a higher electric field and thus higher velocity for the outer Landau level edge modes and a smaller electric field and lower velocity for the inner ones.

Numerical simulations of edge transport in the integer quantum Hall regime for the heterostructure used in these experiments have been performed, and are plotted in Fig. 2.8f; see Ref. [55] for an in-depth review. In these simulations, the spatially varying in-plane electric field is self-consistently evaluated for the Landau level density of states, considering the electrostatic effects of the heterostructure, doping, surface states and gates. The velocity is obtained by solving quantum transport (non-equilibrium Green's function) equations at the Fermi level.

The simulations show good qualitative and quantitative agreement with the experimental results over the range of filling factor $2 < \nu_{bulk} < 10$. At lower filling $\nu_{bulk} < 2$, the edge velocity exhibits non-monotonic behavior, which may be due to the impact of electron-electron interactions which become increasingly important at high magnetic field. Non-monotonic behavior at low filling was also reported in Ref. [44]. Our simulations employ a mean-field Hartree approximation that does not capture many-body effects.

Additionally, the edge velocities also exhibit non-monotonic behavior at high filling $\nu_{bulk} > 10$. A possible explanation for this is that at low fields when the magnetic length becomes comparable to the length scale of the confining potential at the edge, charge transport may occur via skipping orbits, resulting in different behavior than observed at higher fields [60, 66]. It is reasonable for this to occur at $\nu_{bulk} = 10$; here the magnetic length is $\sim$39nm, and simulations indicate that the length scale

of the confining potential is approximately 40nm (see Fig. 2.5). This effect is not captured in the simulations as the magnetic length approaches the Debye length. An alternative possibility is that at high filling where the cyclotron gap is smaller, there may be partial equilibration between the edge modes facilitated by the applied V_{SD}, which would make our assumption of interfering a single edge mode invalid.

2.6 Fractional quantum Hall regime

We turn now to results in the fractional quantum Hall regime. In previous experiments with small Fabry-Perot devices Coulomb-dominated or Coulomb blockade oscillations have been observed in fractional states [45,67–69]. Willet et al. [70,71] reported oscillations at $\nu = 5/2$ consistent with Aharonov-Bohm interference of charge $e/4$ and $e/2$ excitations. However, oscillations with negatively sloped lines of constant phase in the gate voltage-magnetic field plane (a sine qua non of Aharonov-Bohm regime interference) have not been previously reported. Edge modes in the fractional quantum Hall regime are predicted to have remarkably different properties from those in the integer states; in particular, the current-carrying quasiparticles may carry fractional charge. In the fractional case, the Aharanov-Bohm interference phase is modified [36]:

$$\theta = 2\pi \frac{e^*}{e} \frac{A_I B}{\Phi_0} \tag{2.1}$$

As long as the QPCs are not pinched off, the edge modes and the electrons forming the fractional quantum Hall condensate are not localized within the interferometer, so the area A_I should change continuously as the gate voltage is varied. Equation (2.1) indicates that quasiparticle charge may be extracted from gate voltage oscillation periods according to the relationship $\frac{e^*}{e} = \frac{\Phi_0}{B\Delta V_{gate}\frac{\partial A_I}{\partial V_{gate}}}$, where ΔV_{gate} is the gate voltage oscillation period and $\frac{\partial A_I}{\partial V_{gate}}$ is the lever arm relating change in gate voltage to the change in interference path area. $\frac{\partial A_I}{\partial V_{gate}}$ may be determined from the gate voltage period at integer states, where the interfering charge is simply e; a linear fit of ΔV_{gate}

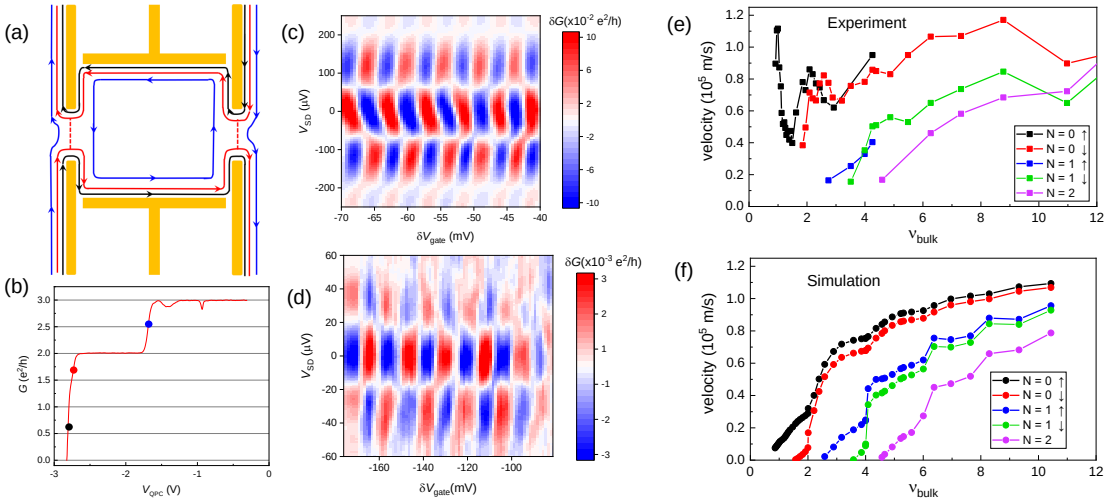

Fig. 2.8. **Edge mode velocity measurements.** (a) Schematic showing an interference path with multiple edge states in which the outermost mode is fully transmitted, the innermost mode is fully backscattered by both QPCs, and the middle mode is partially transmitted by both QPCs; in this configuration only the middle mode is interfered. (b) Conductance versus gate voltage for one QPC at B = 1.64T and $\nu_{bulk} = 3$ with other interferometer gates grounded. The blue, red, and black circles indicate the operating point for interference of the modes associated with $\nu = 3$, $\nu = 2$, and $\nu = 1$ respectively. (c) Differential conductance at $\nu_{bulk} = 1$ interfering the $\nu = 1$ mode and (d) at $\nu_{bulk} = 3$ interfering the innermost $\nu = 3$ mode as a function of side gate voltage and source drain voltage. δV_{gate} is relative to -1.4V. (e) Edge state velocity extracted from the differential conductance oscillations for different edge modes as a function of bulk filling factor. At magnetic fields below approximately 1.2T (bulk filling factor $\nu = 4$) conductance through the QPCs is no longer spin-resolved, so only a single line is displayed for each Landau level. Experimental uncertainty is estimated at ±13%. (e) Numerically calculated edge state velocities for the N = 0, 1, and 2 Landau levels.

versus $1/B$ yields $\frac{\partial A_I}{\partial V_{gate}} = 1.8 \times 10^{-13}\mathrm{m}^2\mathrm{V}^{-1}$. Gate voltage oscillation periods for both integer and fractional quantum Hall states are shown in Fig. 2.9a.

In both the Laughlin [21] and composite fermion [27, 29] theories the $\nu = 1/3$ FQHE state is predicted to support quasiparticles with charge $e^* = e/3$. At $\nu = 1/3$

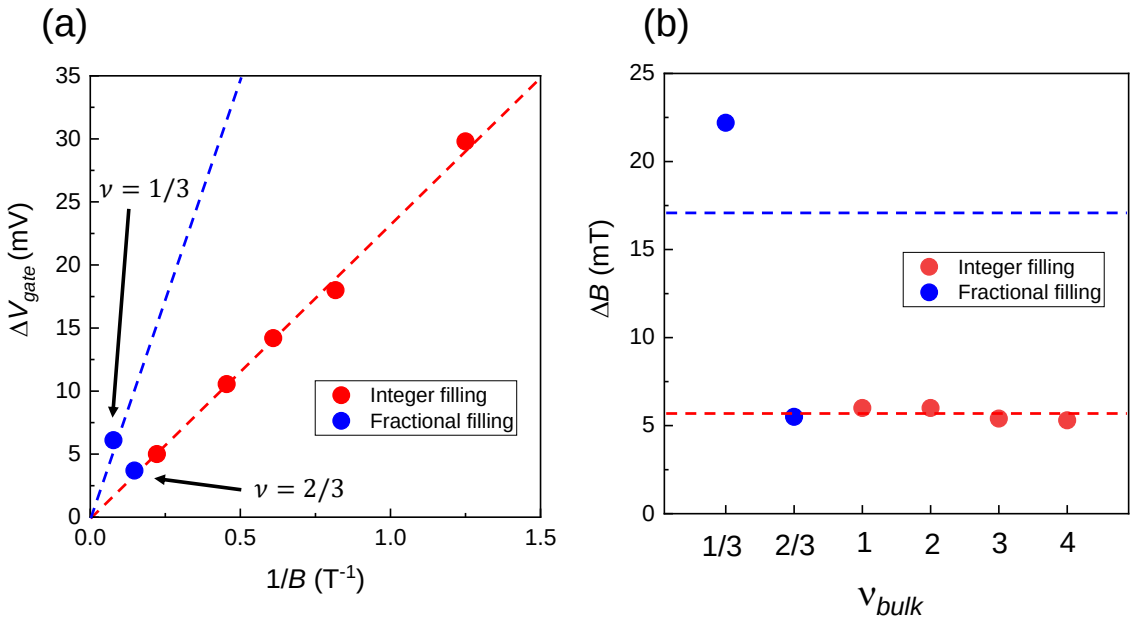

Fig. 2.9. **Side gate and magnetic field oscillation periods for integer and fractional states.** (a) Side gate oscillation period ΔV_{gate} versus inverse magnetic field at integer quantum Hall states (red circles) and fractional quantum Hall states (blue circles). The dashed red line indicates a linear fit through zero of the integer gate periods, yielding a lever arm $\frac{\partial A_I}{\partial V_{gate}} = 1.78 \times 10^{-13} m^2 V^{-1}$. The blue dashed line indicates a line with 3× larger slope, which would correspond to a quasiparticle charge $e^* = e/3$. The gate period at $\nu_{bulk} = 1/3$ falls close to the blue line, consistent with fractional charge $e^* = e/3$, whereas the period at $\nu_{bulk} = 2/3$ is close to the red line, suggesting integral interfering charge. The integer gate periods used are for the $N = 0$ LL; for $\nu_{bulk} \geq 2$ the periods for the spin-down edge state are used to avoid influence of the period-halving phenomenon discussed in the text. (b) Magnetic field periods ΔB at different quantum Hall states. The red dashed line represents the average integer period of 5.7mT, while the blue dashed lines three times the average integer period, which would be expected for the $\nu = 1/3$ state assuming constant area in both regimes.

$(B = 13T)$, we observe conductance oscillations as a function of gate voltage and magnetic field similar to those at integer states; the oscillations have gate voltage period

$\Delta V_{gate} = 6.1$mV; this yields an interfering quasiparticle charge $e^* = e\frac{\Phi_0}{B\Delta V_{gate}\frac{\partial A_I}{\partial V_{gate}}} = 0.29e$, in good agreement with the theoretical predictions. This supports previous experimental results utilizing shot noise [72], resonant tunneling [41], and Coulomb blockade [67]. We mention that interference at $\nu_{bulk} = 1/3$ was found to be reproducible using a range of different gate voltages as well as after thermal cycling the device to room temperature.

Next we discuss the $\nu = 2/3$ FQHE state, which is the hole-conjugate state to $\nu = 1/3$ [73]. Several edge structures have been proposed for the $\nu = 2/3$ state. Motivated by a picture in which the $\nu = 2/3$ consists of a $\nu = 1/3$ hole state imposed upon a $\nu = 1$ background, MacDonald proposed that the $\nu = 2/3$ edge should consist of an inner edge mode of charge $e^* = -e/3$ and an outer edge with $e^* = e$ [74]. Chang [75] and Beenakker [76] constructed models consisting of two $e^* = e/3$ edge modes; a later work indicated that a transition from the MacDonald edge structure to the Chang-Beenakker edge structure should occur as the confining potential is tuned from sharp confinement to soft confinement [77]. Yet another edge model was proposed by Kane, Fisher, and Polchinski in which the presence of disorder leads to a single $e^* = 2e/3$ charged edge mode and a counterpropogating neutral mode [78].

We measure conductance oscillations at $\nu = 2/3$ ($B = 6.8$T) with $\Delta V_{gate} = 3.7$mV, yielding a quasiparticle charge $e^* = e\frac{\Phi_0}{B\Delta V_{gate}\frac{\partial A_I}{\partial V_{gate}}} = 0.93e$, which suggests interference of an integrally charged edge mode. These oscillations have notably lower amplitude than those at both integer states and at $\nu = 1/3$. Presence of an integrally charged mode suggests that the Macdonald edge structure holds in our device. However, we do not find evidence for interference of a fractionally charged $e^* = -e/3$ mode at $\nu = 2/3$, even if the QPC bias is tuned to reduce backscattering. A possible explanation for this is that $e^* = -e/3$ should have a significantly smaller velocity due to being an inner mode; therefore, it will have lower phase coherence, making it very difficult to observe. Smaller device size or lower experimental temperatures might make measurement of the $-e/3$ mode possible.

It is noteworthy that our observation of an integrally charged mode differs from previous experimental findings, in which shot noise and Coulomb blockade measurements suggested a different edge structure consisting of two $e^* = e/3$ charge modes and two neutral modes [79,80], with no integrally charged mode observed. A possible explanation for this discrepancy is that our sample may have a sharper confining potential due to the short setback of the screening wells, resulting in our device supporting the edge structure described in Ref. [74]. Our work provides evidence that experimental details such as the confining potential affect which of the candidate edge structures is formed at $\nu = 2/3$. We mention that a sharp confining potential may also be beneficial for measuring interference at the $\nu = 1/3$ state by preventing edge reconstruction and the proliferation of neutral edge modes [81–83] which may cause dephasing [84,85]; neutral modes have been detected at $\nu = 1/3$ and numerous other fractional quantum Hall states in standard GaAs structures without screening wells [86].

2.7 Magnetic field oscillation periods

The magnetic field oscillation periods for integer fillings $\nu = 1$, 2, 3, and 4 as well as $\nu = 2/3$ and $\nu = 1/3$ are shown in Fig. 2.9b. The Aharonov-Bohm phase is predicted by equation (1), reproduced here: $\theta = 2\pi \frac{e^*}{e} \frac{A_I B}{\Phi_0}$. If the area of the interferometer A_I does not vary with filling factor, then this would yield a magnetic field period ΔB that is constant for all integer states, and inversely proportional to e^* for fractional states. We observe that ΔB is indeed nearly constant (approximately 5.7 mT) for integer states (with the exception of the period-halving phenomenon discussed previously, which has been omitted from Fig. 2.9); this average value is indicated by the red dashed line in the figure. ΔB at 2/3 is very close to the integer period, consistent with the gate voltage oscillation period which also implied interference of an integer charge. The magnetic field period at $\nu = 1/3$ is 22.2mT, much larger than the integer period. Under the assumption that the fractional mode

has the same interfering area as the integer modes, the e^* can be calculated from equation (1) as $e^*/e = \Delta B_{integer}/\Delta B_{1/3} \approx 0.26$. This is in reasonable agreement with the theoretical value $e^* = e/3$, although the moderate discrepancy suggests that the assumption of constant area may be somewhat inaccurate (the dashed blue line in Fig. 2.9b shows the predicted ΔB for constant area and $e^* = e/3$).

If the true interfering charge is assumed to be exactly $e/3$, the 22.2mT period gives an area of $3\Phi_0/\Delta B \approx 0.56\mu\text{m}^2$, about 23% smaller than the area for integer modes. Experiments of resonant tunneling in similarly sized mesoscopic devices have found similarly smaller areas for fractional edge modes compared to integer modes [42, 67].

Finally, we remark that although we have observed Aharonov-Bohm interference of fractionally charged quasiparticles at the $\nu = 1/3$ fractional quantum Hall state, we have not observed the fractional braiding statistics predicted for these quasiparticles [29, 37]. It has been suggested that increasing the flux through the interferometer by one flux quantum should result in the addition of one quasiparticle into the area of the device in order to keep the system charge neutral; this should result in an interference phase jump $\Delta\theta_{anyon} = 4\pi/3$ at the $\nu = 1/3$ state [36, 38]. We appear to measure only the Aharonov-Bohm phase when magnetic field is varied, suggesting that adding flux does not introduce quasiparticles in our device. Critically, the $\nu = 1/3$ state has a large energy gap for the creation of quasiparticles measured to be $\sim 700\mu$eV in a 2DES of similar density [87]. This energy is more than an order of magnitude larger than the measured charging energy in our device ($\frac{e^2}{2C} \sim 17\mu$V), which suggests that when magnetic field is varied it may be energetically favorable for the primary quantum well to remain at fixed filling factor (without creating quasiparticles) rather than fixed sheet density, with the energy cost of the variations in quantum well density reduced by the screening wells. When the experiment is performed at fixed filling factor it is expected that only the Aharonov-Bohm phase of the quasiparticles will be observed when magnetic field and side gate voltage are varied [38, 39], consistent with our observations. An alternative method to introduce quasiparticles and measure

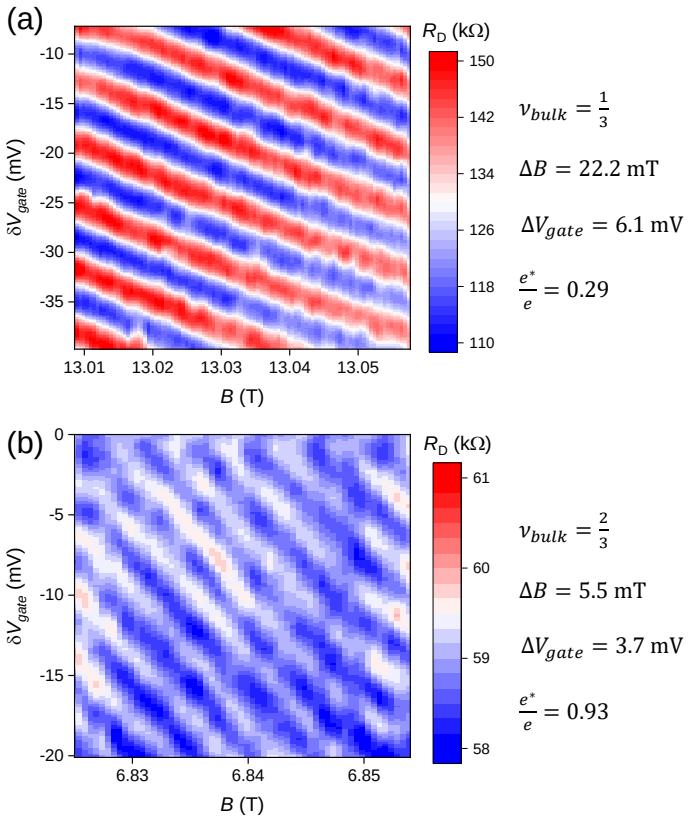

Fig. 2.10. **Interference of fractional quantum Hall states.** (a) Aharonov-Bohm conductance oscillations at $\nu = 1/3$. The QPCs are biased to approximately 22% reflection. (b) Aharonov-Bohm conductance oscillations at $\nu = 2/3$. The QPCs are biased to approximately 20% reflection. In both cases, δV_{gate} is relative to -1.4V.

braiding statistics would be to directly manipulate the electrostatic potential with a gate in the center of the interferometer [38, 39].

Methods

The primary quantum well was measured to have bulk electron density $n = 1.05 \times 10^{11}\text{cm}^{-2}$ and mobility $\mu = 7 \times 10^{6}\text{cm}^2\text{V}^{-1}\text{s}^{-1}$ measured after full device fabrication and in the dark.

The device was fabricated by: (1) optical lithography and wet etching to define the mesa; (2) deposition of In/Sn Ohmic contacts; (3) electron beam lithography and electron beam evaporation (10nm Ti/15nm Au) to define the interferometer gates; (4) optical lithography and electron beam evaporation (20nm Ti/150nm Au) to define the bondpads and the surface gates around the Ohmic contacts; (5) mechanical polishing to thin the GaAs substrate; (6) optical lithography and electron beam evaporation (200nm Ti/150nm Au) to define the backgates.

The device was measured in a dilution refrigerator with base mixing chamber temperature $T = 13$mK. Extensive heat sinking and filtering are used to achieve low electron temperatures and bring the electron temperature close to the cryostat temperature. Standard low-frequency ($f = 13$Hz) 4-terminal and 2-terminal lock-in amplifier techniques were used to probe the diagonal resistance and conductance across the device. Typically a 200pA excitation current was used for measurements of integer states and 100pA excitation was used when measuring fractional states. A +400mV bias cool was applied to the QPC and side gates while the device was cooled from room temperature; this bias-cool technique results in an approximately 400mV built-in bias on these gates, which improves device stability.

Acknowledgments

This work was supported by the Department of Energy, Office of Basic Energy Sciences, under Award number DE-SC0006671. Additional support for sample growth from the W. M. Keck Foundation and Nokia Bell Labs is gratefully acknowledged.

3. DIRECT OBSERVATION OF ANYONIC BRAIDING STATISTICS AT THE $\nu = 1/3$ FRACTIONAL QUANTUM HALL STATE

A version of this chapter has been submitted for publication.

3.1 Abstract

Utilizing an electronic Fabry-Perot interferometer in which Coulomb charging effects are suppressed, we report experimental observation of anyonic braiding statistics for the $\nu = 1/3$ fractional quantum Hall state. Strong Aharonov-Bohm interference of the $\nu = 1/3$ edge mode is punctuated by discrete phase slips consistent with an anyonic phase of $\theta_{anyon} = \frac{2\pi}{3}$. Our results are consistent with a recent theory of a Fabry-Perot interferometer operated in a regime in which device charging energy is small compared the energy of formation of charged quasiparticles [88]. Close correspondence between device operation and theoretical prediction substantiates our claim of observation of anyonic braiding.

3.2 Background

Quantum theory requires that all fundamental particles must be fermions or bosons, which has profound implications for particles' statistical behavior. However, theoretical works have shown that in two dimensions it is possible for particles to violate this principle and obey so-called anyonic statistics, in which exchange of particle position results in a quantum mechanical phase change that is not π or 2π (as for fermions or bosons), but a rational fraction of π [89, 90]. While anyons cannot exist

as fundamental particles in nature, certain condensed matter systems are predicted to host exotic quasiparticles which obey a certain form of anyonic statistics.

The quantum Hall effect is a remarkable example of a topological phase of matter occurring when a two-dimensional electron system (2DES) is cooled to low temperature and placed in a strong magnetic field. In the quantum Hall regime the bulk forms an insulator, and charge flows in edge currents which are topologically protected from backscattering and exhibit quantized conductance. The elementary excitations of fractional quantum Hall states [18] are not simply electrons, which obey fermionic statistics, but instead are emergent quasiparticles which are predicted to have highly exotic properties including fractional charge and anyonic statistics [21]. In two dimensions, two exchanges of particle positions are topologically equivalent to one quasiparticle encircling the other in a closed path [91], referred to as a braid; this is illustrated in Fig. 3.1a. The anyonic character of these quasiparticles is reflected in the fractional phase the system obtains from braiding; thus they are said to obey anyonic braiding statistics. The statistics of fractional quantum Hall states have been studied in theoretical [34,37] and numerical [29,92–95] works. The anyonic phase does not depend on the trajectory taken but only on the number of quasiparticles encircled, making braiding another manifestation of topology in quantum Hall physics; this topological robustness has motivated aggressive pursuit of fault-tolerant quantum computation based on braiding operations in various condensed matter systems [50, 91, 96, 97]. In a recent experimental work anyonic statistics were inferred from noise correlation measurements [98]; however, direct observation of the anyonic phase in braiding experiments will further our understanding of the exotic behavior of quantum Hall quasiparticles and is a necessary step to towards quasiparticle manipulation.

Electronic interferometry has been used to study edge physics in previous theoretical [36,38,40,54,84,88,99–101] and experimental [43–46,48,52,53,59–62,80,102–109] works, and has been proposed as an experimental means to observe anyonic braiding statistics [36,38,51,110] including the highly exotic non-Abelian form of anyonic

statistics [39, 70, 71, 111–115]. An electronic Fabry-Perot interferometer consists of a confined 2DES using quantum point contacts (QPCs) to partition edge currents, as shown in Fig. 3.1b. Quasiparticles backscattered by the QPCs will braid around quasiparticles localized inside the interferometer; therefore changes in N_{qp}, the number of quasiparticles localized inside the interferometer, will result in a shift in the interference phase due to the anyonic contribution θ_{anyon} [36, 38, 51, 110], with $\theta_{anyon} = \frac{2\pi}{2p+1}$ for a Laughlin fractional quantum Hall state $\nu = \frac{1}{2p+1}$ [34, 37]. The interferometer phase difference θ is a combination of the Aharonov-Bohm phase scaled by the quasiparticle charge e^* and the anyonic contribution, written in Eqn. 3.1 [36,38,110]:

$$\theta = 2\pi \frac{e^*}{e} \frac{A_I B}{\Phi_0} + N_{qp}\theta_{anyon} \tag{3.1}$$

The total current backscatterd by the interferometer will depend on $\cos(\theta)$, so interference phase can be probed by measuring the conductance G across the device [49].

A major obstacle towards the observation of anyonic phases through interferometry has been been the Coulomb interaction of the interfering edge state with charge located in the bulk of the interferometer [40]. A strong bulk-edge interaction causes the area A_I of the interferometer to change when charge in the bulk changes [36, 40]. As a consequence, for so-called Coulomb-dominated devices with strong bulk-edge interaction, the change in Aharonov-Bohm phase due to the change in A_I when N_{qp} is changed cancels out the anyonic phase θ_{anyon}, making quasiparticle braiding statistics unobservable [36]. While novel physics has been explored in Coulomb-dominated devices [42, 45–47, 67, 109], this bulk-edge interaction must be reduced to make anyonic braiding observable. Various techniques have been implemented to reduce this Coulomb bulk-edge interaction, including the use of metal screening gates [45, 46], low-temperature illumination to enhance screening by the doping layer [70, 71, 115], addition of an Ohmic contact inside the interferometer [48], and incorporation of auxilliary screening layers inside the semiconductor heterostructure [49]. The screening layer technique has enabled the use of small highly coherent interferometers that

exhibit robust Aharonov-Bohm interference, including at fractional quantum Hall states [49].

3.3 Device Design

The device used for these experiments utilizes a unique high-mobility GaAs/AlGaAs heterostructure [1,3] with screening layers to minimize the bulk-edge interaction (see the layer stack in Fig/ 3.2) [49]. The interferometer is defined using metal surface gates which are negatively biased to deplete the 2DES underneath. Two narrow constrictions define QPCs to backscatter edge currents, and wider side gates define the rest of the interference path. An SEM image of the device is shown in Fig. 3.1b; the device has a nominal area of 1.0μm $\times$ 1.0 μm, and measurements suggest that lateral depletion of the 2DES makes the interferometer area smaller by approximately 200nm on each side, similar to the experimental and numerical results in [49] (see also [55]). Note that the length scale of the interferometer is much greater than the magnetic length $l_B \equiv \sqrt{\frac{hc}{eB}}$ in the regime investigated, with l_B $\approx$9nm at $\nu = 1/3$, so the condition that the interfering quasiparticles be well separated from the localized quasiparticles inside the interferometer which they may braid around should hold [95, 116]. Compared to the device used in [49], the device used in this work has a lower electron density n, which improves device stability because smaller gate voltages can be used. The device also has a somewhat smaller area, which may increase coherence and visibility of interference. Experiments are performed in a dilution refrigerator with a base mixing chamber temperature of T$\approx$10mK; Coulomb blockade measurements of different quantum dot devices suggest a somewhat higher electron temperature of T $\approx$ 22mK. Negative voltages of $\approx$-1V are applied to the QPC gates and $\approx$-0.8V on the side gates; conductance is measured as a function of the side gate voltage variation δV_g, which is relative to -0.8V and applied to both side gates. An additional metal gate in the center of the device (not shown in Fig. 3.1b for clarity) is held at ground potential, so it does not affect the 2DES density; this gate is intended

to make the confining potential from the gates sharper. Measurements are performed using standard 4-terminal and 2-terminal lock-in amplifier techniques.

3.4 Discrete Phase Slips

We operated the device at high magnetic field B at the filling factor $\nu = 1/3$ quantum Hall state. In Fig. 3.3 we show the conductance variation δG measured across the interferometer versus B and δV_g near the center of the $\nu = 1/3$ conductance plateau. The QPCs remain in the regime of weak backscattering across this region region with approximately 90% transmission, and a smooth background conductance is subtracted so that the interference oscillations can be seen clearly. As can be seen in the figure, the predominant behavior observed is conductance oscillations with negatively-sloped lines of constant phase; however, quite conspicuously there are also a small number of discrete phase jumps in the data; dotted lines are guides to the eye for these features. The jumps in phase were found to be repeatable in subsequent scans; see Fig. 3.4.

Eqn. 3.1 provides a straightforward explanation for our observations. The continuous phase evolution with negatively-sloped lines of constant phase can be associated with the Aharonov-Bohm phase accumulated by the interfering quasiparticles, the first term in Eqn. 3.1, which has been observed in previous experiments in the integer [43, 45, 46] and fractional [49] quantum Hall regimes. The second term in Eqn. 3.1 predicts a discrete change in phase when the number of localized quasiparticles changes; therefore, it is natural to associate the discrete phase jumps with the anyonic phase contribution θ_{anyon}. It is noteworthy that the discrete jumps in phase occur across lines with positive slope in the B-V_g plane. This can be understood from the fact that increasing B is expected to remove quasiparticles from the bulk (or create quasiholes) [21, 38], while increasing gate voltage would make it electrostatically favorable to increase the number of localized quasiparticles. Thus, the magnetic field at which it becomes favorable to remove a quasiparticle should increase when gate

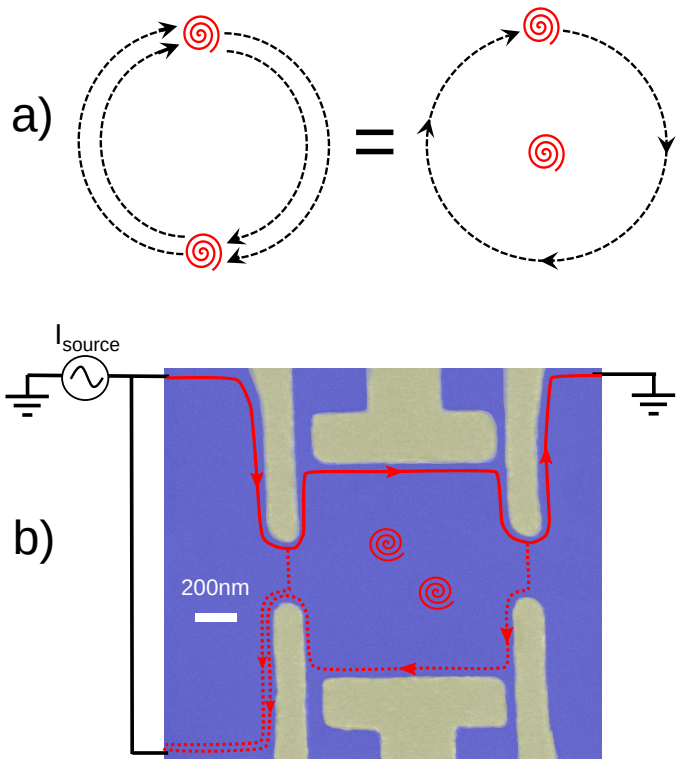

Fig. 3.1. **Quasiparticle braiding experiment.** a) Schematic representation of quasiparticle exchange; quasiparticles are represented by red vortices, and trajectories are shown in dashed lines. Two quasiparticle exchanges (left) which bring the particles back to their original position are topologically equivalent to one quasiparticle executing a closed loop around the the other, and in each case the system gains a quantum mechanical phase θ_{anyon} due to the quasiparticle's anyonic braiding statistics. b) False-color SEM image of interferometer. Blue regions indicate the GaAs where the 2DES resides, and metal gates under which the 2DES is depleted are highlighted in yellow. Red arrows indicate the edge currents, and dotted arrows indicate the backscattered paths which may interfere. Quasiparticles may be localized inside the chamber of the interferometer, as represented by the red vortices, and the backscattered paths enclose a loop around these quasiparticles, making the interferometer sensitive to θ_{anyon}. The lithographic area is 1.0μm $\times$ 1.0μm. The device used in the experiments also has a metal gate covering the top of the interferometer not shown in b), which is kept at ground potential and does not affect the 2DES density underneath.

Fig. 3.2. **Layer stack of the GaAs/AlGaAs heterostructure used for the experiments.** This structure utilizes three GaAs quantum wells: a primary 30nm well flanked by two 13nm screening wells to reduce the bulk-edge interaction in the interferometer. There are 25nm AlGaAs barriers between the main well and screening wells, and the total center-to-center setback of the screening wells from the main well is 48nm.

voltage is increased, and a positive slope to the quasiparticle transitions is expected, as observed in resonant tunneling experiments [42, 47, 67, 80, 117]. The fact that we do indeed observe a positive slope strongly suggests that these discrete phase jumps are associated with changes in localized quasiparticle number, and the magnitude of the slope is also consistent with this. Furthermore, a central principle of quantum Hall theory is that quasiparticles are localized in the hills and valleys of the disorder potential [118], and the fact that the discrete phase jumps are irregularly spaced indicates that their positions are in fact determined by disorder as expected.

To determine the value of the change in phase associated with each phase jump in the data, we performed a least-squares fit in the regions between the phase jumps, fitting the conductance data to the form $\delta G = \delta G_0 cos(2\pi \frac{1}{3} \frac{A_I B}{\Phi_0} + \theta_0)$, with the fitting

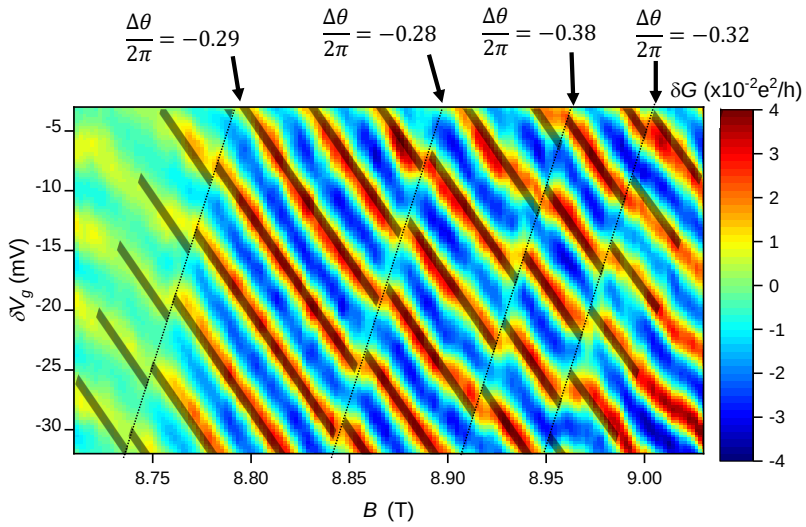

Fig. 3.3. **Conductance oscillations versus B and δVg in the central region.** The predominant behavior is negatively sloped Aharonov-Bohm interference, but a small number of discrete phase jumps are visible. Dashed lines are guides to the eye for these features. Least-squares fits of $\delta G = \delta G_0 \cos\left(2\pi \frac{AB}{\Phi_0} + \theta_0\right)$ are shown with highlighted stripes, and the extracted change in phase $\frac{\Delta\theta}{2\pi}$ are indicated for each discrete jump. Increasing magnetic field is expected to reduce the number of localized quasiparticles; therefore the change in phase across each jump is predicted to be $-\theta_{anyon}$.

parameter being θ_0. This expression for the conductance assumes that between the discrete phase jumps, the phase evolves only by the change in Aharonov-Bohm phase with changing B and changing A_I (via the change in V_g), and θ_0 is the excess phase which cannot be attributed to the Aharonov-Bohm effect. We determine the value of the phase jump by computing $\Delta\theta$, the difference in the fitted values of θ_0 in adjacent regions. The fitted data are shown highlighted in Fig. 3.3, and the extracted values of $\frac{\Delta\theta}{2\pi}$ are shown above each jump. Taking an average and assuming that each phase jump corresponds to the removal of a quasiparticle (or equivalently addition of a quasihole), we obtain $\theta_{anyon} = 2\pi \times (0.31 \pm 0.04)$; this is consistent with the theoretical value of $\theta_{anyon} = \frac{2\pi}{3}$ for the $\nu = 1/3$ state [34, 37]. Our work thus provides experimental

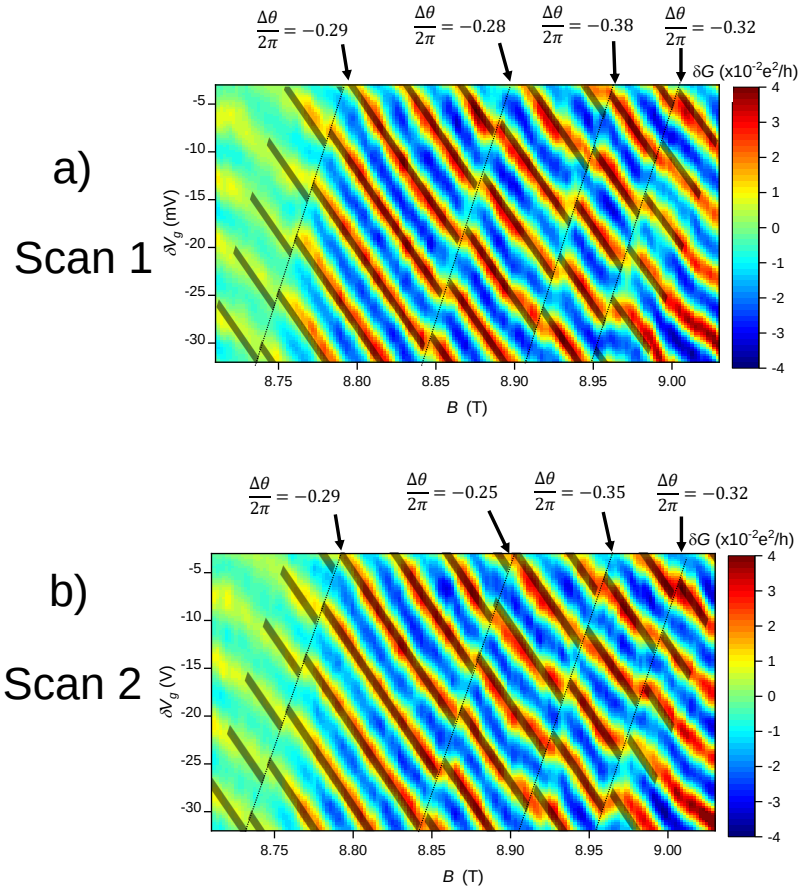

Fig. 3.4. **Repeatability of discrete phase jumps.** a)First scan measurement of conductance versus B and δV_g. This is the same data in Fig. 3.3. b) Second scan across the same range of magnetic field using the same QPC gate voltages. As can be seen from the data, the same pattern of discrete jumps appear in the second scan. The second scan was taken approximately one hour after the first scan. Values of $\frac{\Delta\theta}{2\pi}$ extracted from least squares fits are shown for both scans, and show similar values for each phase jump in both scans.

confirmation for the prediction of fractional braiding statistics at the $\nu = 1/3$ quantum Hall state.

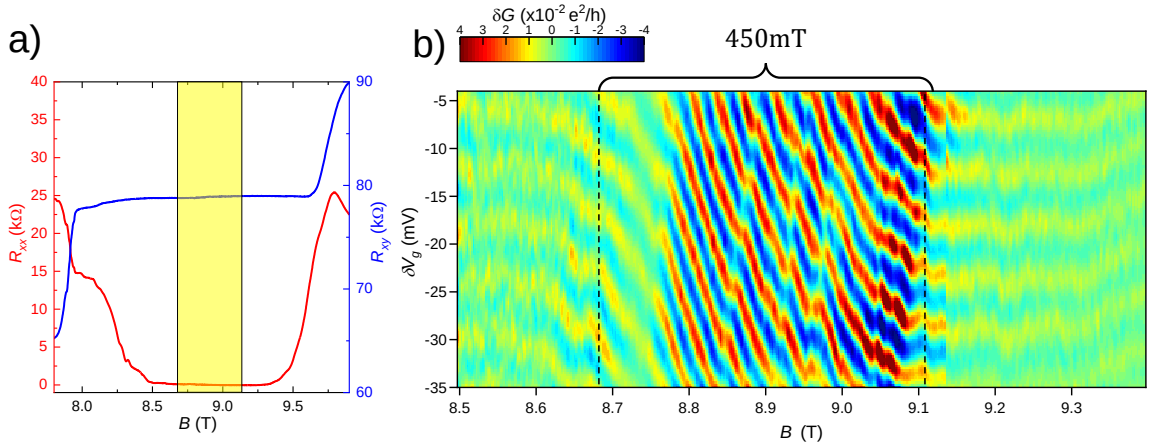

Fig. 3.5. **Interference across the $\nu = 1/3$ quantum Hall plateau.** a) Bulk magnetransport showing longitudinal resistance R_{xx} and Hall resistance R_{xy} across the $\nu = 1/3$ state. b) Conductance oscillations δG versus magnetic field B and side gate voltage δV_g (this side gate voltage variation is relative to -0.8V). The dashed lines indicate the approximate range over which the device appears to exhibit conventional Aharonov-Bohm interference with minimal influence of the anyonic phase contribution. The region over which this occurs is near the center of the plateau, and is highlighted in the bulk transport data in a).

3.5 Transition from constant filling to constant density

A recent theoretical work analyzed the case of a Fabry-Perot interferometer operated at the $\nu = 1/3$ state in which strong screening is utilized to reduce the characteristic Coulomb charging energy and thus suppress the bulk-edge interaction [88]. A key prediction is that the device will transition from constant filling factor to constant density when the magnetic field is varied away from the center of the state. The authors find that over a wide range of magnetic field the bulk 2DES stays at fixed $\nu = 1/3$ filling. In this regime of constant ν the predominant contributor to the phase will be the Aharonov-Bohm phase, but a small number of well-separated quasiparticle transitions should occur from which θ_{anyon} may be extracted, consistent with

our results described above. Once the magnetic field is varied away from the center, the authors predict that the electrostatic energy cost of varying density to maintain fixed ν will cause a transition from constant filling factor to constant density. In the regimes of constant density, many quasiparticles (at low field) or quasiholes (at high magnetic field) will be created inside the interferometer to keep the total charge fixed, with one quasiparticle or quasihole created when the flux is changed by one flux quantum Φ_0, resulting in significant changes in interference behavior mediated by the anyonic phase.

Motivated by these predictions, we operated the interferometer in a wide range of magnetic field across the $\nu = 1/3$ fractional quantum Hall state. Bulk magnetotransport at $\nu = 1/3$ with vanishing longitudinal resistance R_{xx} and a quantized plateau in the Hall resistance R_{xy} is shown in Fig. 3.5a, showing the range of magnetic field over which the $\nu = 1/3$ state occurs in our sample. The conductance measured across the device across the $\nu = 1/3$ state is shown in Fig. 3.5b; this is the same measurement as shown in Fig. 3.3, but extended to higher and lower magnetic field. As discussed previously, near the center of the $\nu = 1/3$ plateau the predominantly observed behavior in the conductance is lines of constant phase with negative slope consistent with Aharonov-Bohm interference [36, 38, 40, 49] with a small number of discrete jumps attributed to quasiparticle transitions. The gate voltage and magnetic field oscillation periods are approximately three times larger than the integer periods measured at $\nu = 1$, consistent with interference of e/3 fractionally charged quasiparticles, as is expected for the $\nu = 1/3$ state and consistent with previous experimental observations of fractional charge [41, 45, 49, 72, 119]. On either side of this central region, however, the behavior changes significantly. The lines of constant phase lose their negative slope; although there is still weak magnetic field dependence to the pattern, the magnetic field scale over which the phase varies is much larger than in the central region, making the lines of constant phase nearly flat; the oscillations depend primarily only on the side gate voltage. It is noteworthy that, despite this conspicuous change, the lines of constant phase are continuous across the transition from the

central Aharonov-Bohm region to the upper and lower regions, which indicates that the oscillations are still due to interference of the edge state.

Our experimental observation that negatively-sloped Aharonov-Bohm interference occurs only in a finite range of magnetic field agrees with the predictions of [88]. At first blush the behavior observed above and below this central region seems to conflict with predictions: we observe an interference pattern that becomes nearly independent of magnetic field, while [88] predicts that the magnetic field period will decrease from $3\Phi_0$ in the central region to Φ_0 in the upper and lower regions because quasiparticles will be created with period Φ_0. However, an additional key prediction in [88] is that the Φ_0 oscillations will be extremely susceptible to thermal smearing, with the authors estimating a temperature scale $T_0 \approx 2$mK (because our device is smaller than the one considered in [88] this predicted temperature scale would be $T_0 \approx 4$mK for our device, still much smaller than our estimated electron temperature of 22mK). This thermal smearing can be understood from the fact that the regime of constant density corresponds to the chemical potential being at a position of high density of states (DOS), and thus small energy spacing between states, leading to thermal smearing. Therefore, the absence of Φ_0 oscillations at T$\approx$ 22mK is in fact in agreement with [88].

The fact that the lines of constant phase flatten out and become independent of magnetic field can be understood based on the combined contribution of the Aharonov-Bohm phase and anyonic phase (Eqn. 3.1). For the $\nu = 1/3$ state, quasiparticles are predicted to carry fractional charge $e^* = e/3$ and fractional braiding statistics $\theta_{anyon} = 2\pi/3$ [34]. Changing the magnetic field to add one flux quantum to the device will change the Aharonov-Bohm phase by $\frac{2\pi}{3}$. Additionally, in the lower field regimes one quasiparticle will be removed, and in the high field regime one quasihole will be added, resulting in a phase shift of $-\frac{2\pi}{3}$ and leaving the total interference phase unchanged in both regimes. The Aharonov-Bohm phase varies continuously, while (in the limit of zero temperature) the quasiparticle number will change discretely, leading to the predicted Φ_0 oscillations [38, 88]; however, when the

quasiparticle number is thermally smeared, the average number of localized quasiparticles will vary nearly continuously, leading to a smooth variation of the anyonic phase; in this case the smoothly varying thermally-averaged anyonic phase cancels the Aharonov-Bohm phase, leading to no change in θ as B is varied, consistent with our experimental observations. Because each quasiparticle at the 1/3 state is a vortex, this can also be understood based on the result from [34] that the Berry phase of a vortex encircling a closed path is equal to $2\pi\langle q_{enc}\rangle$ where q_{enc} is the charge enclosed in the path, and the high and low field regions the electrostatics force density to remain fixed, and thus $\langle q_{enc}\rangle$ remains nearly constant.

The approximate range over which the negatively-sloped Aharonov-Bohm oscillations occur is marked with dashed lines in Fig. 3.5a, and has a span of approximately 450mT. To make a quantitative comparison to theory, we compute the predicted width of the fixed ν region from [88]: $\Delta B_{constant-\nu} = \frac{\Delta_{1/3}\Phi_0 C_{SW}}{\nu e^2 e^*}$. In this expression $\Delta_{1/3}$ is the excitation gap of the $\nu = 1/3$ state which we measure to be ≈ 5.5K (see Fig. 3.6), consistent with previous measurements of the $\nu = 1/3$ gap [87]. C_{SW} is the capacitance per unit area of the screening layers to the quantum well which we calculate as $C_{SW} = \frac{2\epsilon}{d}$, with the factor of two accounting for the fact that there are two screening layers and $d = 48$nm the setback of the screening layers from the quantum well. Using the experimental values from the device gives a predicted value for $\Delta B_{fixed-\nu} \approx 530$mT, in good agreement with the experimentally observed range of Aharonov-Bohm interference of $\approx 450mT$, which suggests that the experimentally observed transition in interference behavior can indeed be explained by the model of [88].

The arguments in [88] of a transition from a regime of constant ν to regimes of constant n when moving away from the center of the state also apply to integer quantum Hall states. In Fig. 3.7 we show measurements of interference as a function of B and V_g across the integer state $\nu = 1$; in contrast to the fractional $\nu = 1/3$ case, the device exhibits no change in behavior and displays negatively-sloped Aharonov-Bohm interference at the high and low field extremes of the plateau. This is consistent

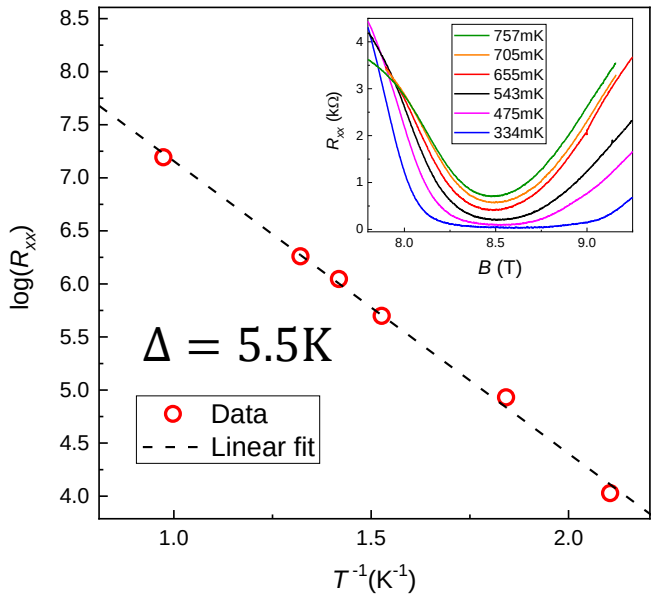

Fig. 3.6. **Measurement of the energy gap for the $\nu = 1/3$ fractional quantum Hall state.** The inset shows longitudinal resistance R_{xx} measured in a bulk region away from the interferometer at different temperatures. A linear fit of the data to the form $R_{xx} = R_0 e^{\frac{-\Delta}{2kT}}$ yields a gap of Δ =5.5K. This is consistent with values measured in previous experiments at similar magnetic field [87].

with the fact that the charge carriers and excited states are electrons which obey fermionic statistics, making their braiding unobservable; $\theta_{fermion} = 2\pi$.

3.6 Period Analysis

Additionally, there is a moderate change in the side gate voltage oscillation period in the high and low field regions compared to the central region; here we analyze this shift in period and find that it consistent with a weak coupling of the side gates to the bulk 2DES inside the interferometer.

We discuss the change in interference behavior from the central region, where the device exhibits primarily Aharonov-Bohm interference behavior with a few phase jumps, to the high and low field regions, where the lines of constant phase flatten out.

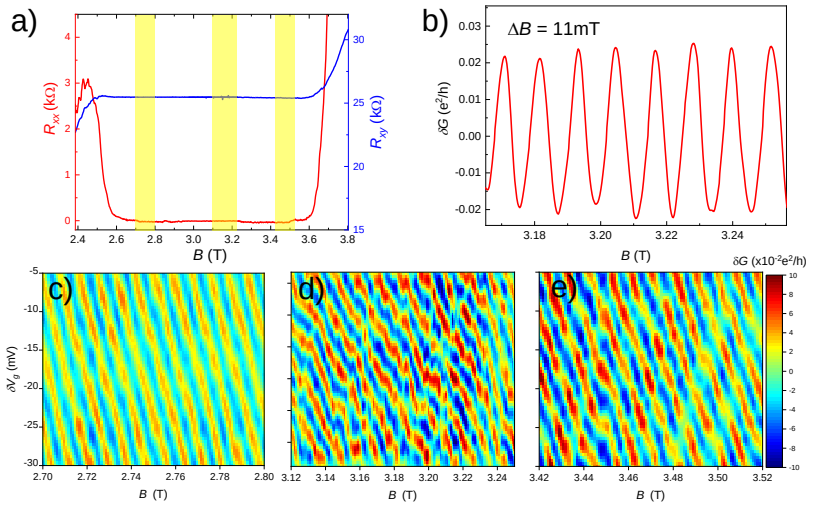

Fig. 3.7. **Measurements of interference at $\nu = 1$.** a) Bulk quantum Hall transport showing the zero in R_{xx} and plateau in R_{xy} corresponding to the $\nu = 1$ integer quantum Hall state. For this integer state, the bulk excitations and edge state current carrying particles are simply electrons, which obey fermionic statistics. b) Conductance oscillations versus magnetic field, showing an oscillation period ΔB =11mT. From this period the effective area A_I of the interferometer can be extracted: $A_I = \frac{\Phi_0}{\Delta B}$ In c), d), and e) we show conductance versus B and δV_g across the interferometer in the low field region of the plateau, near the center of the plateau, and on the high-field side of the plateau; the region on the plateau corresponding to each pajama plot is shown in a). In each of these regions the device exhibits negatively sloped Aharonov-Bohm oscillations. This contrasts with the data shown in Fig. 3.5 for the $\nu = 1/3$ state where lines of constant phase flatten out at high and low fields. This is consistent with the fact that electrons, which carry current and form localized states at $\nu = 1$, are fermions who obey trivial braiding statistics, $\theta_{fermion} = 2\pi$, making braiding unobservable and leading to no change in interference behavior.

Interestingly, despite the lines of constant phase remaining continuous, the side gate oscillation period becomes smaller in the high and low field regions relative to the central region, with periods of 5.8mV at 8.4T, 8.5mV at 8.85T, and 5.4mV at 9.3T. In Fig. 3.8a line cuts of conductance versus gate voltage are shown at these magnetic fields illustrating the change in period. On the other hand, the model of [88] suggests

that the side gate oscillation period will be the same in the central region as in the upper and lower field regions, because the authors assume that the side gate couples only to the edge of the interferometer; under this assumption the side gate voltage will only affect the Aharonov-Bohm phase, making the variation of θ with V_g the same in each region. However, in a real device the gates do not affect just area; they also have some effect on the charge in the bulk of the interferometer. In the high and low field regions this will lead to an additional change in phase with gate voltage due to changes in localized quasiparticle number. To analyze the effect this will have on the side gate oscillation period, in Eqn. 3.2 we take the derivative of θ (from Eqn. 3.1) with respect to side gate voltage:

$$\frac{\partial\theta}{\partial V_g} = 2\pi\frac{e^*}{e}\frac{B}{\Phi_0}\frac{\partial A_I}{\partial V_g} + \theta_a\frac{\partial\langle N_L\rangle}{\partial V_g} \tag{3.2}$$

Here with $\langle N_L\rangle$ we take the thermally averaged number of quasiparticles to account for the fact that in the high and low field regimes significant thermal smearing is expected, and $\langle N_L\rangle$ will not necesarily be an integer [88].

In order to determine whether change in localized quasiparticle number with gate voltage can explain the observed change in period, we determine the parameter $\alpha_{bulk} \equiv \frac{\partial q_{bulk}}{\partial V_g}$ which paramaterizes how the bulk charge inside the interferometer q_{bulk} changes with V_g. To determine α_{bulk} we have operated the device at zero magnetic field in the Coulomb blockade regime [57] with the QPCs tuned to weak tunneling; in this regime there is one conductance peak each time the number of electrons in the device changes by one. Inverting the Coulomb blockade oscillation period gives the total lever arm coupling the side gates to the interferometer, $\alpha_{total} = \frac{1}{\Delta V_{CB}} = \frac{\partial q_{total}}{\partial V_g}$. Zero-field Coulomb blockade oscillations are plotted in 3.8b; the 5.4mV period yields α_{total} =0.19mV^{-1}. However, q_{total} is a combination of charge at the edge and charge in the bulk, $q_{total} = q_{edge} + q_{bulk}$, so to determine α_{bulk} we must also determine $\alpha_{edge} \equiv \frac{\partial q_{edge}}{\partial V_g}$. To extract α_{edge} we operate the device as an Aharonov-Bohm interferometer at the integer quantum Hall state $\nu = 1$; in this regime the interference phase and thus the oscillation period depends only on change in interference area and not on changes

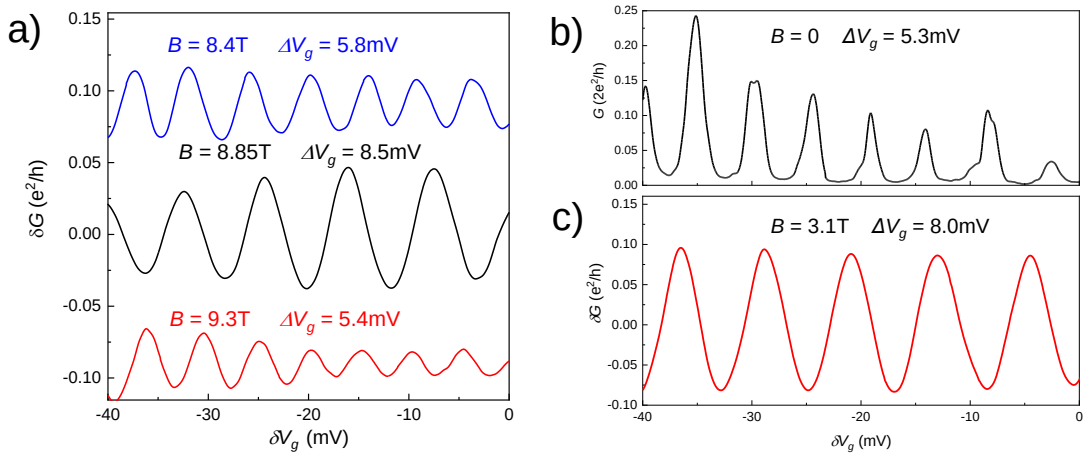

Fig. 3.8. **Conductance oscillations at different magnetic fields.** a) Conductance oscillations δG versus side gate voltage δV_g in the low-field region at $B = 8.4$T (blue), in the central region at $B = 8.85$T (black), and in the high-field region at $B = 9.3$T (red). The side gate oscillation period $\Delta V_{sidegates}$ is significantly smaller in the low field and high field regions than in the central region, with $\Delta V_g = 5.8$mV at 8.4T, $\Delta V_g = 8.5$mV at 8.85T, and $\Delta V_g = 5.4$mV at 9.3T. The QPCs are tuned to approximately 90% transmission. b) Conductance G versus side gate voltage at zero magnetic field with the device operated in the Coulomb blockade regime. Unlike other data presented in this work, the oscillations shown here are due to resonant tunneling of electrons rather than interference, and the QPCs are tuned weak tunneling, $G << \frac{e^2}{h}$. The Coulomb blockade oscillations have a period of 5.3mV, which is used to obtain the total lever arm α_{total} of the gates to the interferometer. c) Aharonov-Bohm interference oscillations at $\nu = 1$. The oscillations period of 8.0mV is used to obtain the lever arm α_{edge} of the gates to the edge.

in charges localized in the bulk [36]. Since for an integer state each oscillation period corresponds to changing the enclosed flux by one, $\alpha_{edge} = n\frac{\partial A_I}{\partial V_g} = \frac{n\Phi_0}{B}\frac{1}{\Delta V_{\nu=1}}$ with n the electron density (we assume that the electrostatics which determine the coupling of the gate to the edge and to the bulk do not change significantly with magnetic field). AB interference oscillations for the integer state $\nu = 1$ at B = 3.1T are show in Fig. 3.8c; the period of 8.0 mV gives $\frac{\partial A}{\partial V_g} = 0.167\mu\text{m}^2\text{V}^{-1}$ and $\alpha_{edge} = 0.12\text{mV}^{-1}$. Finally,

we calculate $\alpha_{bulk} = \alpha_{total} - \alpha_{edge}$ =0.19mV^{-1}−0.12mV^{-1} =0.07mV^{-1}. The fact that α_{edge} is significantly larger than α_{bulk} indicates that, as expected, the primary action of the side gates is to change the area of the interferometer, and the change in bulk charge is comparatively small.

We calculate the expected periods in each regime at $\nu = 1/3$ by $\Delta V_g = 2\pi(\frac{\partial\theta}{\partial V_g})^{-1}$. In the central region quasiparticles are unlikely to be created because the energy gap, so only the first term on the right-hand side of Eqn. 3.2 contributes, whereas in the low-field/high-field regions quasiparticles/quasiholes will be created and contribute to the phase, so both terms will contribute. For the central region then the predicted period is $\Delta V_g = \frac{\Phi_0}{B}\frac{e}{e^*}(\frac{\partial A_I}{\partial V_g})^{-1} \approx 8.4$mV, in good agreement with the measured value of 8.5mV. This agreement with the model suggests that interference in the central region can indeed be understood as the Aharononv-Bohm effect at constant ν of $e/3$ quasiparticles, consistent with theoretical predictions of fractional charge [21] as well as previous experiments in interferometry [45,49] and other experimental observations of fractional charge [41,72,119]. At 8.4T and 9.3T, taking into account the creation of quasiparticles, we calculate $\Delta V_g = \frac{1}{\frac{B}{\Phi_0}\frac{e^*}{e}\frac{\partial A_I}{\partial V_g}+\frac{\theta_a}{2\pi}\frac{\partial N_L}{\partial V_g}} = \frac{1}{\frac{B}{3\Phi_0}\frac{\partial A_I}{\partial V_g}+\alpha_{bulk}}$; here we have used $\frac{e^*}{e} = \frac{1}{3}$, $\theta_a = \frac{2\pi}{3}$, and $\frac{\partial N_L}{\partial V_g} = \frac{e}{e^*}\alpha_{bulk}$. This equation yields a predicted δV_g of ≈ 5.5mV at 8.4T and ≈ 5.1mV at 9.3T, in good agreement with the experimental values of 5.8mV and 5.4mV. This agreement between predicted and observed oscillation periods in each region is strong support for the picture in [88] of a region of constant n and a quasiparticle population at low field, a region of constant ν near the center of the state, and a region of constant n and a quasihole population at high field.

Additionally, these extracted lever arms can be used analyze quantitatively the slope of the quasiparticle transition lines in Fig. 3.3. These transitions will occur when it becomes energetically favorable for a quasiparticle to be created at a certain place in the device, therefore the transition lines will correspond to lines of constant electrostatic energy associated with charge on the device. This electrostatic energy comes from accumulating charge on the device due to changes in the condensate charge density with magnetic field, which may be compensated for by the creation

of quasiparticles. The charge on the 2DES is thus a combination of the condensate charge density and the charge associated with each localized quasiparticle:

$$q_{2DES} = \frac{e\nu A_I B}{\Phi_0} + e^* N_{qp} \tag{3.3}$$

Furthermore, we must consider the net charge, q_{net}, the difference between the charge in the 2DES (from Eqn. 3.3) and the background charge:

$$q_{net} = q_{2DES} - q_{back} = \frac{e\nu AB}{\Phi_0} + e^* N_{qp} - q_{donor} - e\alpha_{bulk}\delta V_g \tag{3.4}$$

Here the background charge is a combination of the charge from the donors, q_{donor}, and the effect of the gate voltage. We follow [36] in treating the gates as creating some effective additional background charge $e\alpha_{bulk}\delta V_g$. Since the changes in localized quasiparticle number occur when the electrostatic energy cost exceeds the energy cost to create a quasiparticle, Eqn. 3.4 implies that the localized quasiparticle transitions will occur across lines with a slope $\frac{dV_g}{dB} = \frac{\nu A}{\Phi_0 \alpha_{bulk}}$. Using $\nu = 1/3$, $\alpha_{bulk} = 0.07\text{mV}^{-1}$ (discussed above), and area extracted from the AB oscillations at $\nu = 1$ $A = \frac{\Phi_0}{\Delta B_{\nu=1}} \approx 0.38\mu m^2$ (Fig. 3.7b), we obtain $\frac{dV_g}{dB} \approx 0.44\text{mV/mT}$. Experimentally, the observed phase jumps occur with a slope of approximately 0.5 mV/mT, in good agreement with the predicted value. This is strong evidence that the discrete phase jumps do indeed correspond to changes in the number of localized quasiparticles inside the interferometer.

3.7 Temperature dependence

An additional observation is that the oscillation amplitudes decay with temperature much more sharply in the high-field and low-field regions than in the central region. We measured the amplitude of the oscillations in each region versus temperature; the oscillations decay approximately exponentially with T as temperature increases, and we can characterize each region by the temperature decay scale T_0 assuming that the oscillation amplitude varies as $e^{\frac{-T}{T_0}}$ [38, 83, 112, 113]. We extract

T_0 through a linear fit of the natural log of the oscillation amplitude as a function of temperature; this data is shown in Fig. 3.9. For the low-field region at 8.4T (blue) $T_0 = 31$mK, for the central region at 8.85T (black) $T_0 = 94$mK, and for the high-field region at 9.3T (red) $T_0 = 32$mK. Interestingly, T_0 is nearly 3 times smaller in the high and low field regions compared to the central region, suggesting enhanced thermal dephasing in these regions. The fact that this increased dephasing occurs in the regions where a large number of quasiparticles and quasiholes populate the interferometer, but not in the central region, suggests that it may be explained by the topological dephasing proposed in [85], in which thermal fluctuations in localized quasiparticle number reduce interference visibility in Fabry-Perot interferometers. This affirms the expectation that the regimes of constant density correspond to high quasiparticle DOS [88]. This dephasing is a remarkable example of the non-local influence of anyonic statistics: despite the fact that the edge quasiparticles are well separated by many magnetic lengths from quasiparticles inside the bulk of the interferometer such that there is minimal direct interaction, thermal fluctuations in N_{qp} nevertheless lead to rapid thermal dephasing of the interference signal.

3.8 Velocity Measurements

We have discussed the observation that the temperature decay scale is much smaller in the high and low field regions than in the central region at $\nu = 1/3$, which suggests that topological dephasing due to thermal smearing of the localized quasiparticle number inside the interferometer may contribute in the high and low field regions. However, another possible explanation for the change in T_0 is that the edge velocity might be much larger at the center, and decrease in the high and low field regions; if this were the case, T_0 would decrease simply due to the additional thermal smearing of the edge state (that said, such a large and non-monotonic change in the velocity over such a relatively small range of B would be rather surprising). In order to determine if the change in T_0 can be explained by changes in the edge ve-

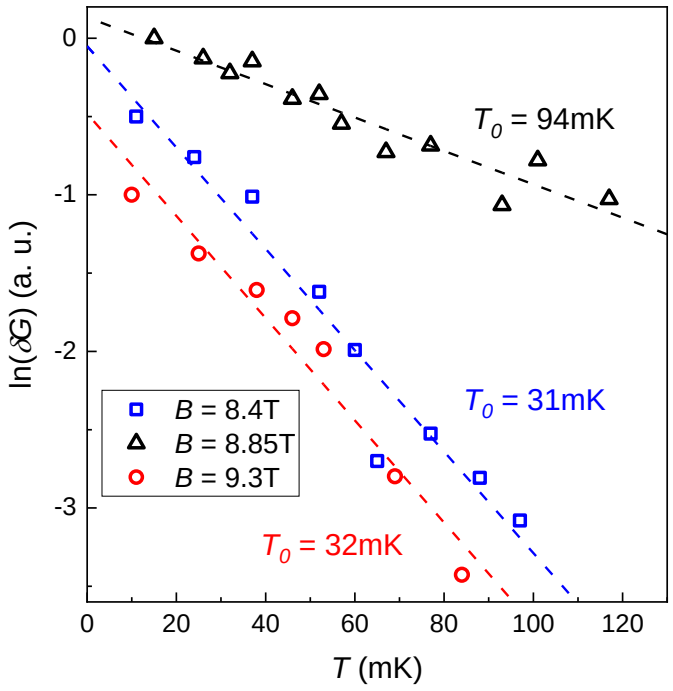

Fig. 3.9. **Dependence of oscillation amplitude on temperature.** The natural log of the oscillation amplitude δG at 8.4T, 8.85T, and 9.3T is plotted versus temperature. Data points are normalized to the amplitude at the lowest temperature and offset for clarity. The oscillation amplitudes show an approximately exponential decay with increasing temperature. Dashed lines indicate linear fits from which the temperature decay scale T_0 is extracted at each magnetic field. T_0 is much larger in the central region than in the low and high field regions, suggesting that there is an additional dephasing mechanism in these regions. This may be explained by topological dephasing due to thermal smearing of the quasiparticle number. The QPCs are tuned to approximately 90% transmission at each temperature to maintain constant backscattering.

locity v_{edge}, we have performed differential conductance measurements in each region from which v_{edge} can be extracted [38]; this has been performed previously for integer quantum Hall states in Aharonov-Bohm interferometers [44,49,60]. We consider first the case of an integer charge edge state. When a finite source drain voltage bias is applied, the energy of the injected edge electrons changes, and this leads to a shift in the phase from the edge dispersion, $\delta\theta = \delta\epsilon \frac{\partial k}{\partial \epsilon} L = \frac{\delta \epsilon L}{\hbar v_{edge}}$. This leads to an additional

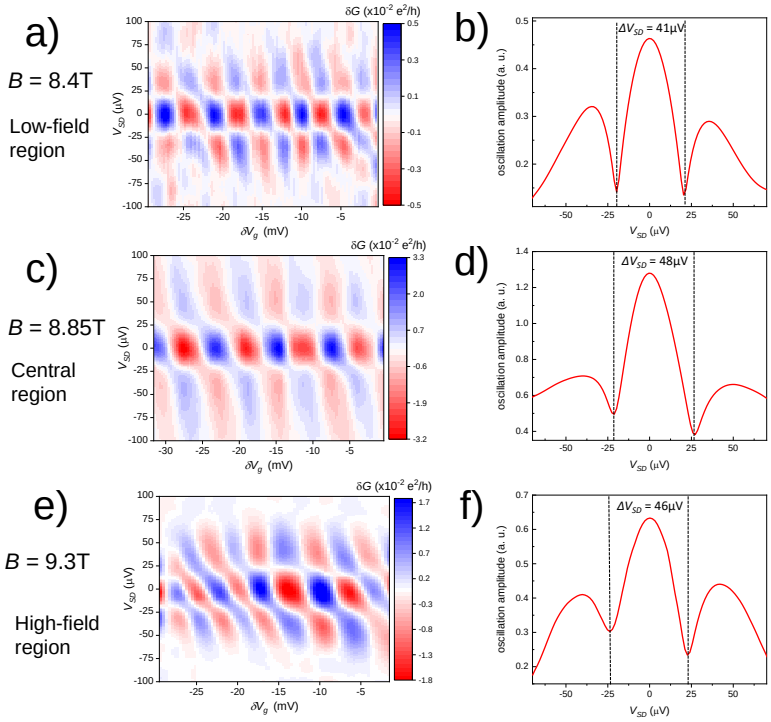

Fig. 3.10. **Differential conductance measurements at $\nu = 1/3$.** a) Differential conductance $\frac{\partial I}{\partial V_{sd}}$ as a function of side gate voltage δV_g and source-drain bias V_{sd} at $B = 8.4$T in the low-field region. b) Conductance oscillation amplitude from a FFT of the conductance versus side gate voltage data as a function of V_{sd}. The oscillation amplitude shows a node pattern as a function of V_{sd} from which the edge velocity may be extracted, yielding $v_{edge} = 8.3 \times 10^3$m/s. c) Differential conductance and d) oscillation amplitude versus V_{sd} at 8.85T giving $v_{edge} = 9.7 \times 10^3$m/s. e) Differential conductance and f) oscillation amplitude versus V_{sd} at 9.3T giving $v_{edge} = 9.3 \times 10^3$m/s. Evidently, the edge velocity does not change significantly across the $\nu = 1/3$ quantum Hall plateau.

interference pattern that occurs as a function of source-drain bias V_{sd} which can be observed in the differential conductance measurement, resulting in a checkerboard pattern in the measured differential conductance as a function of V_{sd} and δV_g. Thus nodes in the conductance oscillations which occur as a function of δV_g occur at certain values of V_{sd}, and the spacing between nodes can be used to extract the edge velocity [38, 44, 49, 102]:

$$v_{edge} = \frac{e^* L \Delta V_{sd}}{2\pi\hbar} \tag{3.5}$$

Here L is the perimeter of the interferometer, estimated based on the area extracted from Aharonov-Bohm interference measurents $L = 4\sqrt{A_I} \approx 2.5\mu$m. Differential conductance measurements are shown at $\nu = 1/3$ in Fig. 3.10. Also plotted is the oscillation amplitude (extracted from a Fourier transform of the data) versus V_{sd}, which enables convenient extract of ΔV_{sd} [44]. This is shown for the low-field region in a) and b), for the central region in c) and d), and for the high-field region in e) and f). Using Eqn. 3.5 yields edge velocities of 8.3×10^3m/s in the low-field region at $B = 8.4$T, 9.7×10^3m/s in the central region at $B = 8.85$T, and 9.3×10^3m/s in the low-field region at $B = 9.3$T The fact that the velocity does not change significantly with magnetic field indicates that a change in edge velocity cannot account for large change in temperature decay scale T_0 between regions. The expected T_0 can be calculated as $T_0 = \frac{h}{2\pi k_B \tau}\frac{1}{g}$ [38, 113] where g is the scaling exponent of the edge state, $g = \frac{1}{3}$ for $\nu = 1/3$ [38], and $\tau = \frac{L}{v_{edge}}$ is the time for the edge state to traverse the interferometer. This yields predicted T_0 based on thermal smearing of the edge state of 76mK at $B = 8.4$T, 89mK at 8.85T, and 85mK at 9.3T. The predicted value of 89mK in the central region at 8.85T is close to the experimentally observed T_0 of 94mK, indicating that the decay of amplitude in the region where the device is nearly free of quasiparticles can be attributed to thermal smearing of the edge. We have observed similar agreement between predicted and observed T_0 at the integer quantum Hall state $\nu = 1$ [49]. However, the experimentally observed T_0 of 31mK in the low-field region and 32mK in the high field region at $\nu = 1/3$ are much smaller than the values predicted for thermal smearing of the edge, indicating that another dephasing mechanism must be at play. This provides further support for the theory that topological dephasing due to thermally smearing of localized quasiparticles contributes to dephasing in these regions.

3.9 Additional Device

The behavior of the device described here were reproduced in a second device, including the change in interference behavior from negatively-sloped Aharonov-Bohm interference to flat lines of constant phase, the suppression of T_0 outside the central region, and the observation of discrete phase jumps consistent with the predicted anyonic phase at $\nu = 1/3$; see Fig. 3.11.

3.10 Possible Bulk-edge interaction effects

We discuss another possible explanation for some of the experimental observations. It is worth mentioning that there is another mechanism which can cause discrete changes in phase in quantum Hall interferometers, even for integer quantum Hall states. In devices which are intermediate between the Aharonov-Bohm and Coulomb-dominated regimes, creation of a localized charge inside the interferometer causes the area of the interferometer to change due to finite bulk-edge coupling, resulting in a reduction in the Aharonov-Bohm phase visible discrete changes in the interference phase. This mechanism does not depend on exotic braiding statistics [36]. However, increasing the magnetic field should tend to remove particle-like quasiparticles or create hole-like quasiparticles; in either case each excitation will lead to an an increase in phase when magnetic field is increased, because the decrease in N_{qp} would be accompanied by compensatory increase in A_I. However, this is inconsistent with our observation of negative changes in phase across each discrete phase jump, and also inconsistent with the fact that these discrete phase jumps occur in the region where the Aharonov-Bohm phase shows clear negative slope, indicating minimal bulk-edge interaction. Nevertheless it is possible that some residual bulk-edge interaction may have a small effect on the observed phase jumps. In [36] it was found that the observed jumps in phase when changing quasiparticle number should be $\Delta\theta = \theta_{anyon} \times (1 - \frac{K_{IL}}{K_I})$, where $\frac{K_{IL}}{K_I}$ is the ratio of the bulk-edge interaction strength K_I to the characteristic energy cost for charging the edge K_I. Thus, residual bulk-edge interaction would

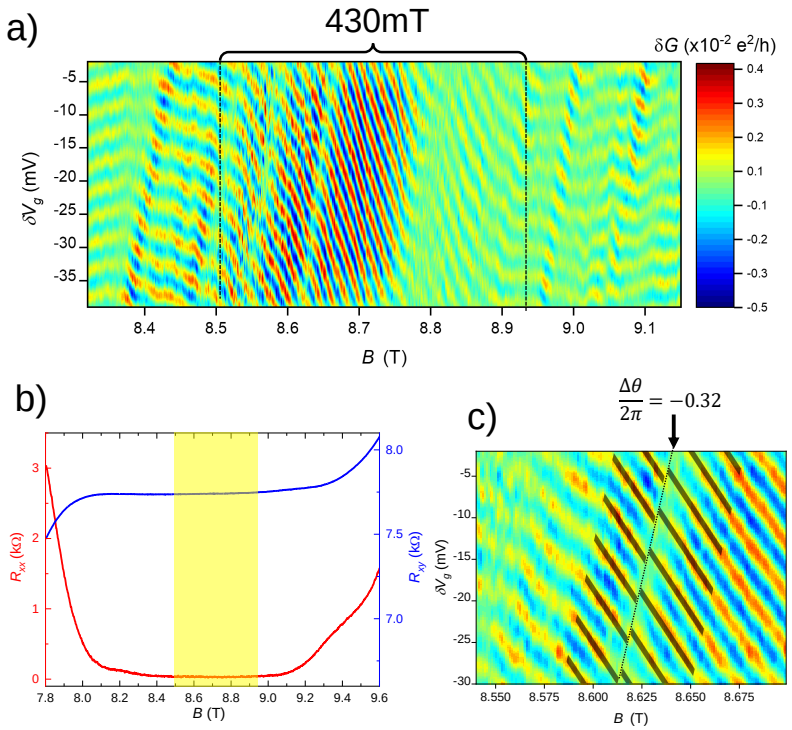

Fig. 3.11. **Measurements of interference for a second device, taken from a different chip fabricated on the same wafer.** a) Conductance across the interferometer versus magnetic field B and side gate voltage δV_g; δV_g is relative to -1.0V. Behavior is similar to that observed in the device described for the first device: in a finite region with width $\approx$ 430mT, the device exhibits negatively sloped Aharonov-Bohm oscillations, which flatten out at higher and lower magnetic fields, consistent with the creation of quasipaticles and quasiholes. b) Bulk magnetotransport showing R_{xx} (red) and R_{xy} (blue) for device B. The region near the center of the $\nu = 1/3$ state where the negatively sloped Aharonov-Bohm oscillations occur is highlighted. c) zoomed-in view of a clear phase jump in the data (this jump is also visible in b), but the data in c) is a different scan intended to improve signal to noise). Least-squares fits of the conductance on either side of the phase jump yields an extracted phase jump $\frac{\Delta\theta}{2\pi} = -0.32$, yielding an anyonic phase $\theta_{anyon} = 2\pi \times 0.32$, consistent with theory.

result in a slightly smaller observed change in phase. This might account for the fact that the majority of the observed phase jumps are slightly smaller than $\frac{2\pi}{3}$.

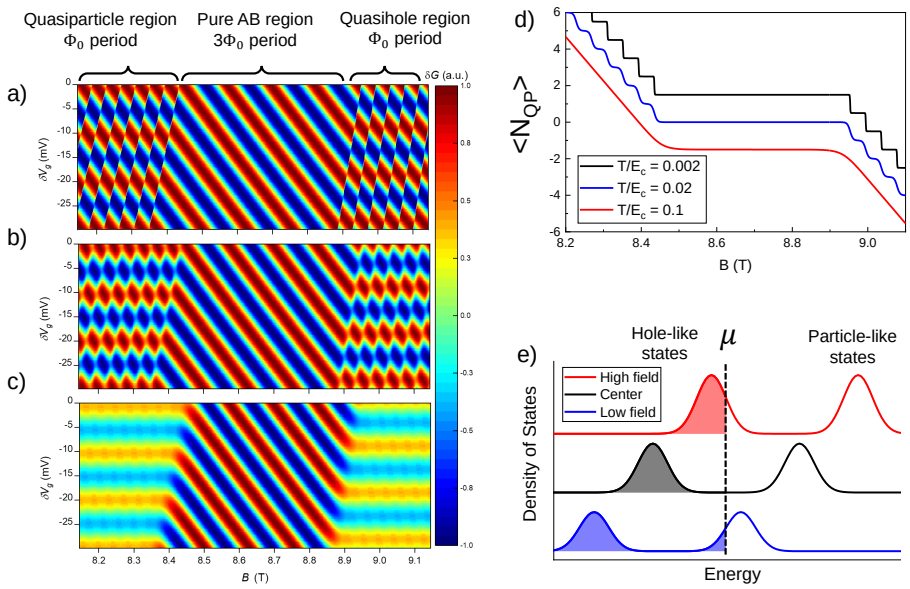

Fig. 3.12. **Simulations of interferometer behavior at $\nu = 1/3$.** Conductance values are computed as a function of magnetic field B and side gate voltages V_g, taking into account both the Aharonov-Bohm phase and the contribution θ_{anyon} from braiding around localized quasiparticles inside the bulk of the interferometer. Simulations are performed at different ratios of the temperature k_BT interferometer charging energy $E_c = \frac{e^2}{2C}$ a) 0.002 b) 0.02 and c) 0.1. d) Plot of the thermal expectation value of the number of localized quasiparticles inside the interferometer for different ratios of k_BT/E_c; in this context a negative quasiparticle number indicates a population of quasiholes. In each case in the middle of the state there are no quasiparticles, resulting in conventional Aharonov-Bohm interference with $3\Phi_0$ period, while at higher fields quasiholes form and at lower fields quasiparticles form, resulting in phase slips with Φ_0 period. As temperature is elevated, the quasiparticle number is thermally smeared, making the Φ_0 period phase slips unobservable and reducing the amplitude of the oscillations that occur as a function of V_g. e) Qualitative plot of the density of states versus energy.

3.11 Simulations

To further validate application of the model of [88] to our experimental results, we have performed simulations of interferometer behavior to model the conductance versus gate voltage V_g and magnetic field B. The starting point for this is the equation

for the interference phase difference which determines conductance oscillations, Eqn. 3.1.

The conductance for an interferometer varies as $\delta G = a_0 cos(\theta)$, with a_0 an amplitude that depends on the backscattering of the QPCs. In our system thermal fluctuations in N_{qp} may be important, so we need to calculate a thermal average (because we use low-frequency measurement techniques, this thermal average should correspond to the experimentally measured conductance). Following [36], we compute the thermal expectation value $\langle \delta G \rangle$:

$$\langle \delta G \rangle = \frac{1}{Z} \sum_{N_{qp}=-\infty}^{+\infty} e^{\frac{-E(N_{qp})}{k_B T}} \cos\left(2\pi \frac{e^*}{e} \frac{A_I B}{\Phi_0} + N_{qp}\theta_{anyon}\right) \tag{3.6}$$

$$Z = \sum_{N_{qp}=-\infty}^{+\infty} e^{\frac{-E(N_{qp})}{k_B T}} \tag{3.7}$$

Here E is the energy of the device as a function of N_{qp}. As described previously, a negative quasiparticle number here corresponds to a population of quasiholes. We define an energy similar to that in [88], but for the interferometer rather than the bulk energy per unit area:

$$E = E_0 + \frac{e^2}{2C} q_{net}^2 + \Delta_{qp} |N_{qp}| \tag{3.8}$$

E_0 is an offset accounting for the energy of the condensate which does not depend on the number of quasiparticles, so it is left out of the simulation. The absolute value of N_{qp} is multiplied by Δ_{qp} to account for the fact that quasiholes (corresponding to negative N_{qp}) also cost energy Δ_{qp}, and for simplicity we set the energy associated with creating a quasiparticle Δ_{qp} to be half of the full gap, $\Delta_{qp} = \frac{\Delta}{2}$. This is a simplification which assumes that the energy cost for creating quasiparticles is the same as for quasiholes, although numerical results have indicated that quasiparticles have a higher energy cost than quasiholes [120]. Nevertheless, the width of the constant ν region over which no quasiparticles or quasiholes are created is determined by the full gap which is a sum of the quasiparticle and quasihole gaps, $\Delta = \Delta_{qp} + \Delta_{qh}$, and this full

gap is the value measured in transport. So, asymmetry in the energies of quasiparticles and quasiholes do not affect quantitative comparison between the theory of [88] and our experimental results.

As discussed in the Period Analysis section, q_{net} is difference between the charge in the 2DES and the compensating background charge (including that created by the side gate), and is written in Eqn. 3.4. The term $\frac{e^2}{2C}\delta q_{net}^2$ in Eqn. 3.8 gives the energy cost associated with building up excess charge on the device. In the presence of screening layers separated from the main well by distance d, we estimate the characteristic capacitance to be $C = \frac{2\epsilon A_I}{d}$.

Simulations of conductance versus magnetic field and side gate voltage are performed by numerically evaluating Eqn. 3.6 and Eqn. 3.7 at each value of B and δV_g. The area A_I is computed as $A_I = A_0 + \frac{\partial A}{\partial V_g}\delta V_g$. Rather than performing an infinite sum, we sum over N_{qp} from -20 to +20 to make the computation possible; this is justified because states with large numbers of quasiparticles are exponentially suppressed. Simulations are performed for the $\nu = 1/3$ state, so based on theoretical expectations we set $\theta_{anyon} = \frac{2\pi}{3}$ and $e^* = e/3$. The value of 5.5K for Δ extracted from the bulk transport gap measurement in Fig. 3.6 was used, giving a value of 2.75K for Δ_{qp}. A 2DES of $0.7 \times 10^{11} cm^{-2}$ is assumed, which sets the background charge q_{donor}.

In Fig. 3.12a, b, and c we show the results of the simulations at different temperatures. The energy scale which primarily determines the thermal smearing effect of temperature is $\frac{e^2}{2C}$, so we set the ratio of kT to $\frac{e^2}{2C}$ at 0.002, 0.02, and 0.1 in a, b, and c. In order to make the behavior in the simulations easier to see in the plots, these simulations are performed with a device with smaller area than the real device; we set A_0=0.1μm^2, whereas for the real device $A_0 \approx 0.38\mu$m^2 based on the Aharonov-Bohm periods. We first focus on the low-temperature simulation in a). Qualitative features of the simulation match the experiment: negatively-sloped Aharonov-Bohm oscillations of period $3\Phi_0$ occur near the center, and this behavior is confined to a 530mT region (consistent with the value calculated from the model in [88] and close to the experimentally observed value of $\approx$ 450mT). Above and below this region, the

simulation in a) shows sharply defined discrete jumps in phase occurring with period Φ_0, consistent with the findings of [88]. As temperature is increased in b) and c), the transitions in these phase jumps become thermally smeared together, such that at the highest value of temperature simulated the transitions in phase are nearly completely smeared out, and the simulation shows nearly flat lines of constant conductance. This is in good qualitative agreement with the experimental results.

An additional subtle feature in the simulations is that the transition from the central Aharonov-Bohm region to quasiparticle and quasihole regions occurs across a line with positive slope in the $V_g - B$ plane, due to the coupling of the side gate to the bulk included in the simulation, α_{bulk}. This behavior is in fact observed in the experimental data in the transition to the high-field region. In the low-field transition this behavior is less clear because the transition appears to occur more smoothly rather than abruptly, but a positive slope is still observable.

In Fig. 3.12d, line cuts of the thermally averaged quasiparticle number $\langle N_{qp} \rangle$ are plotted versus B from the simulations at each temperature. At low temperatures this forms a staircase-like function with very sharp transitions when it becomes energetically favorable to change the number of localized quasiparticles, whereas at high temperatures these transitions become thermally smeared such that the evolution becomes quite smooth. While our simplified model and simulations likely do not capture all of the physics of the device, we believe that this picture of the average quasiparticle number becoming at high temperature smeared should hold. Additionally, it is possible that other mechanisms, such as charge noise, may result in smearing of $\langle N_{qp} \rangle$ on the measurement time scale.

3.12 Conclusions

We have measured conductance oscillations in Fabry-Perot interferometer across a wide range of magnetic field at the $\nu = 1/3$ quantum Hall state. Near the center of the state, we observe discrete jumps in the interference phase consistent with the anyonic

braiding statistics of localized quasiparticles, and we obtain $\theta_{anyon} = 2\pi \times (0.31 \pm 0.04)$, which agrees with the theoretically predicted value of $\theta_{anyon} = \frac{2\pi}{3}$. When the magnetic field is moved away from the center, we observe a change in interference behavior from predominantly negatively sloped lines of constant phase to a phase that is nearly independent of B. This observation suggests that the 2DES transitions from a regime of constant filling factor at the center to regimes of constant density leading to a thermally smeared population of quasiparticles (at low field) and quasiholes (at high field), as predicted in a recent theoretical work [88]. In the low and high field regimes we observe a dramatic increase in thermal dephasing evidenced by the suppression the temperature decay scale T_0, which indicates that despite their large spatial separation from the interfering edge state, localized quasiparticles have a profound impact on interference behavior through their braiding statistics.

3.13 Methods

The device used was fabricated using the following steps: (1) optical lithography and wet etching to define the mesa; (2) deposition and annealing of Ni/Au/Ge Ohmic contacts; (3) electron beam lithography and electron beam evaporation (5nm Ti/10nm Au) to define the interferometer gates; (4) optical lithography and electron beam evaporation (20nm Ti/150nm Au) to define bondpads and surface gates around the Ohmic contacts; (5) mechanical polishing to thin the GaAs substrate; (6) optical lithography and electron beam evaporation (200nm Ti/150nm Au) to define the backgates used to deplete the bottom SW around the Ohmic contacts so that only the primary quantum well is probed.

Standard low-frequency (f = 13Hz) 4-terminal and 2-terminal lock-in amplifier techniques were used to probe the diagonal resistance and conductance across the device. Typically a 50pA excitation current was used for measurements. A +600mV bias was applied to the QPC and side gates while the device was cooled from room

temperature; this bias-cool technique results in an approximately 600mV built-in bias on these gates, which was found to improve device stability.

3.14 Acknowledgements

This material is based on work supported by the U.S. Department of Energy, Office of Science, Office of Basic Energy Sciences, under award number DE-SC0020138.

References

4. CONCLUSIONS

4.1 Summary of Progress

A significant breakthrough we achieved in this work is a dramatic improvement in the coherence of quantum Hall Fabry-Perot interferometers. The screening well heterostructure enables devices which are an order of magnitude smaller and can still operate in the Aharonov-Bohm regime. I suspect that the screening well structure's ability to increase the sharpness of the confining potential is also critical, but this is hard to quantify and compare to previous results since data from devices without screening wells is already quite limited.

This great improvement has enabled a few interesting results in the quantum Hall regime. The first is mapping the edge state velocity of different Landau level edge states versus filling factor, which previously was not possible for inner edge states due to poor coherence. This was an interesting result on its own, but an additional consequence was that it allowed us to validate the numerical results developed by our collaborators [55]. The numerical simulations showed surprisingly good agreement with the experiment; I find this an impressive demonstration of the predictive value of numerical work (it's worth emphasizing that most of the simulations were done before any experimental data was available, so no "tweaking" was done to improve the simulation after the fact).

The second result is Aharonov-Bohm interference at the fractional quantum Hall states $\nu = 1/3$ and $\nu = 2/3$, which was not possible in large devices without screening wells. This was the first clear demonstration (including negatively-sloped pajama plot stripes) of AB interference at a fractional state despite significant past experimental efforts. Occasionally the question comes up "Are quasiparticles real particles", and the typical answer is "What do you mean by 'real'?". Now we can say that the fra-

cional quantum Hall quasiparticles are real enough to exhibit a fundamental quantum mechanical phenomenon, the Aharonov-Bohm effect.

The final major result is direct evidence for quasiparticle braiding statistics described in the previous chapter. Nearly all of the results in this chapter were anticipated in the theoretical work by Rosenow and Stern [88], including both the discrete jumps near the center of the $\nu = 1/3$ plateau and the transition in behavior away from the center. In this work we see evidence for quasiparticle braiding both in the limit of a sparse quasiparticle population, where individual phase jumps can be seen, and in the limit of a large number of thermally smeared quasiparticles or quasiholes at low and high field. The screening well structure was necessary in multiple aspects of this experiment. It enabled the use of small devices with good coherence of AB interference at the $\nu = 1/3$ state, which wasn't possible with previous non-SW experiments. Second, it improves the sharpness of the confining potential, which might be critical to avoid decoherence. Finally, the screening creates the region near the center of the state where individual phase jumps can be observed.

4.2 Antidot gate devices

My original proposal for creating quasiparticles and measuring the anyonic phase was to modify the device design by including an additional "antidot" gate in the middle of the device to electrostatically generate quasiparticles inside the interference path. A preliminary CAD design for such a device is shown in Fig. 4.1. This design would utilize two separate electron beam lithography steps to define the primary interference path and the antidot gate in the middle, and the two gate layers would be separated by a dielectric. Although I did fabricate such devices, for some reason they ended up being too noisy to work correctly. This was strange, since the noise occurs when the QPC gates are biased, but devices in the same round of processing that had the same QPCs but didn't get the dielectric or overlaid antidot gate were much less noisy. So, somehow the dielectric deposition or additional gate addition

made the underlying QPC gates very noisy. My suspicion is that the overlay electron beam lithography somehow causes some damage that induces noise, but a simpler explanation would be that the dielectric causes some problems - it's been suggested that we should de a plasma descum before the dielectric ALD depisition to ensure the surface is free of photoresist contamination.

Since these antidot gates didn't work, it was fortunate that it turned out to be possible to create quasiparticles with magnetic field/side gate voltage for braiding. However, it is still desirable to have better control of quasiparticle creation with an antidot gate, which might be especially important for the $\nu = 5/2$ state where quasiparticles need to be kept away from the interfering edge to avoid decoherence by Majorana hopping. Therefore, in the future it will be useful to optimize device fabrication in order to eliminate the excess noise in these antidot-gated devices.

4.3 Exploring limits to device size

It is noteworthy that, although we have measured AB interference in a much smaller device than has been previously reported using the screening well heterostructure design, we have not yet fully explored the limits of how small a device it is possible to make before the interferometer becomes Coulomb dominated. Smaller devices would be desirable to further improve coherence (which may be important for observing interference in some of the more fragile fractional Hall states). Interesting behavior is predicted in the intermediate regime between Aharonov-Bohm and Coulomb dominated behavior [36], and this itself is worth exploring. Therefore, a future project will be to fabricate a series of interferometers with the screening well structure and determine the minimum device size for which AB regime interference may be measured, and map out the transition from AB to Coulomb-dominated behavior as device size is decreased further.

I have done some of this work already. In $0.8\mu\text{m}\times0.8\mu\text{m}$ and $0.7\mu\text{m}\times0.7\mu\text{m}$ devices I have observed intermediate regime behavior at $\nu = 1$. Unfortunately these devices

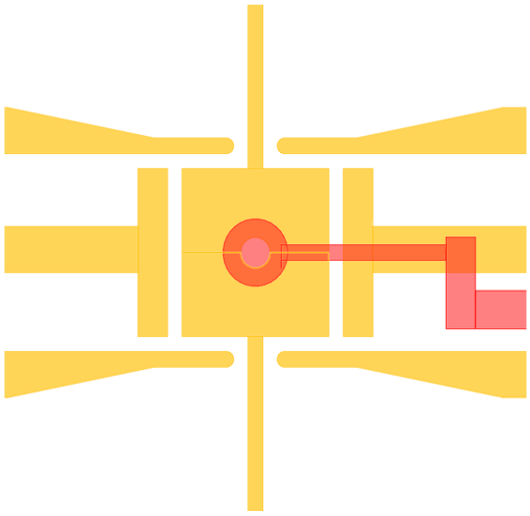

Fig. 4.1. **CAD design for an interferometer with an "antidot" gate in the middle to create quasiparticles.** The gates that define the interference path are shown in yellow, in addition to a center grounded gate, similar to to the interferometer design used in the previous chapter. An additional gate which extends into the middle of the device is included and shown in red. When negatively biased, this red gate will deplete charge in the middle of the interferometer, leading to the creation of quasiparticles, which should result in a shift in the interference path due to the anyonic phase. The center yellow gate has a round hole in the middle to allow the red gate to deplete charge in the interferometer. The two gate layers will be separated by a dielectric.

were zapped and damaged, so new devices will need to be fabricated. It would be interesting to test these sorts of devices at $\nu = 1/3$ and see the effect of intermediate regime behavior on braiding.

4.4 $\nu = 5/2$: Possible non-Abelian quantum Hall state

An intriguing possibility is that some special quantum Hall states beyond those described in the composite fermion picture may host so-called "non-Abelian anyon" quasiparticles. These quasiparticles are even more exotic than the (Abelian) anyons of the composite fermion states. For Abelian anyons, braiding results in simply a phase factor, which we have experimentally measured. For non-Abelian states, however, the ground state of the system is degenerate, and braiding may result in a transition from one ground state to another. This has been proposed as a means to build a topological quantum computer, and furthermore Fabry-Perot interferometry has been proposed as a way to probe the potentially non-Abelian properties of quasiparticles [39, 50]. Therefore, it is a major goal to extend interferometry to the potentially non-Abelian states, which are most likely to exist in the second Landau level. Even more intriguingly, a double-interferometer structure has been proposed as a means to realize a topologically protected qubit [50]. The most promising state is $\nu = 5/2$, which has drawn considerable experimental and theoretical work.

While there is significant incentive to perform interference at $\nu = 5/2$, there are also major challenges. The first is that $\nu = 5/2$ is an extremely fragile state, and requires specially designed heterostructures with extremely low disorder and high electron density to be observed; the screening well structure will require significant modification to be compatible with these requirements. An additional difficulty is that the $\nu = 5/2$ edge mode is an inner mode and thus may have low edge velocity and poor coherence; furthermore a theoretical work has shown that $\nu = 5/2$ is extremely susceptible to decoherence when the confining potential is too shallow [83]. For these reasons I suspect it will be very difficult to get interference to work at $\nu = 5/2$.

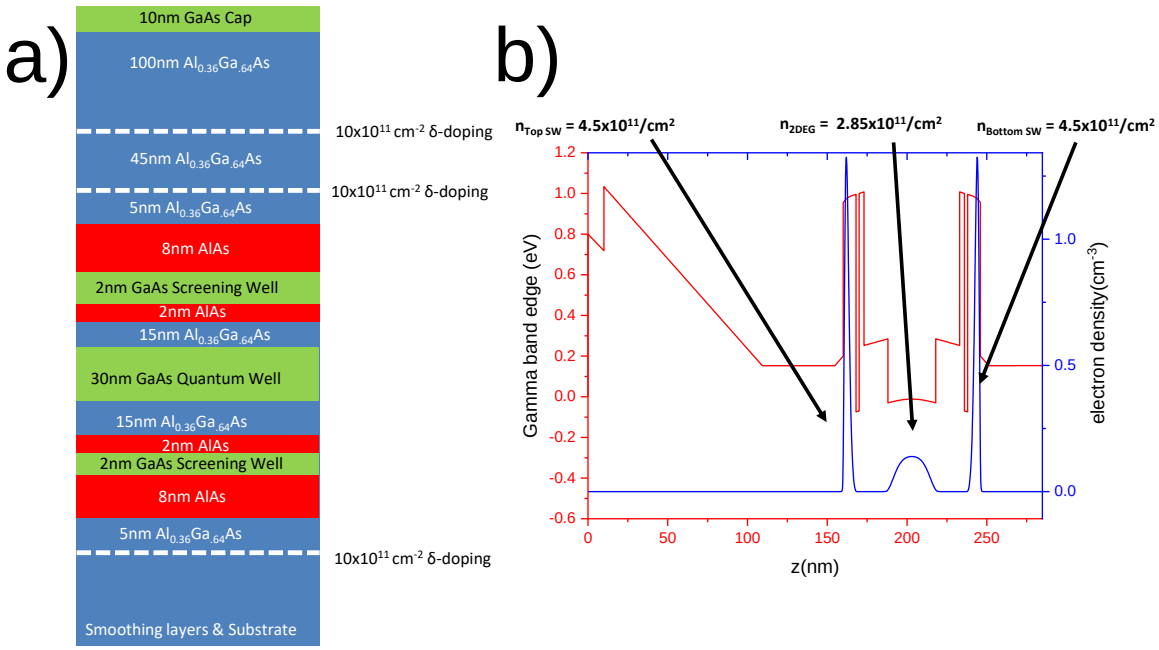

Fig. 4.2. **Possible heterostructure for $\nu = 5/2$ interference experiments.** a) Layer stack, with wide AlAs layers in the SWs in which the electrons will sit. b) Nextnano simulation of this structure.

Nevertheless, it is worth trying, and the first step will be do design a screening well heterostructure with low enough disorder and high enough electron density to support the state.

Also noteworthy is that the non-Abelian quasiparticles at $\nu = 5/2$ are predicted to have charge $e^* = e/4$, so the characteristic charging energy $\frac{e^{*2}}{2C}$ will be even smaller, making it difficult to maintain fixed quasiparticle number at experimental temperatures. One way to deal with this would be to reduce screening to reduce C, which might be possible by making the screening wells worse at screening somehow. However, increasing the SW setback isn't a good way to do this because then the confining potential will be less sharp and you will get edge reconstruction. It might be possible to make the 2DES in the SWs highly disordered so that they don't conduct well. Of course, a tradeoff is that disorder that affects the SW may also reduce the quality of

the QW, and then you won't get a good 5/2 state. An additional necessity is high electron density in the main QW, because a high density (to get high characteristic Coulomb energy) is needed to get a decent 5/2 gap as well.

A possible heterostructure design is shown in Fig. 4.2a, with a nextnano simulation shown in Fig. 4.2b. This structure screening wells with wide outer AlAs barrier and narrow GaAs wells so that the electrons will sit in the outer AlAs in the X-band. Also, AlAs has higher mass than GaAs, so the mobility will be lower and hopefully they won't screen as well. The donors are also a shorter setback from the SWs which will make the SWs more disordered; hopefully this won't affect the QW too much, but that remains to be seen. Because of the relatively high offset of the GaAs band minimum from AlAs, this will give a higher electron density. For this structure I also reduced the setback of the SWs from the QW to hopefully achieve a sharper confining potential and higher QW density. Numerical results have suggested that a very sharp confining potential is needed to get interference of the non-Abelian edge quasiparticles [83].

You might wonder whether reducing the screening of the screening wells is acceptable. For the Abelian states such as $\nu = 1/3$, the screening wells must be good at screening because bulk-edge interaction reduces the visibility of the braiding phase shift θ_{anyon} [36]. However, at $\nu = 5/2$ the non-Abelian nature of the quasiparticles means that the effect of braiding is not simply a phase shift. Instead the prediction is that we will see the even-odd effect where interference disappears for an odd number of quasiparticles, because braiding has effectively changed the state and the different backscattered paths are orthogonal, and re-appears when an even number of quasiparticles are inside the device [39, 50, 111–113]. Since this isn't just a phase, it should be fine the have strong bulk-edge interaction since you will still be able to tell whether or not oscillations occur as a function of B or V_g. The periodicities in the case of AB, intermediate, and CD regime devices have been analyzed theoretically in [54], and most it was found that bulk-edge coupling does not affect the side-gate oscillation pe-

riod. So, unlike Abelian braiding, non-Abelian effects should be observable through interference even in the case of a Coulomb-dominated device.

REFERENCES

REFERENCES

[1] M. J. Manfra, "Molecular Beam Epitaxy of Ultra-High Quality AlGaAs/GaAs Heterostructures: Enabling Physics in Low-Dimensional Electronic Systems," *Annual Review of Condensed Matter Physics*, vol. 5, pp. 347–373, 2014.

[2] V. Umansky, M. Heiblum, Y. Levinson, J. Smet, J. Nuebler, and M. Dolev, "MBE growth of ultra-low disorder 2DEG with mobility exceeding 35x10^6 cm2/Vs," *Journal of Crystal Growth*, vol. 311, no. 7, pp. 1658–1661, 2009.

[3] G. C. Gardner, S. Fallahi, J. D. Watson, and M. J. Manfra, "Modified MBE hardware and techniques and role of gallium purity for attainment of two dimensional electron gas mobility >35x10^6cm2/V s in AlGaAs/GaAs quantum wells grown by MBE," *Journal of Crystal Growth*, vol. 441, pp. 71–77, 2016.

[4] S. Birner, T. Zibold, T. Andlauer, T. Kubis, M. Sabathil, A. Trellakis, and P. Vogl, "nextnano: General purpose 3-d simulations," *IEEE Transactions on Electron Devices*, vol. 54, no. 9, pp. 2137–2142, Sept 2007.

[5] R. Dingle, H. L. Stormer, A. C. Gossard, and W. Wiegmann, "Electron mobilities in modulation-doped semiconductor heterojunction superlattices," *Appl. Phys. Lett.*, vol. 33, p. 1888, 1978.

[6] J. D. Watson, "Growth of low disorder gaas/algaas heterostructures by molecular beam epitaxy for the study of correlated electron phases in two dimensions," Ph.D. dissertation, Purdue University, 5 2015.

[7] M. Heiblum, E. E. Mendez, and F. Stern, "High mobility electron gas in selectively doped n:algaas/gaas heterojunctions," *Appl. Phys. Lett.*, vol. 44, p. 1064, 1984.

[8] L. Pfeiffer, K. W. West, H. L. Stormer, , and K. W. Baldwin, "Electron mobilities exceeding 10^7 cm2/vs in modulation-doped gaas," *Appl. Phys. Lett.*, vol. 55, p. 1888, 1989.

[9] V. Umansky, R. de Picciotto, and M. Heiblum, "Extremely high-mobility two dimensional electron gas: evaluation of scattering mechanisms," *Appl. Phys. Lett.*, vol. 71, p. 683, 1997.

[10] L. Pfeiffer and K. W. West, "The role of mbe in recent quantum hall effect physics discoveries," *Physica E*, vol. 20, p. 57, 2003.

[11] K. V. Klitzing, G. Dorda, and M. Pepper, "New method for high-accuracy determination of the fine-structure constant based on quantized hall resistance," *Physical Review Letters*, vol. 45, no. 6, pp. 494–497, 1980.

[12] K. von Klitzing, "Quantum Hall Effect: Discovery and Application," *Annual Review of Condensed Matter Physics*, vol. 8, no. 1, pp. 13–30, 2017.

[13] B. I. Halperin, "Quantized hall conductance, current-carrying edge states, and the existence of extended states in a two-dimensional disordered potential," *Phys. Rev. B*, vol. 25, pp. 2185–2190, Feb 1982.

[14] A. M. M. Pruisken, "On localization in the theory of teh quantized hall effect: a two-dimensional realization of the θ-vacuum," *Nucl. Phys. B*, vol. 235, pp. 277–298, 1984.

[15] R. B. Laughlin, "Quantized hall conductivity in two dimensions," *Phys. Rev. B*, vol. 23, pp. 5632–5633, May 1981.

[16] D. J. Thouless, M. Kohmoto, M. P. Nightingale, and M. den Nijs, "Quantized hall conductance in a two-dimensional periodic potential," *Phys. Rev. Lett.*, vol. 49, pp. 405–408, Aug 1982.

[17] Q. Niu, D. J. Thouless, and Y.-S. Wu, "Quantized hall conductance as a topological invariant," *Phys. Rev. B*, vol. 31, pp. 3372–3377, Mar 1985.

[18] D. C. Tsui, H. L. Stormer, and A. C. Gossard, "Two-dimensional magnetotransport in the extreme quantum limit," *Physical Review Letters*, vol. 48, no. 22, pp. 1559–1562, 1982.

[19] D. C. Tsui, H. L. Störmer, J. C. M. Hwang, J. S. Brooks, and M. J. Naughton, "Observation of a fractional quantum number," *Phys. Rev. B*, vol. 28, pp. 2274–2275, Aug 1983.

[20] H. L. Stormer, D. C. Tsui, and A. C. Gossard, "The fractional quantum Hall effect," *Reviews of Modern Physics*, vol. 71, no. 2, pp. S298–S305, 1999.

[21] R. B. Laughlin, "Anomalous quantum Hall effect: An incompressible quantum fluid with fractionally charged excitations," *Physical Review Letters*, vol. 50, no. 18, pp. 1395–1398, 1983.

[22] A. M. Chang, M. A. Paalanen, D. C. Tsui, H. L. Störmer, and J. C. M. Hwang, "Fractional quantum hall effect at low temperatures," *Phys. Rev. B*, vol. 28, pp. 6133–6136, Nov 1983.

[23] A. M. Chang, P. Berglund, D. C. Tsui, H. L. Stormer, and J. C. M. Hwang, "Higher-order states in the multiple-series, fractional, quantum hall effect," *Phys. Rev. Lett.*, vol. 53, pp. 997–1000, Sep 1984.

[24] G. S. Boebinger, A. M. Chang, H. L. Stormer, and D. C. Tsui, "Magnetic field dependence of activation energies in the fractional quantum hall effect," *Phys. Rev. Lett.*, vol. 55, pp. 1606–1609, Oct 1985.

[25] R. Willett, J. P. Eisenstein, H. L. Störmer, D. C. Tsui, A. C. Gossard, and J. H. English, "Observation of an even-denominator quantum number in the fractional quantum hall effect," *Phys. Rev. Lett.*, vol. 59, pp. 1776–1779, Oct 1987.

[26] A. Kumar, G. A. Csáthy, M. J. Manfra, L. N. Pfeiffer, and K. W. West, "Nonconventional odd-denominator fractional quantum hall states in the second landau level," *Phys. Rev. Lett.*, vol. 105, p. 246808, Dec 2010.

[27] J. K. Jain, "Composite-Fermion Approach for the Fractional Quantum Hall Effec," *Physical Review Letters*, vol. 63, no. 2, pp. 199–202, 1989.

[28] ——, "Composite Fermion Theory of Exotic Fractional Quantum Hall Effect," *Annual Review of Condensed Matter Physics*, vol. 6, no. 1, pp. 39–62, 2014.

[29] ——, *Composite Fermions*. Cambridge: Cambridge University Press, 2007.

[30] W. Pan, J.-S. Xia, V. Shvarts, D. E. Adams, H. L. Stormer, D. C. Tsui, L. N. Pfeiffer, K. W. Baldwin, and K. W. West, "Exact quantization of the even-denominator fractional quantum hall state at $\nu = 5/2$ landau level filling factor," *Phys. Rev. Lett.*, vol. 83, pp. 3530–3533, Oct 1999.

[31] J. P. Eisenstein, K. B. Cooper, L. N. Pfeiffer, and K. W. West, "Insulating and fractional quantum hall states in the first excited landau level," *Phys. Rev. Lett.*, vol. 88, p. 076801, Jan 2002.

[32] G. Moore and N. Read, "Nonabelions in the fractional quantum hall effect," *Nuclear Physics B*, vol. 360, no. 2-3, pp. 362–396, 1991.

[33] E. H. Rezayi and F. D. M. Haldane, "Incompressible paired hall state, stripe order, and the composite fermion liquid phase in half-filled landau levels," *Phys. Rev. Lett.*, vol. 84, pp. 4685–4688, May 2000.

[34] D. Arovas, "Fractional Statistics and the Quantum Hall Effect," *Physical Review Letters*, vol. 53, no. 7, 1984.

[35] S. A. Kivelson and V. L. Pokrovsky, "Methods to measure the charge of the quasiparticles in the fractional quantum Hall effect," *Physical Review B*, vol. 40, no. 2, pp. 1373–1376, 1989.

[36] B. I. Halperin, A. Stern, I. Neder, and B. Rosenow, "Theory of the Fabry-Perot quantum Hall interferometer," *Physical Review B - Condensed Matter and Materials Physics*, vol. 83, no. 15, p. 15440, 2011.

[37] B. I. Halperin, "Statistics of quasiparticles and the hierarchy of fractional quantized hall states," *Physical Review Letters*, vol. 52, no. 18, pp. 1583–1586, 1984.

[38] C. D. C. Chamon, D. E. Freed, S. a. Kivelson, S. L. Sondhi, and X. G. Wen, "Two point-contact interferometer for quantum Hall systems," *Physical Review B*, vol. 55, no. 4, pp. 2331–2343, 1997.

[39] A. Stern and B. I. Halperin, "Proposed experiments to probe the non-abelian ν=5/2 quantum hall state," *Physical Review Letters*, vol. 96, no. 1, pp. 1–4, 2006.

[40] B. Rosenow and B. I. Halperin, "Influence of interactions on flux and back-gate period of quantum hall interferometers," *Physical Review Letters*, vol. 98, no. 10, pp. 1–4, 2007.

[41] V. J. S. B. Goldman, "Resonant Tunneling in the Quantum Hall Regime: Measurement of Fractional Charge," *Science*, vol. 267, no. 5200, pp. 1010–1012, 1995.

[42] A. Kou, C. M. Marcus, L. N. Pfeiffer, and K. W. West, "Coulomb oscillations in antidots in the integer and fractional quantum hall regimes," *Physical Review Letters*, vol. 108, no. 25, pp. 1–5, 2012.

[43] Y. Ji, Y. Chung, D. Sprinzak, M. Heiblum, and D. Mahalu, "An electronic Mach – Zehnder interferometer," *Nature*, vol. 422, no. 8, pp. 415–418, 2003.

[44] I. Gurman, R. Sabo, M. Heiblum, V. Umansky, and D. Mahalu, "Dephasing of an Electronic Two-Path Interferometer," *Physical Review B*, vol. 121412, p. 14, 2016.

[45] N. Ofek, A. Bid, M. Heiblum, A. Stern, V. Umansky, and D. Mahalu, "Role of interactions in an electronic Fabry-Perot interferometer operating in the quantum Hall effect regime." *Proceedings of the National Academy of Sciences of the United States of America*, vol. 107, no. 12, pp. 5276–5281, 2010.

[46] Y. Zhang, D. T. McClure, E. M. Levenson-Falk, C. M. Marcus, L. N. Pfeiffer, and K. W. West, "Distinct signatures for coulomb blockade and aharonov-Bohm interference in electronic Fabry-Perot interferometers," *Physical Review B - Condensed Matter and Materials Physics*, vol. 79, no. 24, pp. 1–4, 2009.

[47] P. V. Lin, F. E. Camino, and V. J. Goldman, "Electron interferometry in the quantum hall regime: Aharonov-Bohm effect of interacting electrons," *Physical Review B - Condensed Matter and Materials Physics*, vol. 80, no. 12, pp. 1–6, 2009.

[48] I. Sivan, H. K. Choi, J. Park, A. Rosenblatt, Y. Gefen, D. Mahalu, and V. Umansky, "Observation of interaction-induced modulations of a quantum Hall liquid's area," *Nature Communications*, vol. 7, pp. 1–9, 2016.

[49] J. Nakamura, S. Fallahi, H. Sahasrabudhe, R. Rahman, S. Liang, G. C. Gardner, and M. J. Manfra, "Aharonov–Bohm interference of fractional quantum Hall edge modes," *Nature Physics*, 2019.

[50] S. D. Sarma, M. Freedman, and C. Nayak, "Topologically protected qubits from a possible non-abelian fractional quantum hall state," *Physical Review Letters*, vol. 94, no. 16, pp. 1–4, 2005.

[51] E. A. Kim, "Aharanov-Bohm interference and fractional statistics in a quantum Hall interferometer," *Physical Review Letters*, vol. 97, no. 21, pp. 3–6, 2006.

[52] P. V. Lin, F. E. Camino, and V. J. Goldman, "Superperiods in interference of e/3 Laughlin quasiparticles encircling filling 2/5 fractional quantum Hall island," *Physical Review B - Condensed Matter and Materials Physics*, vol. 80, no. 23, pp. 1–7, 2009.

[53] S. Baer, C. Rössler, T. Ihn, K. Ensslin, C. Reichl, and W. Wegscheider, "Cyclic depopulation of edge states in a large quantum dot," *New Journal of Physics*, vol. 15, 2013.

[54] C. W. Von Keyserlingk, S. H. Simon, and B. Rosenow, "Enhanced Bulk-Edge Coulomb Coupling in Fractional Fabry-Perot Interferometers," *Physical Review Letters*, vol. 115, no. 12, pp. 1–5, 2015.

[55] H. Sahasrabudhe, B. Novakovic, J. Nakamura, S. Fallahi, M. Povolotskyi, G. Klimeck, R. Rahman, and M. J. Manfra, "Optimization of edge state velocity in the integer quantum Hall regime," *Physical Review B*, vol. 97, no. 8, pp. 1–11, 2018.

[56] J. P. Eisenstein, L. N. Pfeiffer, and K. W. West, "Independently contacted two-dimensional electron systems in double quantum wells," *Applied Physics Letters*, vol. 57, no. 22, pp. 2324–2326, 1990.

[57] C. W. J. Beenakker, "Theory of Coulomb-blockade oscillations in the conductance of a quantum dot," *Physical Review B*, vol. 44, no. 4, pp. 1646–1656, 1991.

[58] D. T. McClure, "Interferometer-based studies of quantum hall phenomena," Ph.D. dissertation, Harvard University, 5 2012.

[59] P. Roulleau, F. Portier, P. Roche, A. Cavanna, G. Faini, U. Gennser, and D. Mailly, "Direct measurement of the coherence length of edge states in the integer quantum hall regime," *Physical Review Letters*, vol. 100, no. 12, pp. 6–9, 2008.

[60] D. T. McClure, Y. Zhang, B. Rosenow, E. M. Levenson-Falk, C. M. Marcus, L. N. Pfeiffer, and K. W. West, "Edge-state velocity and coherence in a quantum hall Fabry-Pérot interferometer," *Physical Review Letters*, vol. 103, no. 20, pp. 1–4, 2009.

[61] H. K. Choi, I. Sivan, a. Rosenblatt, M. Heiblum, V. Umansky, and D. Mahalu, "Robust electron pairing in the integer quantum hall effect regime," *Nature Communications*, vol. 6, no. May, p. 7435, 2015.

[62] I. Sivan, R. Bhattacharyya, H. K. Choi, M. Heiblum, D. E. Feldman, D. Mahalu, and V. Umansky, "Interaction-induced interference in the integer quantum Hall effect," *Physical Review B*, vol. 97, no. 12, 2018.

[63] G. A. Frigeri, D. D. Scherer, and B. Rosenow, "Subperiods and apparent pairing in integer quantum Hall interferometers," *Arxiv preprint*, 2017.

[64] D. B. Chklovskii, B. I. Shklovskii, and L. I. Glazman, "Electrostatics of edge channels," *Physical Review B*, vol. 46, no. 7, pp. 4026–4034, 1992.

[65] D. B. Chklovskii, K. A. Matveev, and B. I. Shklovskii, "Ballistic conductance of interacting electrons in the quantum Hall regime," *Physical Review B*, vol. 47, no. 19, pp. 12 605–12 617, 1993.

[66] G. Montambaux, "Semiclassical quantization of skipping orbits," *European Physical Journal B*, vol. 79, no. 2, pp. 215–224, 2011.

[67] D. T. McClure, W. Chang, C. M. Marcus, L. N. Pfeiffer, and K. W. West, "Fabry-Perot interferometry with fractional charges," *Physical Review Letters*, vol. 108, no. 25, pp. 1–5, 2012.

[68] F. E. Camino, W. Zhou, and V. J. Goldman, "Aharonov-Bohm superperiod in a Laughlin quasiparticle interferometer," *Physical Review Letters*, vol. 95, no. 24, pp. 1–4, 2005.

[69] ——, "e/3 Laughlin quasiparticle primary-filling ν=1/3 interferometer," *Physical Review Letters*, vol. 98, no. 7, pp. 3–6, 2007.

[70] R. L. Willett, L. N. Pfeiffer, and K. W. West, "Measurement of filling factor 5/2 quasiparticle interference with observation of charge e/4 and e/2 period oscillations," *Proceedings of the National Academy of Sciences*, vol. 106, no. 22, pp. 8853–8858, 2009.

[71] R. L. Willett, C. Nayak, K. Shtengel, L. N. Pfeiffer, and K. W. West, "Magnetic-field-tuned aharonov-bohm oscillations and evidence for non-abelian anyons at ν=5/2," *Physical Review Letters*, vol. 111, no. 18, pp. 1–5, 2013.

[72] D. De-Picciotto, R; Reznikov, M; Heiblum, M; Umansky, V; Bunin, G; Mahalu, "Direct observation of a fractional charge.pdf," *Nature*, vol. 389, no. September, pp. 1996–1998, 1997.

[73] S. M. Girvin, "Particle-hole symmetry in the anomalous quantum Hall effect," *Physical Review B*, vol. 29, no. 10, pp. 6012–6014, 1984.

[74] A. H. MacDonald, "Edge states in the fractional-quantum-Hall-effect regime," *Physical Review Letters*, vol. 64, no. 2, pp. 220–223, 1990.

[75] A. M. Chang, "A unified transport theory for the integral and fractional quantum hall effects: Phase boundaries, edge currents, and transmission/reflection probabilities," *Solid State Communications*, vol. 74, no. 9, pp. 871–876, 1990.

[76] C. Beenakker, "Edge channels for the fractional quantum Hall effect," *Physical Review Letters*, vol. 64, no. 2, pp. 216–219, 1990.

[77] Y. Meir, "Composite Edge States in the nu=2/3 Fractional Quantum Hall Regime," *Physical Review Letters*, vol. 72, no. 16, pp. 2624–2627, 1994.

[78] C. L. Kane, M. P. A. Fisher, and J. Polchinski, "Randomness at the Edge: Theory of Quantum Hall Transport at Filling v = 2/3," *Physical Review Letters*, vol. 72, no. 26, pp. 4129–4132, 1994.

[79] A. Bid, N. Ofek, M. Heiblum, V. Umansky, and D. Mahalu, "Shot Noise and Fractional Charge at the 2/3 Composite Fractional Edge Channel," *Physical Review Letters*, vol. 0911, no. 103, p. 236802, 2009.

[80] R. Sabo, I. Gurman, A. Rosenblatt, F. Lafont, D. Banitt, J. Park, M. Heiblum, Y. Gefen, V. Umansky, and D. Mahalu, "Edge reconstruction in fractional quantum Hall states," *Nature Physics*, vol. 13, no. May, pp. 491–496, 2017.

[81] X. Wan, K. Yang, and E. H. Rezayi, "Reconstruction of fractional quantum Hall edges," *Physical Review Letters*, vol. 88, no. 5, pp. 568 021–568 024, 2002.

[82] Y. Joglekar, H. Nguyen, and G. Murthy, "Edge reconstructions in fractional quantum Hall systems," *Physical Review B*, vol. 68, no. 3, p. 035332, 2003.

[83] Z. X. Hu, E. H. Rezayi, X. Wan, and K. Yang, "Edge-mode velocities and thermal coherence of quantum Hall interferometers," *Physical Review B - Condensed Matter and Materials Physics*, vol. 80, no. 23, pp. 1–6, 2009.

[84] M. Goldstein and Y. Gefen, "Suppression of Interference in Quantum Hall Mach-Zehnder Geometry by Upstream Neutral Modes," *Physical Review Letters*, vol. 117, no. 27, pp. 1–6, 2016.

[85] J. Park, Y. Gefen, and H.-S. Sim, "Topological dephasing in the $\nu = 2/3$ fractional quantum Hall regime," *Physical Review B*, vol. 92, no. 24, p. 245437, 2015.

[86] H. Inoue, A. Grivnin, Y. Ronen, M. Heiblum, V. Umansky, and D. Mahalu, "Proliferation of neutral modes in fractional quantum Hall states." *Nature communications*, vol. 5, no. May, p. 4067, 2014.

[87] K. Du, R. R.; Stormer, H. L.; Tsui, D. C.; Pfeiffer, L. N.; West, "Experimental Evidence for New Particles in the Fractional Quantum Hall Effect," *Physical Review Letters*, vol. 70, pp. 2944–2947, 1993.

[88] B. Rosenow and A. Stern, "Flux Superperiods and Periodicity Transitions in Quantum Hall Interferometers," *Physical Review Letters*, vol. 124, no. 10, p. 106805, 2020.

[89] J. M. Leinaas and J. Myrheim, "On the theory of identical particles," *Nuovo Cim B*, pp. 1–23, 1977.

[90] F. Wilczek, "Quantum mechanics of fractional-spin particles," *Physical Review Letters*, vol. 49, no. 14, pp. 957–959, 1982.

[91] C. Nayak, S. H. Simon, A. Stern, M. Freedman, and S. Das Sarma, "Non-Abelian anyons and topological quantum computation," *Reviews of Modern Physics*, vol. 80, no. 3, pp. 1083–1159, 2008.

[92] H. Kjønsberg and J. Myrheim, "Numerical study of charge and statistics of Laughlin quasiparticles," *International Journal of Modern Physics A*, vol. 14, no. 4, pp. 537–557, 1999.

[93] H. Kjønsberg and J. M. Leinaas, "Charge and statistics of quantum Hall quasiparticles - A numerical study of mean values and fluctuations," *Nuclear Physics B*, vol. 559, no. 3, pp. 705–742, 1999.

[94] G. S. Jeon, K. L. Graham, and J. K. Jain, "Fractional Statistics in the Fractional Quantum Hall Effect," *Physical Review Letters*, vol. 91, no. 3, pp. 1–4, 2003.

[95] ——, "Berry phases for composite fermions: Effective magnetic field and fractional statistics," *Physical Review B - Condensed Matter and Materials Physics*, vol. 70, no. 12, pp. 1–14, 2004.

[96] A. Stern, "Anyons and the quantum hall effect—a pedagogical review," *Annals of Physics*, vol. 323, pp. 204–249, 2013.

[97] S. D. Sarma, M. Freedman, and C. Nayak, "Majorana Zero Modes and Topological Quantum Computation," *Nature Publishing Group*, vol. 1, no. May, p. 15001, 2015.

[98] H. Bartolomei, M. Kumar, R. Bisognin, A. Marguerite, E. Bocquillon, A. Cavanna, Q. Dong, U. Gennser, and Y. Jin, "Fractional statistics in anyon collisions," *Science*, vol. 2, no. April, pp. 173–177, 2020.

[99] B. Rosenow and S. H. Simon, "Telegraph noise and the Fabry-Perot quantum Hall interferometer," *Physical Review B - Condensed Matter and Materials Physics*, vol. 85, no. 20, pp. 1–5, 2012.

[100] I. P. Levkivskyi, J. Frohlich, and E. V. Sukhorukov, "Theory of fractional quantum Hall interferometers," *Physical Review B - Condensed Matter and Materials Physics*, vol. 86, no. 24, pp. 1–21, 2012.

[101] S. D. D. Frigeri, Giovanni A. and B. Rosenow, "Sub-periods and apparent pairing in integer quantum Hall interferometers," *Europhysics Letters*, vol. 126, no. 6, 2019.

[102] L. V. Litvin, A. Helzel, H. P. Tranitz, W. Wegscheider, and C. Strunk, "Edge-channel interference controlled by Landau level filling," *Physical Review B - Condensed Matter and Materials Physics*, vol. 78, no. 7, pp. 2–5, 2008.

[103] E. Deviatov and a. Lorke, "Experimental realization of a Fabry-Perot-type interferometer by copropagating edge states in the quantum Hall regime," *Physical Review B*, vol. 77, no. 16, pp. 2–5, 2008.

[104] E. V. Deviatov, A. Ganczarczyk, A. Lorke, G. Biasiol, and L. Sorba, "Quantum Hall Mach-Zehnder interferometer far beyond equilibrium," *Physical Review B - Condensed Matter and Materials Physics*, vol. 84, no. 23, pp. 1–6, 2011.

[105] P.-A. Huynh, F. Portier, H. le Sueur, G. Faini, U. Gennser, D. Mailly, F. Pierre, W. Wegscheider, and P. Roche, "Quantum Coherence Engineering in the Integer Quantum Hall Regime," *Physical Review Letters*, vol. 108, no. 25, p. 256802, 2012.

[106] S. Tewari, P. Roulleau, C. Grenier, F. Portier, A. Cavanna, U. Gennser, D. Mailly, and P. Roche, "Robust quantum coherence above the Fermi sea," *Physical Review B - Condensed Matter and Materials Physics*, vol. 93, no. 3, pp. 2–5, 2016.

[107] H. Duprez, E. Sivre, A. Anthore, A. Aassime, A. Cavanna, A. Ouerghi, U. Gennser, and F. Pierre, "Macroscopic electron quantum coherence in a solid-state circuit," *Phys. Rev. X*, vol. 9, p. 021030, May 2019.

[108] R. Bhattacharyya, M. Banerjee, M. Heiblum, D. Mahalu, and V. Umansky, "Melting of Interference in the Fractional Quantum Hall Effect: Appearance of Neutral Modes," *Physical Review Letters*, vol. 122, no. 24, p. 246801, 2019.

[109] M. P. Röösli, L. Brem, B. Kratochwil, G. Nicolí, B. A. Braem, S. Hennel, P. Märki, M. Berl, C. Reichl, W. Wegscheider, K. Ensslin, T. Ihn, and B. Rosenow, "Observation of quantum hall interferometer phase jumps due to a change in the number of bulk quasiparticles," *Phys. Rev. B*, vol. 101, p. 125302, Mar 2020.

[110] S. Kivelson, "Semiclassical theory of localized many-anyon states," *Physical Review Letters*, vol. 65, no. 27, pp. 3369–3372, 1990.

[111] P. Bonderson, A. Kitaev, and K. Shtengel, "Detecting non-abelian statistics in the ν=5/2 fractional quantum hall state," *Physical Review Letters*, vol. 96, no. 1, pp. 1–4, 2006.

[112] W. Bishara and C. Nayak, "Edge states and interferometers in the Pfaffian and anti-Pfaffian states of the $\nu = 5/2$ quantum Hall system," *Physical Review B - Condensed Matter and Materials Physics*, vol. 77, no. 16, pp. 1–8, 2008.

[113] W. Bishara, P. Bonderson, C. Nayak, K. Shtengel, and J. K. Slingerland, "Interferometric signature of non-Abelian anyons," *Physical Review B - Condensed Matter and Materials Physics*, vol. 80, no. 15, 2009.

[114] A. Stern, B. Rosenow, R. Ilan, and B. I. Halperin, "Interference, Coulomb blockade, and the identification of non-Abelian quantum Hall states," *Physical Review B - Condensed Matter and Materials Physics*, vol. 82, no. 8, pp. 1–9, 2010.

[115] R. L. Willett, K. Shtengel, C. Nayak, L. N. Pfeiffer, Y. J. Chung, and M. L. Peabody, "Interference measurements of non-Abelian e / 4 & Abelian e / 2 quasiparticle braiding Introduction to 5 / 2 interferometry :," *arxiv.org*, pp. 1–88, 2019.

[116] G. Jeon and J. Jain, "Nature of quasiparticle excitations in the fractional quantum Hall effect," *Physical Review B - Condensed Matter and Materials Physics*, vol. 68, no. 16, pp. 1–5, 2003.

[117] D. B. Chklovskii, "Comment on "New Class of Resonances at the Edge of the Two-Dimensional Electron Gas."," *arXiv*, vol. 1833, p. 9895, 1996.

[118] B. I. Halperin, "Quantized Hall conductance, current-carrying edge states, and the existence of extended states in a two-dimensional disordered potential," *Physical Review B*, vol. 25, no. 4, pp. 2185–2190, 1982.

[119] L. Saminadayar, D. C. Glattli, Y. Jin, and B. Etienne, "Observation of the $e/3$ fractionally charged laughlin quasiparticle," *Phys. Rev. Lett.*, vol. 79, pp. 2526–2529, Sep 1997.

[120] A. H. MacDonald and S. M. Girvin, "Quasiparticle states and the fractional quantum hall effect," *Phys. Rev. B*, vol. 33, pp. 4414–4417, Mar 1986.

[121] M. J. Kellogg, "Evidence for excitonic superfluidity in a bilayer two-dimensional electron system," Ph.D. dissertation, California Institute of Technology, 7 2004.

APPENDICES

A. INTERFEROMETER FABRICATION PROCESS

The majority of the fabrication process I have used is quite standard, and closely follows that described in John Watson's thesis. The main point where things diverge is the backgating process; this was a part of the process I had to develop on my own. The primary steps of surface processing are shown in Fig. A.1, while the steps of backgate processing are shown in Fig. A.2.

A.1 Gallium Stripping

1. Start with a full wafer, or cleave into a quarter or half wafer to work with. Blow off any dust bunnies from the surface before starting.
2. Spin a layer of AZ1518 resist at 4000 RPM for 40s.
3. Bake the resist for 2min at 100C.
4. Put a cleanwipe on hotplate and set to 50C. Put wafer face down (gallium side up) onto the cleanwipe.
5. Wipe off gallium with qtips. Keep wiping until all the shiny stuff is gone.
6. Spin and bake another layer of AZ1518 (4000 RPM 40s and bake 100C 2min).
7. Etch 2 min in full strength HCl. Quench etch by transferring to DI water.
8. Rinse well in DI water. Blow dry.
9. Squirt down with Acetone to strip resist from surface.
10. Sonicate 3min each in Toluene, Acetone, and IPA. Rinse with methanol and blow dry between each solvent. Spray down with DI water and blow dry.

A.2 Mesa Etch

1. Cleave wafer into a piece that fits the number of chips you want to fab.
2. Spin and Bake AZ1518 (4000 RPM 40s and bake 100C 2min).
3. Use MJB3 mask aligner. Align one corner of the pattern to the corner of the chip, and do your best to align the crystal axes with the axes of the mask (this is important for backgating).
4. Expose 20s with power 10mW/cm^2. If the power is different from this for some reason, adjust the time to get the same energy.
5. Prepare three beakers: two with MF-26A developer and one with DI water. Develop 20s in the 1st beaker and 10s in the beaker, then quench development in the DI water. Rinse with flowing DI water and blow dry. If you have multiple chips, throw out the developer and replace with fresh developer for each chip.
6. Load into Branson Asher on a glass slide. Once tool is pumped down, set flow rates to 130 for Argon and 13/6 for O2. Etch 90s with 100W power. Make sure there is no reflected power.
7. The etch solution is a 50:5:1 H2O:H3PO4:H2O2 mixture. Go to an acid hood and mix this together by starting with a 500mL beaker filled with 500mL of water, add 50mL of H3PO4 with a glass pippette, then add 10mL of H2O2 with the pipette. Mix together a bit then let sit for 20min to let it reach room temperature.
8. The etch rate for GaAs/AlGaAs structures will be $\sim$1.8nm/s. If you want to be really precise, etch a test piece first and measure it with a profilometer, then calculate the etch rate and scale for exactly how deep you want to etch. Etch your real sample for the desired length of time, then transfer to DI water, then rinse with DI water and blow dry.
9. Squirt with acetone to strip resist.

10. Sonicate in toluene, acetone, and IPA 3min each. Spray down with DI water and blow dry.

You should do the Ohmic contact deposition the same day as the mesa etch to avoid allowing the sidewalls to oxidize. At least, this is what I've always been told and what I've always done.

A.3 Ohmic Contacts

1. Spin and Bake AZ1518 (4000 RPM 40s and bake 100C 2min).
2. Align Ohmic contact pattern on mask to mesa pattern on chip.
3. Expose 20s with power 10mW/cm^2. If the power is different from this for some reason, adjust the time to get the same energy.
4. Soak 20min in chlorobenzene. This hardens the surface of the resist to create an undercut pattern in development, which aids the metal liftoff.
5. Use two baths of MF-26A developer. Develop 70s in 1st bath and 20s in 2nd. Quench etch in DI water; rinse with DI water and blow dry.
6. Load into Branson Asher on a glass slide. Once tool is pumped down, set flow rates to 130 for Argon and 13/6 for O2. Etch 15s with 100W power. Make sure there is no reflected power.
7. Get evaporator ready to quickly load sample. I've used the CHA and it usually works, but it's better to use our group's PVD if possible. For the CHA you should vent the chamber on have our sample holder ready; for the PVD vent the load lock and have the sample hold out and ready to mount, with the sample clips you want to use in place.
8. Take sample to acid hood. Etch 20s in HCl. Quench in DI water, rinse with DI water and blow dry.

9. As quickly as possible get the sample to the evaporator and under vacuum to avoid oxidtation after the HCl etch. You should aim to have the sample under vacuum within about 5 min.
10. Evaporate 8nm Ni/80nm Ge/160nm Au/36nm Ni. Use rates of 1.5 A/s for the initial Ni layer and 2 A/s for the rest. I've always used this metal stack for everything and it's always worked, although it may not be optimal for every structure.
11. Soak in acetone to liftoff. Blast with air brush filled with Acetone to blow off flakes.
12. Soak in some clean acetone. Rinse acetone off with IPA then DI water and blow dry.
13. Load into Jipelec RTA. Anneal in forming gas 2min at 435C (using John Watson's recipe).

At this point I like to cleave off one of the chips and bring to Physics to test the contacts. Sometimes contacts don't work for whatever reason (I tend to blame the CHA and haven't had this problem with the PVD, but who knows...), and you don't want to proceed with all the work just to be heartbroken when you find that contacts don't work. The chip you test will be sacrificial, though, so let it be one that's on the edge of the wafer and not really usable. You can't easily wirebond to the annealed metal, so I use indium soldering.

A.4 Electron Beam Lithography

1. Spin PMMA. I've had good success with 950 PMMA A2 (although if you use the Raith and use 25kV, there's some past experience that shows it lower mobility). Spin at 4000RPM for 40s and bake 8min at 180C on hotplate.
2. Load into EBL system and expose pattern. I've had good success using both the Raith at 3kV accelerating voltae and using the Elionix at 100kV; using the Raith

at 25kV hasn't worked so well and seems to cause damage. With the Raith at 3kV I've gotten good results with a dose of $36\mu C/cm^2$, and in the Elionix around $900\mu C/cm^2$. This will depend on the exact pattern, though, so it's reccomended to do a dose test with any new pattern.

3. Develop in 1:3 MIBK:IPA. For PMMA A2 I develop 30s, while for PMMA A4 I develop for 60s.
4. Load into evaporator. I've gotten good results evaporating 5nm Ti/10nm Au each at 1.5 A/s.
5. Soak in acetone to liftoff. Sonicate 30s in acetone to finish liftoff. Soak a few min in clean acetone then squirt down with IPA and DI water. Blow dry.

A.5 Bondpads

1. Spin and Bake AZ1518 (4000 RPM 40s and bake 100C 2min).
2. Align Bondpad pattern to Ohmic contact pattern in mask aligner.
3. Expose 20s with power $10mW/cm^2$. If the power is different from this for some reason, adjust the time to get the same energy.
4. Soak 20min in chlorobenzene. This hardens the surface of the resist to create an undercut pattern in development, which aids the metal liftoff.
5. Use two baths of MF-26A developer. Develop 70s in 1st bath and 20s in 2nd. Quench etch in DI water; rinse with DI water and blow dry.
6. Load sample into evaporator. I've succesfully used the CHA, Leybold, and PVD.
7. Evaporate 20nm Ti/150nm Au at 2 A/s for both layeres.
8. Soak in acetone to liftoff. Blast with air brush filled with Acetone to blow off flakes.
9. Soak in some clean acetone. Rinse acetone off with IPA then DI water and blow dry.

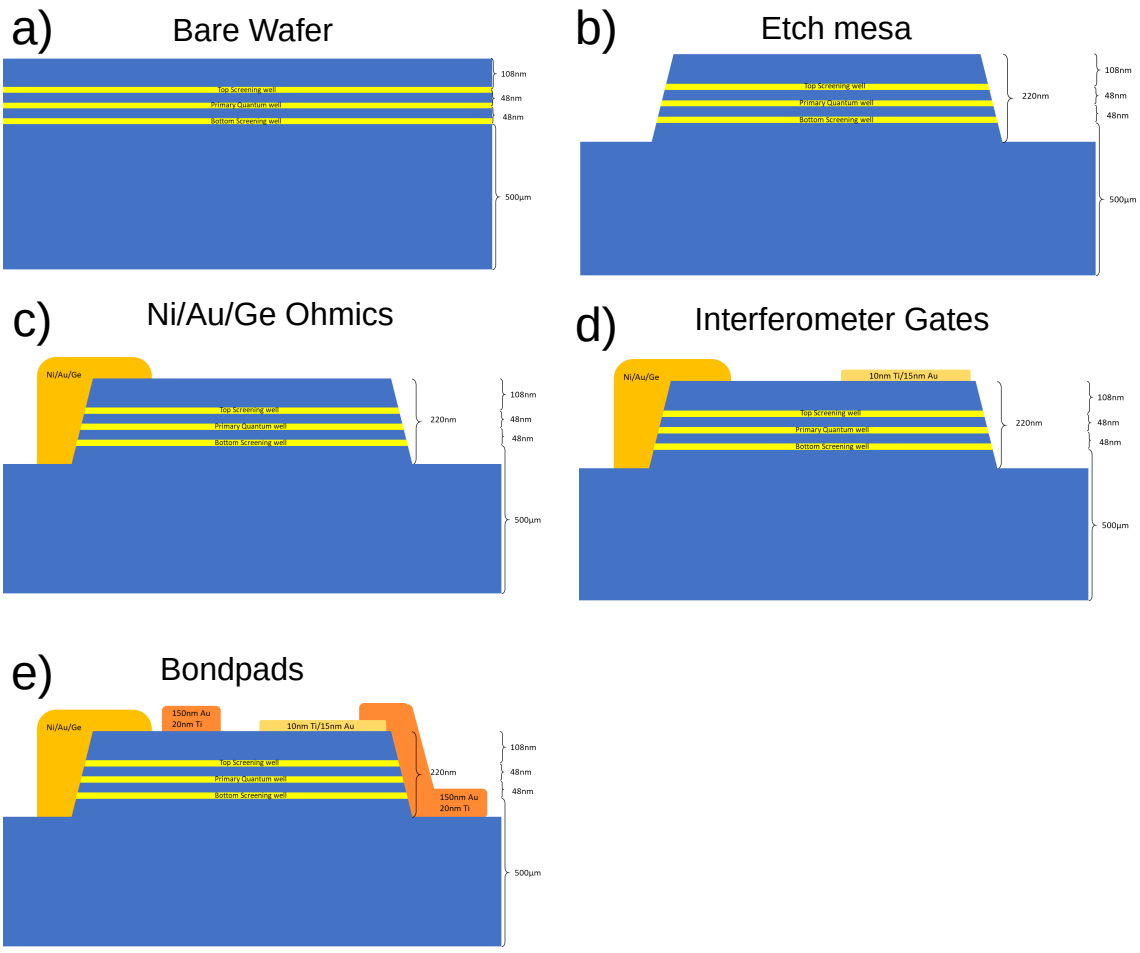

Fig. A.1. **Schematic of surface processing.** a) Bare screening well structure. b) Wet etch down through all GaAs wells and doping layers. c) Evaporated and annealed Ni/Au/Ge Ohmic contacts. d) Deposition of fine gates to define interferometer. e) Deposition of bondpads and surface gates around Ohmic contacts.

At this point if your sample is not going to back-gated and you have a single EBL layer, you are done. Otherwise continue on with backgating.

The back-gating process is something I had to develop. There are two difficulties to overcome. First, the GaAs substrates we use are 500μm thick, which is too thick to gate through without using thousands of volts, and that's too thick to have the

gate only affect part of the 2DEG (since we want to deplete the area around the Ohmic but not not under the interferometer). Second, it's tricky to align a pattern on the backside of the wafer to the features on the front side of the wafer. So, I needed to figure out a way to thin the substrate (without breaking the chip!) and align the backgates to the mesa defined on the surface. The Eisenstein developed a procedure for this in which they etched using bromine to thin the substrate, and used a mask aligner with an IR microscope (with GaAs being transparent to IR) to align the backside pattern [121]. Then, they soldered to the surface pads and used epoxy to glue wires to the backside, and mounted the samples via the gold wires to sample headers, with the chips being suspended in the air by the gold wires like little spiders. First of all, we don't have an IR mask aligner, so I had to find a different way to do alignment. Bromine in very dangerous and reactive, so I opted for mechanical polishing to thin the substrate rather than etching. Finally, I need to wirebond because interferometers have many bondpads, so just soldering isn't good enough, so I needed to find a way to avoid breaking the thinned chips with the wirebonder.

The general procedure I came up with is to finish surface processing, then cleave out my chips into individual chips. I then take a picture of the bottom left corner of the chip, which has the cleaved corner and a set of alignment marks; from this picture you can see how far the pattern is from the two edges. Then, mount the chip on a carrier chip (I used cleaved Si pieces for this) with Crystalbond, which protects the chip while you polish, and polish down the substrate to 50μm using SiC lapping films. This leaves a fairly rough surface, but this turned out not to be a problem. Then, take back to the cleanroom and, using the picture I took of the surface to judge where the surface pattern is relative to the bottom *right* corner (since it's now flipped), align the backgate pattern to the chip.

The backgates can just be wired up with gold wires and silver epoxy. In order to make the chips robust enough to wirebond to the surface, I embed them in epoxy (Stycast 2850). Originally, to avoid ever having to handle the thinned chips, I mounted the chips on PCB headers with the epoxy before removing the Si carrier

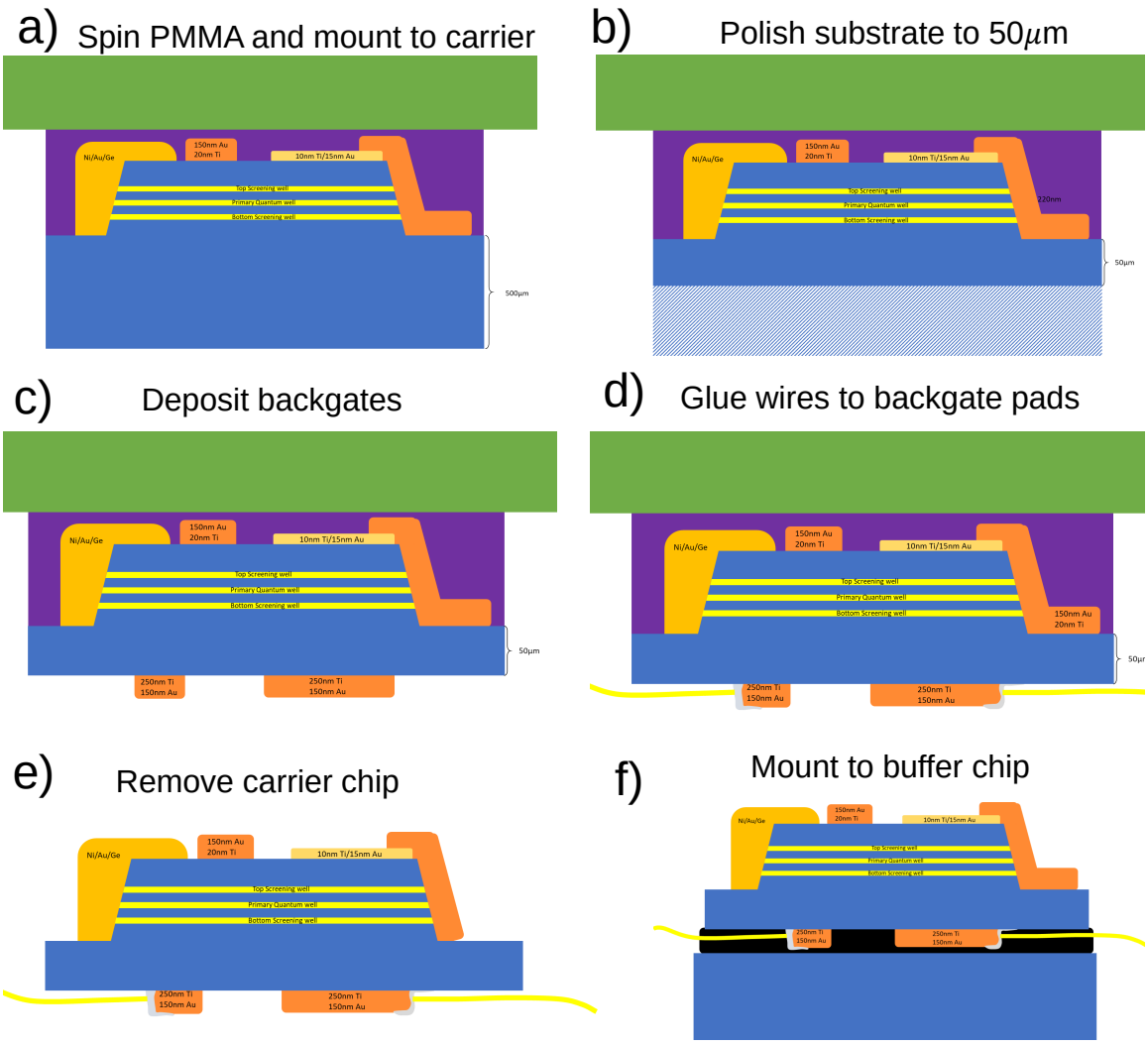

Fig. A.2. **Schematic of backgate processing.** a) Spin PMMA on surface to protect the surface, then glue to carrier Si chip. b) Mechanically polish to 50 μm. c) Deposit backgates. d) Glue gold wires to backgate pads with silver epoxy. e) Soak in acetone to remove chip from carrier chip. f) Mount to buffer GaAs chip with Stycast epoxy.

chip, then soaked in Acetone to remove the carrier chip. However, this caused 2 problems. First, I found that chips often broke after removing them from the fridges. Originally I thought this might be due to thermal cycling, but it was actually due to flexing of the PCB board due to handling the PCB and pulling it out of the sockets;

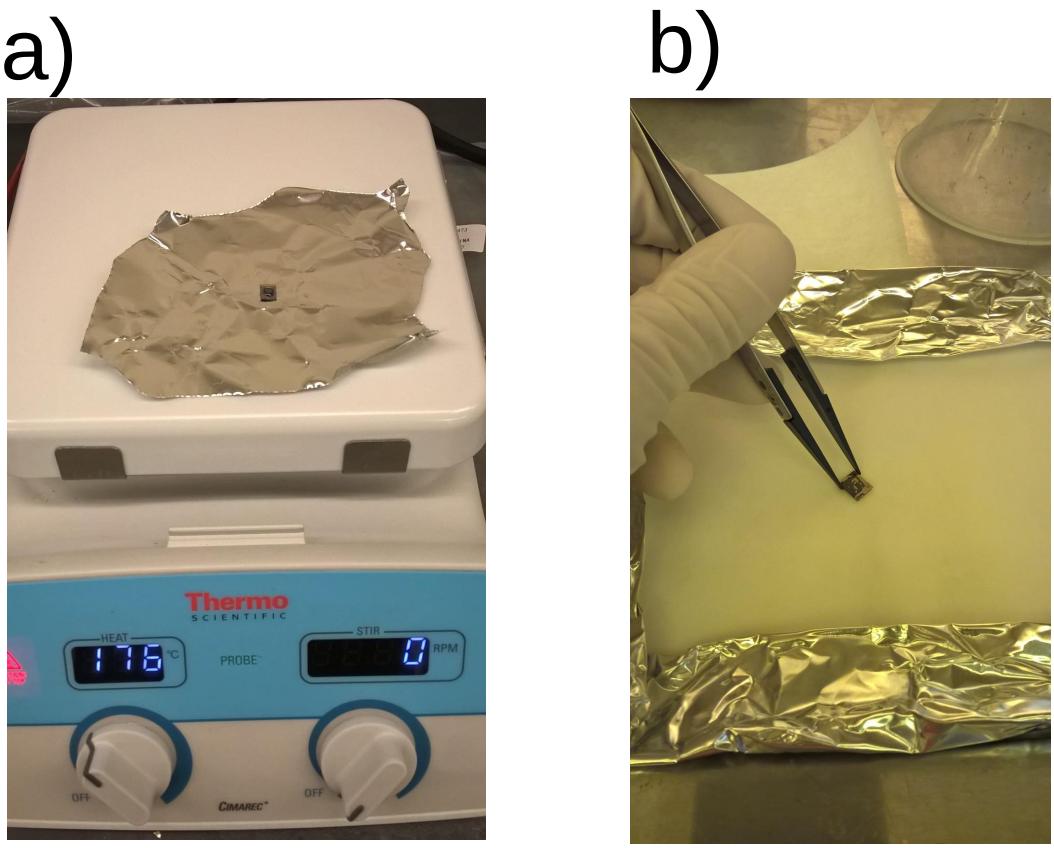

Fig. A.3. **Handling chips for backgate processing**. a)Gluing GaAs chip with surface processing finished to carrier chip before polishing. b) Handling chip after in cleanroom after polishing. You should be careful to grab with tweezers by the carrier chip and not let the chip land facedown to avoid breaking it. It's also a good idea to have nice soft carrying vehicle made of cleanwipes and foil to carry your samples around in.

this flexing transferred through the epoxy to the thinned chips, causing them to crack. To prevent this, I started mounting the chips with the epoxy to a GaAs 'buffer chip rather than directly to the PCB, and this greatly reduced chip breakage.

Second, the acetone to remove the carrier chip seems to soak into the epoxy and make it expand a little bit, and this caused the edges of the chip to break where the acetone was causing the epoxy to swell. To prevent this I started removing from the

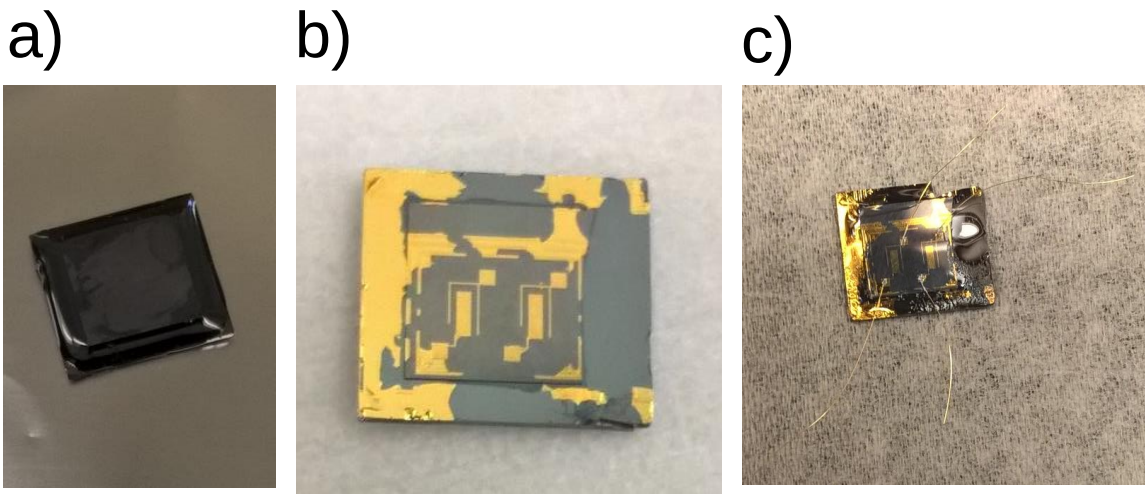

Fig. A.4. **Chips at various stages.** a) Chip after polishing but before depositing backgate. b) Chip after patterning and depositing backgates and lifting off. Getting all the metal off is a hassle. c) Chip after glueing gold wires to backgate pads.

carrier chips first by soaking in acetone (but still after gluing on the gold wires) so that the epoxy doesn't get soaked in acetone. Then I mount the chip to the buffer chip with epoxy. At this point you obviously have to be careful because you are handling a very thin chip. If you handle by the gold wires rather than grabbing the chip directly, however, I've found that the chips almost never break as long as you are careful.

With the chips thus secured with epoxy to a buffer chip, you can then mount the assembly on a header with rubber cement, and the epoxy makes it so you can wirebond to the chip without breaking it. On very rare occasions I've seen that the wirebonder will create cracks in the chip, but this is rare. Another thing that frequently happens is that the epoxy delaminates from the buffer chip after thermal cycling; however, this has turned out not to be a problem because the epoxy on its own provides a stable enough base to do further wireboning to the chip. It can be a little bit tricky though because the chip is now suspended by the gold wires, so it can

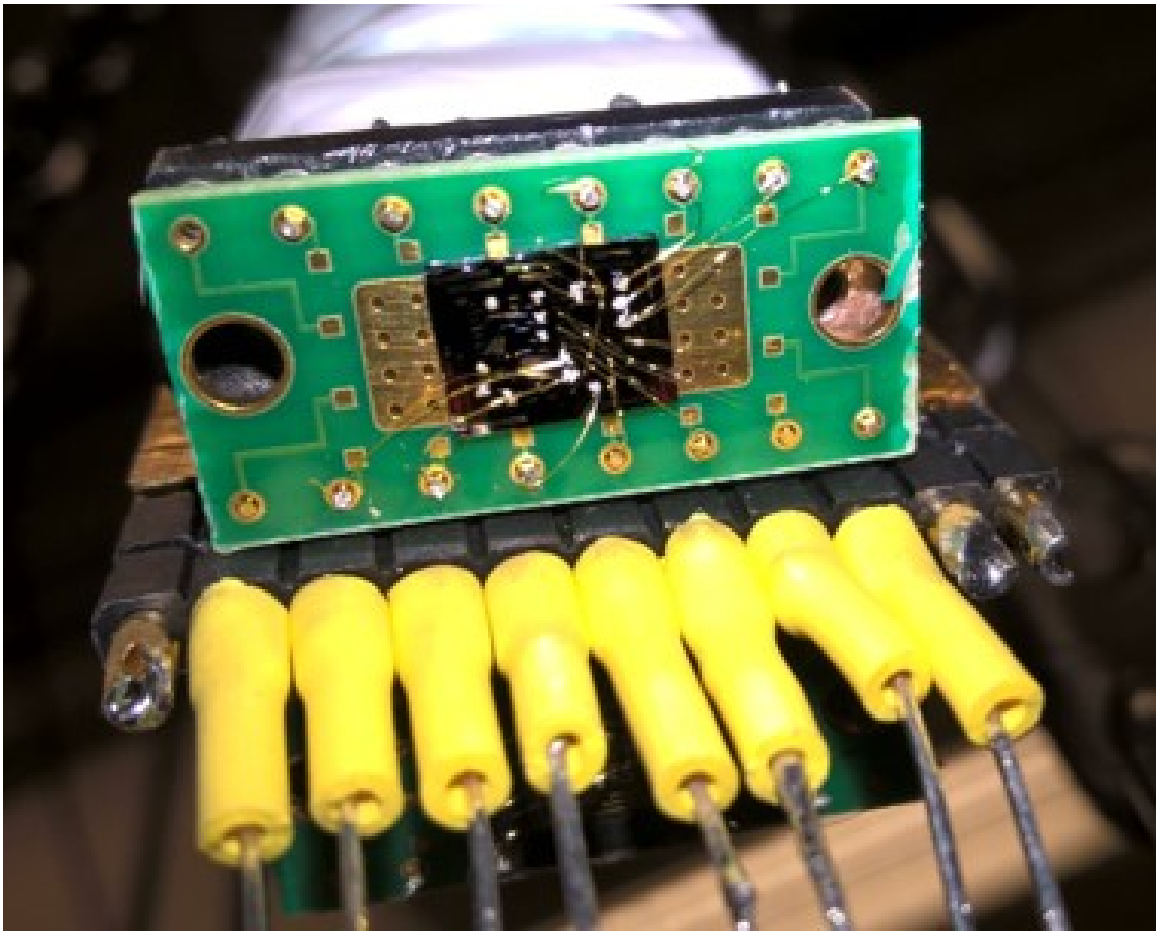

Fig. A.5. **Chip mounted in fridge.** Polished chip has been mounted to carrier chip and header and wirebonded. It is mounted in the Kelvinox on the end of the tail and ready to cool down.

get pushed down a little bit by the wirebonding tip, making it a bit more difficult to bond.

A.6 Backgate

1. Spin and Bake a layer of 950 PMMA A4 on the surface. This is to protect the surface during the backgate processing.
2. If you have multiple chips in a piece, it into individual chips.

3. Take pictures of the bottom left corner of each chip under the miscroscope; you will later use these pictures to align the backgate pattern to the surface.
4. Take chips from Birck to Physics.
5. Cleave out carrier chips from a blank GaAs or Si wafer. The carrier chip should be roughly 2mm wider then the real chip. Put a scratch in one corner of the carrier chip to mark where the bottom left corner of the real chip will go.
6. Heat the carrier chip up on a hotplate to 180C.
7. Add some Crystalbond 509 to the carrier chip.
8. Use tweezers to place the real chip face down on the carrier chip, aligning the bottom left corner with the scratch you made. Press firmly down to get it flat.
9. Use calipers to make sure the chip is flat. Do this by measuring the thickness along all the edges of the sample to ensure that no part is sticking up more than another. If it is not flat, re-heat it and try to get it flat.
10. Polish by hand using 30um and 12um SiC lapping films (Ted pella part numbers 815-372 and 815-374). Get the film wet with water, then use your finger to rub it on the film in circular motions. Your target thickness is around 50μm. Use calipers to measure how much you've taken off and to make sure you're keeping it flat. Once you've removed 350 μm, switch to the 12 μm film.
11. Once you're finished polishing, rinse with water and wipe down with qtips to get the debris off. The polished chips are fragile so be careful, although as long as they're glued down they're not likely to break.
12. Bring chips back to cleanroom.
13. Squirt down with acetone then soak in acetone for about 1 minute to remove excess Crystalbond from the surface. You don't want to soak for too long though because acetone dissolves Crystalbond 509 you don't want to risk the chip coming off the carrier chip at this point.
14. Soak for a few minutes in IPA and DI water.

15. Spin and Bake a layer of AZ1518 photoresist.
16. Align the marked corner of the chip with the backgate pattern. Refer to the pictures you took under the microscope to identify where the surface pattern is relative to this corner. Remember that things are mirrored since you flipped the chip over, so you're aligning the bottom right corner of the backgate to the bottom right corner of the flipped chip (which corresponds to the bottom left corner of the surface pattern).
17. Expose 20s at 10mW/cm^2.
18. I've found that for some reason using chlorobenzene messes up the development at this point, so don't use it. Just develop in MF-26A (30s in 1st bath and 20s in 2nd bath), quench in DI water, rinse in DI water, and blow dry.
19. Check pattern under microscope and make sure it's consisten with the picture you took of the surface relative to the corner.
20. Load into evaporator. Evaporate 100nm Ti/150nm Au.
21. Soak in acetone to lift off. Because you didn't use chlorobenzene this liftoff is hard. Try not to soak for too long in acetone because you don't want the chip to come off the carrier yet. Use steel tweezers to make little perforations in the resist and metal so that the acetone can dissolve the resist. Obviously be very careful that you don't damage the chip when you do this. Use the air brush to blast off the metal, but fill it with DI water instead of acetone so you don't accidentally blast the chip off the carrier and break it into a billion pieces. You may need to go through several cycles of making little perforations with tweezers, soaking for a short time in acetone, then blasting with DI water.

A.7 Mounting to header

1. Take chips back over to Physics.

2. Use silver epoxy (EPO-TEK EJ2189-LV) to attach gold wires (2mil thickness) to the backgate pads. Do this while the chip is still attached to the carrier.
3. Bake for around 10min at 120C to cure the epoxy. Make sure the wires are firmly attached.
4. Soak the chip in acetone in a petri dish to left the chip off the carrier. Put cleanwipe at the bottom of the dish so there's something soft there rather than hard glass.
5. It may take several hours for the chip to lift off of the carrier, but it should do so eventually. Once it does you need to be extremely careful; handle only by the gold wires, and don't grab the chip itself at this point. Transfer from the acetone to a petri dish full of IPA, then take it out and gently blow dry with a hair dry from a good distance.
6. Cleave a blank GaAs chip slightly larger than your chip. Mix Stycast 2850 and apply a little bit to the blank chip and a little bit to the backside of the real chip, and glue down your chip to the blank chip, making sure gold wires are sticking out. Use the gold wires to manipulatet the chip and get it relatively flat, but it should embedded in the epoxy rather than than flux against the blank chip.
7. Let epoxy cure overnight.
8. Glue the carrier chip down to a PCB header with rubber cement.
9. Indium bond the gold wires to the header and wirebond the contacts on the chip.

At this point the device is finished and you are ready to measure!

B. SIMULATION CODE

This is the Matlab code I used to generate the simulation data in Fig. 3.12; the temperature was selected to give a ratio of the T to $\frac{e^2}{2C}$ of 0.002. The output of this is shown in Fig. B.1.

```
%Input Parameters
A0=0.1;  %Area in um^2
v=1/3; %filling factor of state
thetaAnyon=1/3; %phase when braiding one quasiparticle around
    another. 1/3 for 1/3 state
estar=1/3; %quasiparticle charge
maxQP=30;  %number of QPs to include in range
SWsetback = 48; %setback of SWs from main QW in nm
n_electron = 0.7; %electron density in units of 10^11 /cm^2
T = 0.1; %temeprature in units of K
Delta=5.5/2; %Energy gap in units of K. The transport gap is
    divided by 2 because it creates a QP-QH pair, whereas here
    we use Delta to create one QP or one QH
Vsgleverarm=.12; %lever arm for change in area, dA/dVg (in um
    ^2/V)
Vsgbulkleverarm=0.02*1000; %lever arm for change in bulk
    charge with gate, dq_bulk/dVg (in electrons/V);

%Constants
epsilon = 12*8.854e-12; %permittivity of semiconductor
phi0=4.14; %magnetic flux quantum in um^2mT
```

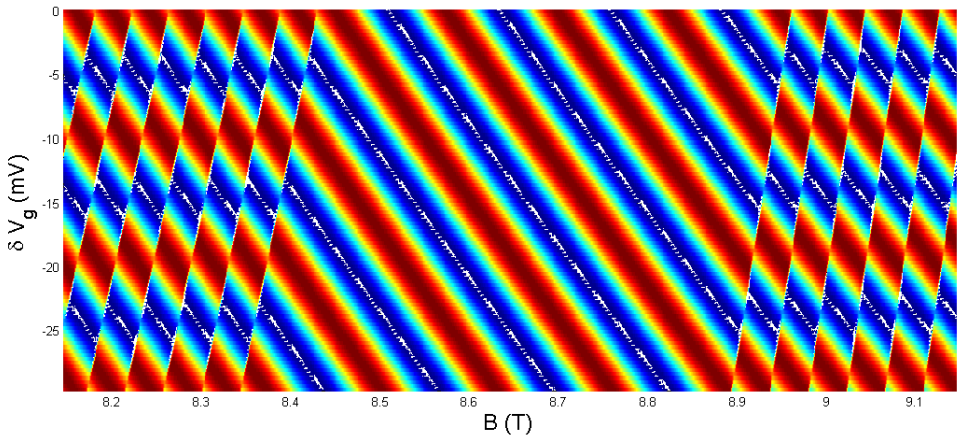

Fig. B.1. **Output plot from Matlab for simulation of conductance versus gate voltage δV_g and magentic field B.** The central region exhibits Aharonov-Bohm interference where no quasiparticles are created, while at high field quasiholes are added and low field quasiparticles are added resulting in discrete phase jumps, consistent with the results of [88]. The temperature is set to give a ratio of T to $\frac{e^2}{2C}$ of 0.002, resulting in very sharp jumps in phase due to minimal thermal smearing.

```
17
18 %Calculated parameters
19 C = A0*1e-12*2*epsilon/SWsetback/1e-9 %calculation of
       characteristic geometric capacitance
20 ec = 1.602e-19/2/C*1e6 %Charging energy in units of eV,
       calculated as e^2/2C
21 k1=ec*1e-6/8.62e-5 %Charging energy converted into units of
       temperature (K)
22 B0=n_electron*4.14/v; %Center magnetic field of exact state
       filling
23
24
```

```
25
26 %Simulation parameters
27 dB=0.001; %Magnetic field resoultion
28 dVg = .0003; %Gate voltage resolution
29 numx=1000; %Number of points in x-axis (magnetic field)
30 numy=100; %number of points in y-axis (Vg)
31 numxBoffset = 550; %Point to center the magnetic field
32
33 %Arrays containing simulated data
34 R=[]; %Array containing the conductance oscillations
35 expQP=[]; %Array containing the calculated thermal
       expectation values
36 A=[]; %Array containing area at each B and Vg
37 B=[]; %Array contaning magnetic field
38 Vsg = []; %Array containing side gate voltage at each point
39
40
41 %These loops iterate through each value of magnetic field and
        gate voltage
42 %in the simulation. n is the index for the magnetic field
       point, m is the
43 %index for gate voltage point. At each point the conductance
       oscillation is
44 %calculated.
45 for n=1:numx
46
47    for m=1:numy
48          Vsg(n,m)=(m-numy)*dVg; %Gate voltage at each point
```

```
49      B(n,m)=B0+dB*(n-numxBoffset); %Magnetic field at each
            point
50      deltaB=B(n, m)-B0; %Magnetic field relative to exact
            filling
51      A(n, m)=A0+Vsg(n,m)*Vsgleverarm; %Calculate area based
            on gate voltage and lever arm
52      phi=A(n,m)*B(n,m)*1000/phi0; %Number of flux quanta
53      dphi=A(n,m)*(B(n,m)-B0)*1000/phi0;
54
55
56      Z = 0; %Partition function
57      a=0;
58      expQP(n,m)=0; %Expectation value of quasiparticle
            number, to be calculated
59      Energy0=0; %minimum value of the energy in the
            summation. This needs to be here because if the
            energy gets too negative then Matlab calculates the
            exponential of it as just zero, which messes up the
            simulation.
60
61      Energies = []; %Array containing energy at each value
            of the quasiparticle number
62
63      %This loop calculates the energy at each allowed value
            for the number
64      %of quasiparticles. q is the quasiparticle number (
            negative q means
65      %quasiholes).
66      for q = -maxQP:maxQP
```

```
67          deltaQtotal=v*deltaB*1000/phi0*A(n,m)-Vsg(n,m)*
                Vsgbulkleverarm+q*estar; %amount of charge away
                from ideal value, in units of e
68
69          if q==-maxQP
70              Energy0 = k1*deltaQtotal^2+abs(q)*Delta*(1+0*
                    abs(q));
71          end
72
73          Energy = k1*deltaQtotal^2+abs(q)*Delta; %Energy
                calculated as combination of chargning energy
                and energy cost for creating the number of
                quasiparticles
74          if Energy<Energy0
75              Energy0 = Energy; %this sees if the current
                    energy value is the smallest one yet, and if
                    so sets Energy0 equal to that
76          end
77          Energies(q+maxQP+1)=Energy;
78      end
79
80      %This loop calculates the expectation value of the
            conductance
81      %oscillation. The variable a is the sum of all the
            values of
82      %cos(theta)*e^(-E/kT). Z is partition function.
83      for q = -maxQP:maxQP
84          Z = Z+exp(-(Energies(q+maxQP+1)-Energy0)/T); %add
                each term in the summation to get Z
```

```
85              expQP(n,m) = expQP(n,m)+q*exp(-(Energies(q+maxQP+1)
                    -Energy0)/T); %add up contribution to the
                    expectation value of qp number
86              t=2*pi*(q*thetaAnyon+A(n,m)*B(n,m)*1000/phi0*estar)
                    ; %phase at point in the summation
87              a = a+exp(-(Energies(q+maxQP+1)-Energy0)/T)*cos(t);
                     %conductance at each point in the summation
                    times the thermal factor
88          end
89
90          expQP(n,m) = expQP(n , m)/Z; %calculate the normalized
                thermal expectation
91          R(n, m)=a/Z; %calculate the normalized conductance
92      end
93  end
94
95  %Plotting
96  surf(B', 1000*Vsg', R', 'edgecolor', 'none') %Creates
        colormap plot of conductance
97  axis([B(1,1), B(numx, 1), 1000*Vsg(1,1), 1000*Vsg(1,numy)])
98  xlabel('B (T)', 'fontsize', 18);
99  ylabel('\delta V_{g} (mV)', 'fontsize', 18);
100
101 %Put data in a nice array to export to origin
102 exportdata=zeros(1+numy, 1+numx);
103 B=B';
104 Vsg=Vsg';
105 R=R;
106 exportdata(1,1)=0;
```

```
107 exportdata(1, 2:(numx+1))=B(1, :);
108 exportdata(2:(numy+1), 1)=Vsg(:, 1);
109 exportdataCrossSection = [B(1, :)', R(:, 1)];
110 for n = 1:numy
111     exportdata(n+1, 2:(numx+1))=R(:, n);
112 end
```

C. LIST OF SAMPLES MEASURED

Table C.1.
List of samples measured

Sample	**Structure**	Density ($\times 10^{11}$ cm^{-2}	**Device**	**Results**
Willett device	Doping Well	3.5	1.2μm×1.2μm with no screening gate	CD interference at integers states and $\nu = 5/3$
12-18-15.1 J1a	SHJ	0.66	2μm×2μm; no screening gate	Mostly CD. Weak AB and intermediate regime at low field.
8-10-16.2 J1c	Shifted SHJ	1.6	3μm×3μm with etched trench gates and screening gate	Very disordered QPCs. Weak AB at 3T but not much else
3-30-16.2 J1d	Shifted SHJ	1.6	3μm×3μm with screening gate, dielectric, and helper gate	Very disordered, probably caused by 20kV EBL used in overlay layer
3-30-16.2 J2c	Shifted SHJ	1.6	3μm×3μm with screening gate, dielectric, and helper gate. 3kV EBL.	Good clean QPC behavior. Weak AB interference at low field. Trying to tune helper gate didn't improve coherence at all.
11-28-17.1 J1a	Double SW (low density SWs)	1.7	3μm×3μm and 1.6μm×1.6μm with screening gate	Some AB at low field in 3.0μm device. CD only in 1.6μm device. Screening wells don't conduct at low temperature because they are too low density.
11-21-17.1 J1a	Double SW	0.9	1.2μm×1.2μm	With some positive bias on top screening gate, get strong AB oscillations. Now way to isolate transport in main QW, though, so the oscillations could be in any of the wells. Proof of concept for SW design.
2-1-18.2 J2a	Single SW	0.92	1.2μm×1.2μm with top screening gate and top Ohmic gate to isolate transport in QW	AB oscillations up to $\nu = 1$, then transition to CD
2-1-18.1 J3a	Double SW	1.05	1.2μm×1.2μm with top screening gate and top and bottom Ohmic gate to isolate transport in QW. Measured right side device on chip.	Results presented in Chapter 2. Strong AB at integer states and $\nu = 1/3$ and $\nu = 2/3$.
2-1-18.1 J4c	Double SW	1.3	1.2μm×1.2μm with top screening gate and top and bottom Ohmic gate to isolate transport in QW	Density too high to get to $\nu = 1/3$ ($n = 1.3 \times 10^{11}$cm^{-2}).
5-14-18.1 J1a	Double SW	0.42	1.2μm×1.2μm with top screening gate and top and bottom Ohmic gate to isolate transport in QW	Contacts stop working at high field, probably because density too low.
7-18-18.1 J1a and b	Double SW	0.72	1.2μm×1.2μm interferometer with dielectric and antidot gate	Very noisy device, too noisy to get any sensible results at $\nu = 1/3$.
6-27-18.1 J1c	Double SW	0.63	Interferometer with etched antidot	Device seems pathological with very asymmetric QPCs, probably due to etched antidot
6-28-18.1 J1c	Double SW	0.6	Standard interferometer 1.2μm×1.2μm without antidot	Good AB interference at integers and $\nu = 1/3$
9-18-18.1 J2b	Double SW	0.7	1.2μm×1.2μm Interferometer with gated antidot and Al2O3 dielectric	Noisy device. Can still get some interference at $\nu = 1$ and $\nu = 1/3$. Antidot gate results in noisy, but seemingly continuous phase evolution.

Table C.2.
List of samples measured Cont.

Sample	**Structure**	Density ($\times 10^{11}$ cm^{-2}	**Device**	**Results**
3-30-16.1 J2a	SHJ	1.2	500nm and 800nm quantum dots	Measure Coulomb blockade. Get 50mK electron temperature without RC filters. With 10kOhm/100nF RC filters get 20mK.
9-18-18.1 J3a	Double SW	0.7	0.8μm$\times 0.8\mu$m interferometer with no antidots	Device shows no interference; seems pathological. Very asymmetric QPCs.
9-18-18.1 J3b	Double SW	0.7	1.0μm$\times 1.0\mu$m interferometer with no antidots	Measured interference at integer states and $\nu = 1/3$. Get $T_0 = 130$mK at $\nu = 1$ and $T_0 = 63$mK at $\nu = 1/3$.
9-18-18.1 J3c	Double SW	0.7	0.8μm$\times 0.8\mu$m and 0.7μm$\times 0.7\mu$m interferometers with no antidots	Intermediate regime behavior in 700nm and 800nm devices at $\nu = 1$. 800nm device showed stronger AB behavior at $\nu = 2$ and $\nu = 3$ of outer mode. Also some AB behavior at $\nu = 1/3$.
9-18-18.1 J3e	Double SW	0.7	1.0μm$\times 1.0\mu$m and 0.8μm$\times 0.8\mu$m interferometers with Al2O3 and antidot gates	Devices were extremely noisy and give complete junk data.
9-18-18.1 J4b	Double SW	0.7	Standard interferometer 1.2μm$\times 1.2\mu$m. Measured top right device on chip.	Second device in Chapter 3. Good AB interference at $\nu = 1$ and $\nu = 1/3$. Single discrete phase jump visible.
9-18-18.1 J4c	Double SW	0.7	Standard interferometer 1.0μm$\times 1.0\mu$m. Measured top left device on chip.	Primary device in Chapter 3. Good AB interference at $\nu = 1$ and $\nu = 1/3$, shows transition from negative slope to flat lines of constant phase with discrete phase jumps in cetner.
9-18-18.1 J4d	Double SW	0.65	Standard interferometer 1.0μm$\times 1.0\mu$m. Measured top left device on chip.	Shows transition from AB interference at center to flat lines of constant phase at high and field consistent with samples J4c and J4b and the results in Chapter 3. Discrete phase jumps consistent with those described in Chapter 3 are also visible, although the data is significantly noisier such that the jumps cannot be resolved as well.